Pt Nanoparticle Facets Characterised by CO Adsorption with Infrared Spectroscopy

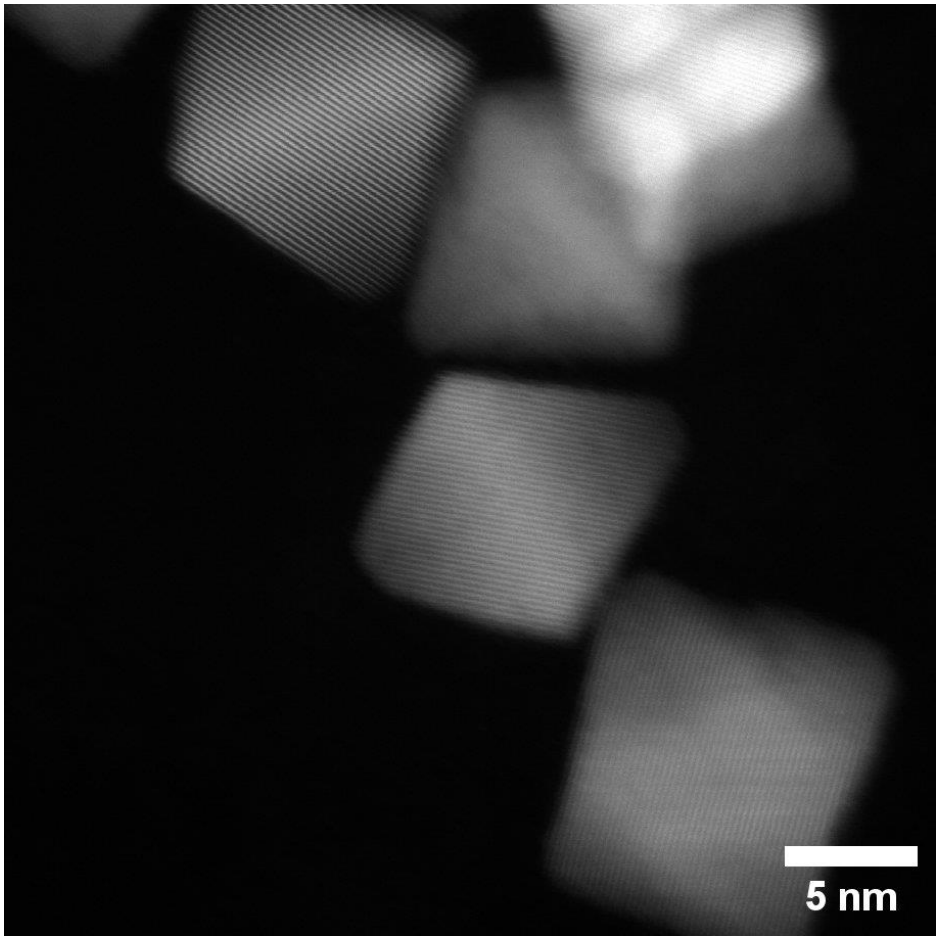

Master Thesis in Chemistry submitted by

Selena Schraven

Under supervision of

Dr. Bettina Baumgartner
Dr. Matteo Monai
Prof. dr. Eelco Vogt

05-02-2024

Inorganic Chemistry and Catalysis
Debye Institute for Nanomaterials Science
Utrecht University

Layman's abstract

Catalysts are used to accelerate the rate of a reaction. Currently, catalysts made of metal nanoparticles are heavily researched and used in industrial processes as they proved to be effective catalysts for numerous reactions. Nanoparticles have dimensions of 1–100 nm and, therefore, have a very high surface area-to-volume ratio. This ratio is important because the higher this ratio, the more active sites where molecules can adsorb and react are present on the metal nanoparticles.

Besides the size of these metal nanoparticles, the shape can be changed into cubes, octahedrons, tetrahedrons, or rods. Every shape has different surface facets on which atoms are arranged differently, and reactivity can be different. Currently, Transmission Electron Microscopy (TEM) is used to determine the shape and size of synthesized metal nanoparticles. However, this is an expensive and time-consuming technique. This research studies if carbon monoxide infrared (CO-IR) spectroscopy can be used to determine the shapes and sizes of platinum nanoparticles.

In CO-IR spectroscopy, infrared (IR) light interacts with the platinum nanoparticles. Depending on the atoms and chemical bonds involved, IR light at a specific wavelength will be absorbed, allowing to get “fingerprint” information of molecules. Platinum is chosen as the metal in this study because when carbon monoxide (CO) adsorbs on platinum, a distinct band can be seen in the CO-IR spectrum at a frequency between 2000 and 2100 cm^{-1}. The exact observed frequency in this range will depend on the environment of the platinum, such as the shape, size, and facet of the platinum nanoparticle.

Cubes and octahedrons were synthesized in this study, after which TEM images were taken of them to determine their size and shape. Then, CO-IR spectroscopy measurements were done on the same samples, and a correlation between the Pt-CO band position and TEM images was derived. Seven different bands were assigned contributing to the broad Pt-CO band.

It was found that the final shape of the Pt nanoparticles depended on various factors during the synthesis, including the reaction temperature, stirring rate, and the method of adding the metal. The Pt-CO band shifted to higher wavenumbers when increasing reaction temperatures were used. This shift is attributed to an increase in the number of atoms a Pt atom is directly neighbours with. Furthermore, it was seen that when looking at cubes synthesized at different reaction temperatures, 160 and 200 °C, at a high resolution, they had no noticeable shape differences; however, there were differences in “fuzziness” on the edges. This still has to be further investigated. As for the octahedrons, it was shown that silver atoms added during the synthesis are not entirely removed after the synthesis. They form bridges between the platinum nanoparticles. Furthermore, it was seen that the octahedrons were forming circular assemblies.

CO adsorption on different samples showed that the Pt-CO band shifted with different samples and when reactive gasses flowed over the sample (H_2 and O_2). Additionally, using Pt as a catalyst in converting CO to CO_2 in an O_2 environment showed that Pt cubes with a lower coordination number converted CO at a lower temperature than those with a higher coordination number. However, more research should be done on the synthesis method to get more platinum nanoparticles with the same shape.

Abstract

Platinum nanoparticles (Pt NPs) are used extensively as catalysts in numerous catalytic reactions. The shape and size of these nanoparticles can affect the activity and selectivity of these reactions. It is, therefore, important to find a way to characterize these properties of the catalyst. Nowadays, Transmission Electron Microscopy (TEM) is often used to characterize the size and shape of nanoparticles. However, this only analyses a small sample size and is an expensive method. It is known that the Pt environment affects the Pt-CO band position in carbon monoxide infrared (CO-IR) spectroscopy. In this study, I researched if CO-IR spectroscopy can be used to characterize the shape and size of Pt NPs.

Depending on the nanoparticle's shape, different facets are exposed. Platinum cubes and octahedrons both have only one surface facet, {100} and {111}, respectively. During this research, both Pt cubes and octahedrons were synthesized using the polyol method. The resulting nanoparticles were then characterized with TEM to obtain the average particle size and shape. Thereafter, CO-IR spectroscopy was done with the cubes and octahedrons. The Pt-CO band position was then studied to see if it corresponds to the TEM results.

Reaction temperature, stirring rate, and precursor and ligand addition methods seemed to be crucial factors in the resulting nanoparticle shape. Higher temperatures resulted in a blueshift in the Pt-CO band. However, peak fitting of the CO adsorption DRIFTS spectra gave inconclusive results, and no difference between cubes and octahedrons could be made. HR-TEM images of the cubes synthesized at 160 °C and 200 °C showed minimal differences but a possible difference in the straightness of the edges. The former showed more ridges formed on the surfaces, thus more under-coordinated Pt atoms on the surface. However, a small sample size was studied, and further research should be conducted. Octahedrons displayed low CO adsorption, attributed to residual silver bridges between the Pt nanoparticles blocking the CO adsorption sites and circular aggregate formation of the Pt nanoparticles reducing the total surface area. H_2 pretreatments resulted in the band splitting into two distinct bands, attributed to the well-coordinated and under-coordinated sites. O_2 pretreatments led to a blueshift of the Pt-CO band to 2100 cm^{-1}.

In the future, more research should be done on the synthesis to get more uniform results. This will lead to a clearer picture of the CO-IR spectroscopy results. Therefore, the surface facets of more samples should be characterized with HR-TEM to determine the facets.

Contents

1. Introduction

Metal nanoparticles are widely researched due to their extensive use as catalysts. Nanoparticles, with a size range of 1–100 nm, have a higher surface-to-volume ratio than bulk metal, providing more active sites and increasing the reaction rate and product yield.[1] Additionally, by changing the metal or combining different metals, the properties of the catalyst can be changed.[2] This versatility allows for a wide range of applications. One of the most researched metals is platinum (Pt) because of its exciting properties, such as a high melting point and excellent stability. These properties make platinum a great candidate in many catalytic processes, such as fuel cells,[3–5] photocatalysis,[6,7] and water electrolysis.[8,9] Next to catalysis, platinum is also utilised in applications in the medical field, for example, as an anti-bacterial agent[10–12] and for cancer treatment.[13,14] Given their many applications, researchers are studying the synthesis of these platinum nanoparticles and the optimisation for catalytic reactions.

The size and shape of platinum nanoparticles influence the physical properties of the nanoparticles, such as their activity and selectivity.[15–18] Therefore, these properties are important for the eventual application of the catalyst, and the synthesis method should be chosen accordingly. Firstly, the smaller the nanoparticles are, the greater their surface-to-volume ratio is. Unlike bulk material, nanoparticles need less material to achieve the same number of active sites. The more active sites there are, the higher the catalyst activity is. Secondly, the shape of the nanoparticles determines the type of facets they possess. Platinum has a face-centred cubic (fcc) crystal structure, which is the closest possible packing of the atoms.

Well-coordinated closed-packed metal surface facets generally have the lowest free energies, and thus, most metal nanoparticles primarily expose (111) and (100) surface facets. For an fcc single crystal, the surface tensions (γ) associated with the low-index crystallographic planes are in the order of $\gamma_{111} < \gamma_{100} < \gamma_{110}$. The most stable shape an fcc crystal can adopt is the truncated octahedrons. Cubes have only {100} facets; most other shapes have {111} facets or a combination of {100} and {111} facets. Examples of the former are octahedrons, tetrahedrons, and tripods. Cuboctahedrons belong to the latter. Different nanoparticle shapes with their facets can be seen in Figure 1.

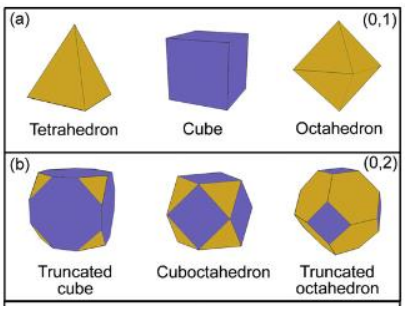

Figure 1 Compilation of various nanoparticle shapes with yellow depicting {111} facets and blue depicting {100} facets. Adapted from Peng et al. (2009).[81]

The polyol method is one way to synthesise platinum nanoparticles with a specific size and shape.[19–22] This process uses a polyol, like polyethylene, as both a solvent and reducing agent. The polyol method allows for higher reaction temperatures, and due to its high viscosity, the reaction is diffusion-controlled.[21,23] Other advantages are that it protects from metal oxidation and minimises coalescence. In addition to the polyol, a platinum precursor such as platinic acid (H_2PtCl_6) is needed. The polyol reduces the platinum to its zero-valent state, followed by

agglomeration to platinum nanoparticles. Ligands are used to control the growth of the nanoparticles and stabilise them. Structure-directing agents are a method to control the shape of the eventual nanoparticles.

Characterisation of the shape and size of these nanoparticles is usually done with Transmission Electron Microscopy (TEM), which has both advantages and disadvantages. The advantages are that it provides information about the nanoparticles' distribution on the support and the nanoparticles' uptake, and it delivers a high-resolution image of the shape and size of the nanoparticles. The major disadvantage of TEM is that only a small sample size is analysed. If another characterisation technique could be used to characterise and quantify the facets of Pt nanoparticles, it could increase its accessibility. When these two datasets are combined (facet characterization and quantification), information on the nanoscale and at the ensemble level of the Pt nanoparticles is disclosed.

Carbon monoxide infrared (CO-IR) spectroscopy is a less expensive technique, making it more accessible and allowing for the analysis of a larger sample area. The Pt(0)-CO bond shows a very characteristic band around 2000–2100 cm^{-1} in CO-IR spectroscopy. The band position and intensity depend on the platinum environment.[7,24–27] This research aims to discover whether the facets of the Pt nanoparticles and their size can be determined by the position and intensity of this band in a CO-IR spectrum. To achieve this goal, cubic and octahedral platinum nanoparticles will be synthesised using the method of Song et al. (2005).[23] The details and mechanism of this synthesis method will be explained in Section 2, and the synthesis steps are given in Section 3. Both TEM and DRIFTS will then be used to characterise the nanoparticles. First, an overview of all the syntheses regarding size and shape is given in Section 4, after which in Section 5, the CO-IR spectroscopy results of the samples will be compared to evaluate if a difference in shape affects the Pt-CO band position in CO-IR spectroscopy.

2. Theory

2.1. CO adsorption on platinum

Infrared spectroscopy, in combination with carbon monoxide (CO) adsorption, is a powerful tool for studying Pt nanoparticles. The Pt(0)-CO bond exhibits a distinct band in the IR spectrum, typically observed around 2000–2100 cm^{-1}. This spectral region offers minimal interference from other absorptions, ensuring easy identification of the Pt(0)-CO band without overlap with other bands. However, the precise band position does depend on several factors, including the Pt atom's environment, oxidation state, CO adsorption configuration on Pt, and CO coverage of the Pt.[28]

CO adsorbs on the surface of a Pt NP through two electronic interactions, forming a σ bond and a π bond. The σ bond is formed between the carbon's lone pair and an empty d orbital of the metal. Concurrently, the partially filled d orbitals of the metal donate electrons back to the π antibonding orbital (π^*) of the CO bond, known as π backdonation (Figure 2).[29] A correlation exists between the CO bond strength and the metal-CO bond strength. The strength of the CO bond is influenced by the extent of back-donation and the overlap of the relevant orbitals.[30] Essentially, the stronger the metal-CO bond, the more back-donation, and the more electrons are donated to an antibonding orbital from CO, making the bond weaker. Multiple factors contribute to the Pt-CO bond strength, including Pt oxidation state, CO adsorption configuration on Pt, CO coverage, and the specific adsorption site.

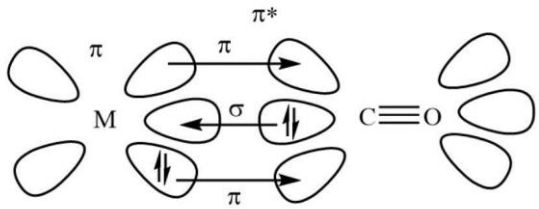

Figure 2 Synergic bonding in metal carbonyls.

The oxidation state of Pt influences CO bond strength due to the variations in d orbitals filling. Weaker π backdonation due to less-filled d orbitals produces a stronger CO bond, leading to Pt^{n+}-CO bands appearing at higher frequencies. Ivanova et al. (2007) state that Pt^{4+} is coordinatively saturated, preventing CO binding. Pt^{3+}, Pt^{2+} and Pt^{+} show bands around, respectively, 2183 cm^{-1}, 2134 cm^{-1}, and 2111 cm^{-1}.[31–33]

CO can adsorb in different configurations onto a Pt atom: linearly on top of one Pt atom, bridged on two Pt atoms, or in a three-fold hollow configuration on three Pt atoms. Corresponding Pt-CO bands are observed at 2000–2100 cm^{-1}, 1800–1970 cm^{-1}, and 1700–1770 cm^{-1}, respectively.[34] Increased CO coverage causes more linear CO adsorption. The band position will also shift to higher wavenumbers with higher CO coverage due to CO-CO dipole coupling. Dipole coupling between CO adsorbed on different sites, such as terrace and edge sites, induces intensity transfer from low to high-frequency vibrations, shifting the Pt-CO band to the high-frequency. The different contributions of the different sites become, therefore, less apparent.[35]

Furthermore, CO-CO dipole coupling explains why temperature influences the band position, as higher temperatures lead to CO desorption from Pt NPs, reducing CO coverage. CO desorption starts from {111} facets, followed by {100} facets, edges, and corners due to stronger bonding.[24] Consequently, the Pt-CO band shifts to lower wavenumbers at higher temperatures. This necessitates a consistent temperature at which all DRIFTS CO adsorption measurements are performed.

Moreover, CO can adsorb on the edges, corners, or terraces of the Pt NPs, with preferential adsorption on corners, followed by edges, and lastly, on terraces.[36] The difference between these sites is the amount of nearest neighbours (NN) of the Pt, known as the coordination number (CN). Corner sites have 3 NN, edges 5 NN, and the coordination number of terraces depends on the facets. The CN of different facets increases from 110 < 100 < 111, with 7, 8, and 9 NN, respectively. This difference in coordination number affects the Pt-CO band position.

Kappers et al. (1991) established a linear relationship between the Pt coordination number and the Pt-CO band position, with increasing coordination numbers resulting in higher wavenumbers for the Pt-CO band. In conclusion, {111} facets with a coordination number of 9 exhibit a higher wavenumber for the Pt-CO band compared to {100} facets (CN = 8).[37] The Pt{111}-CO band can be found in the range of 2087–2096 cm^{-1}, while the Pt{100}-CO can be found in the range of 2077–2084 cm^{-1}.[37–39] Additionally, uncoordinated sites like edges and corners (CN = 3–6) show a Pt-CO band at lower wavenumbers, approximately 2000-2050 cm^{-1}.[37]

This site-dependent theory extends to nanoparticle size. In smaller nanoparticles, most adsorption sites are corners or edges characterized by low coordination numbers. To study the site dependence of the Pt-CO band in FTIR spectroscopy, nanoparticles should be sufficiently large to possess numerous terrace adsorption sites. Recent research (Figure 3) revealed that when nanoparticles average around 10 nm, CO adsorbs equally on well-coordinated sites (terraces) and under-coordinated sites (corners and edges).[27] Consequently, this study aims for nanoparticles with an average size above 3 nm to ensure enough signal from terraces.

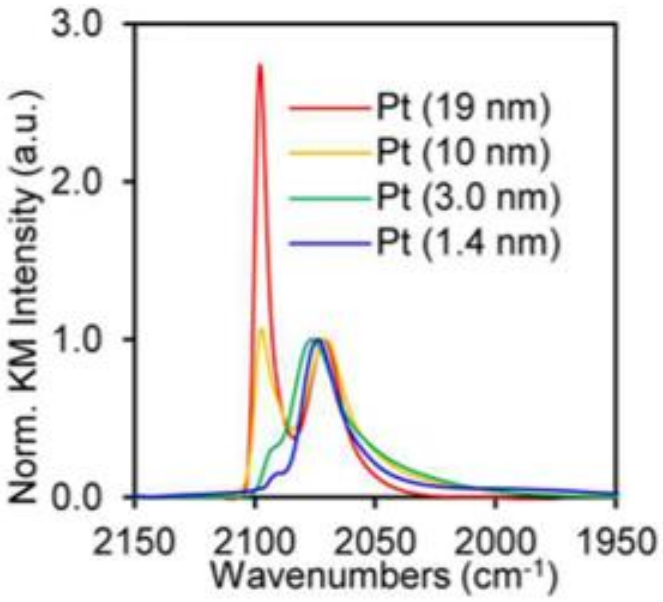

Figure 3 DRIFT spectra of CO adsorbed on various Pt NP sizes at 298K. Adapted from Kale et al. (2016).[27]

2.2. Colloidal nucleation and growth

Classical Nucleation Theory (CNT) is the predominant theoretical model to describe nanoparticle nucleation. CNT assumes that a particle is a small piece of bulk matter in a supersaturated solution, consequently possessing a surface tension equivalent to macroscopic bulk. A solution attains supersaturation when the solute concentration exceeds the concentration expected at thermodynamic equilibrium. Pt nanoparticle formation is a homogeneous nucleation, as there is only one type of solute, the platinic acid (or Pt atoms). When Pt seeds are introduced in the reaction, it is a heterogeneous nucleation, as it acts as a foreign cluster.[40] In this section, homogeneous nucleation is assumed.

Upon clustering of Pt atoms, the cluster is unstable at first. The stability of the Pt cluster depends on the total Gibbs free energy change occurring during nucleation, which comprises two contributions, surface and bulk contributions (Equation 1).

$$\Delta \boldsymbol{G} = \Delta \boldsymbol{G}(\boldsymbol{bulk}) + \Delta \boldsymbol{G}(\boldsymbol{surface}) \quad (1)$$

Expansion of the total surface area increases the total Gibbs energy, as depicted by Equation 2.

$$\Delta \boldsymbol{G}(\boldsymbol{surface}) = \boldsymbol{\gamma \beta} (\boldsymbol{v_m N})^{\frac{2}{3}} \quad (2)$$

Here, γ is the surface tension in N m^{-1}, β is the proportionality constant depending on the clusters' shape, v_m is the monomer volume in m^3, and N is the cluster's number of monomers. The proportionality constant for spheres, cubes, and octahedrons are 4.84, 6, and 5.72, respectively. The calculations for this can be seen in Appendix A.

Conversely, the bulk term of the total Gibbs free energy can be described by the multiplication of the number of monomers (N) with the chemical potential difference between the bulk phase and the supersaturated solution ($\Delta\mu$), as shown in Equation 3. The total Gibbs free energy depends on $\Delta\mu$, which can be derived from the formula for the chemical potential of an ideal, non-interacting solute, given in Equation 4. The expression for $\Delta\mu$ is given in Equation 5.

$$\boldsymbol{\Delta G}(\boldsymbol{bulk}) = -\boldsymbol{N}|\boldsymbol{\Delta \mu}| \quad (3)$$

$$\boldsymbol{\mu} = \boldsymbol{\mu_0} + \boldsymbol{k_B T} \ln\left(\frac{\boldsymbol{c}}{\boldsymbol{c_0}}\right) \quad (4)$$

$$\boldsymbol{\Delta \mu} = -\boldsymbol{k_B T} \ln\left(\frac{\boldsymbol{c}}{\boldsymbol{c}(\boldsymbol{sat})}\right) = -\boldsymbol{k_B T} \ln(\boldsymbol{S}) \quad (5)$$

Here, c is the solute concentration, μ_0 is a reference chemical potential for reference concentration c_0, c(sat) is the saturation concentration, k_B is the Boltzmann constant, T is the temperature, and S is the degree of supersaturation.[41]

The bulk term is negative, as it reduces the total free Gibbs energy and is the driving force for the nucleation. Thus, when a particle only consists of very few Pt atoms, the surface term surpasses the bulk term, rendering particle formation energetically unfavourable. Equilibrium between the bulk term and the surface term in Equation 1 indicates that the cluster has become stable, and the corresponding size is called the critical size (r^*). The relationship between these terms can be seen in Figure 4.

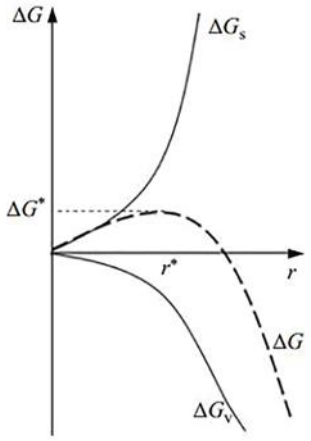

Figure 4 Graph of total free Gibbs energy plotted against cluster size. The positive surface and negative bulk contributions can be seen, resulting in a Gibbs energy maximum at the critical nucleus size. Adapted from Wang et al. (2023). [82]

When the critical size is reached, the total free Gibbs energy is at its highest, referred to as the activation free energy (Equation 6).

$$\boldsymbol{\Delta G^{*} = \frac{d\Delta G}{dN} = 0} \qquad (6)$$

Combining Equations 1–6 shows that the activation barrier depends on the supersaturation of the solution. Supersaturation renders cluster formation thermodynamically spontaneous. However, a cluster always wants to lower its free Gibbs energy. Before a cluster attains the critical size, it is energetically unfavourable to grow, leading to (partial) dissolution.[42] This, in turn, leads to the bigger stable particles growing even more, a phenomenon called Ostwald ripening.[43] When particles have reached the critical size, to lower the total free Gibbs energy, it is energetically favourable to grow.

Additionally, the activation barrier, and therefore also the critical size of a cluster, depends on the proportionality constant. The difference between the cubes and octahedron proportionality constant is small (6 vs 5.72). Therefore, the critical size and activation barrier will not differ much when either cubes or octahedrons are synthesized.

As the monomer concentration depletes during nucleation, resulting in cluster formation, the supersaturation of the solution decreases. Consequently, fewer new clusters form and the growth of already established clusters is more energetically favourable. This is called the growth stage. The deposition of a monomer onto a cluster can be classified into two categories: reaction-limited growth and diffusion-limited growth. [44] Reaction-limited growth occurs when monomer adsorption onto the growing cluster is the rate-determining step. In contrast, diffusion-limited growth designates the rate-determining step as the monomer reaching the growing cluster. According to Varghese N. and Rao C. (2012), when a capping agent is utilized during platinum nanocluster nucleation, both diffusion and surface reaction contribute to the growth rate.[45]

2.3. The polyol synthesis

The polyol synthesis, first introduced by Fiévet, Lagier and Figlarz in the late 80's,[40] constitutes a method for synthesizing nanoparticles from metal oxides, hydroxides or salts using polyols. It is a particularly powerful method of producing metal nanoparticles of diverse shapes. According to Wulff's theorem, an fcc metal will inherently assume a truncated octahedron shape in vacuum due to its maximum stability.[46] However, when metal nanoparticles are formed in a solution phase, the equilibrium shape can be altered, allowing for the creation of nanoparticles with different shapes and morphologies.

Polyols, defined as alcohols with at least two alcohol groups, act as both the solvent and the reducing agent in polyol reactions.[21] The utilization of polyols offers several advantages:

- Polyols have a high boiling point, allowing high reaction temperatures;
- They are viscous, making the reaction a diffusion-limited reaction;[47]
- They stabilize the formed metal nanoparticles by coordinating with the metal nanoparticles, reducing the amount of aggregation.[21] The polyol will first be deprotonated by a base, after which it will coordinate with the metal nanoparticles via the deprotonated hydroxyl group.[48]

The choice of polyol significantly impacts the resulting nanoparticles. Larger polyols correspond to lower oxidation potentials, necessitating higher reaction temperatures. Biacchi et al. (2011) demonstrated that varying the polyol influences the uniformity of resulting nanoparticles.[49] In this research, ethylene glycol was used as the polyol. The oxidation scheme of ethylene glycol is shown in Figure 5.

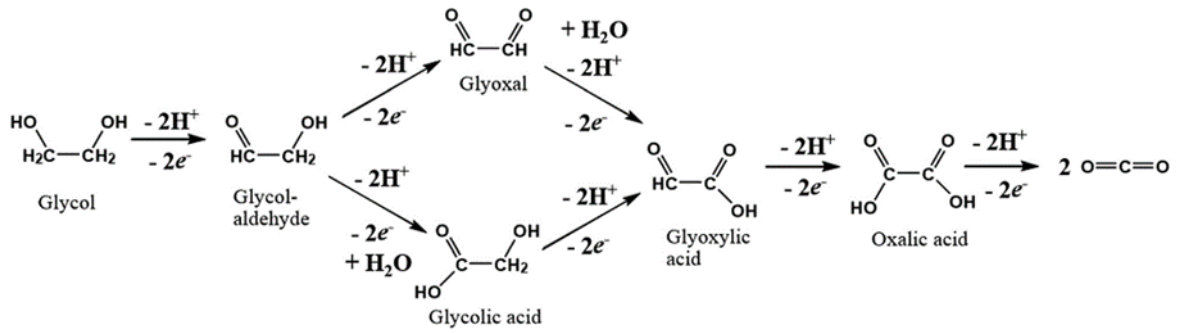

Figure 5 Oxidation mechanism of ethylene glycol. Adapted from Livshits et al. (2008).[83]

It is noteworthy that the reaction temperature influences which oxidation product of ethylene glycol reduces the metal precursor.[50] In this research, reaction temperatures above 160 °C were used, causing the ethylene glycol to be dehydrated to acetaldehyde. The acetaldehyde will then reduce the platinum according to Equations 7 and 8.

$$HOCH_2CH_2OH \rightarrow CH_3CHO + H_2O \quad (7)$$

$$2n\ CH_3CHO + 2\ Pt^{n+} \rightarrow 2\ Pt^0 + n\ CH_3COCOCH_3 + 2n\ H^+ \quad (8)$$

When the metal precursor encounters the polyol at an elevated temperature, the polyol reduces the metal precursor to the metallic state. However, the sequence of steps remains uncertain. Unreduced metal precursors might initially cluster together and subsequently undergo reduction. Alternatively, the metal precursors may need to be reduced individually before forming clusters with other reduced metal atoms.[46] Thus, the application of CNT might not be straightforward in this particular case. Whether a high concentration of the platinum

precursor or a high concentration of reduced platinum causes supersaturation of the solution and, therefore, cluster formation needs further research.

The reduction kinetics influences the shape of the clusters during nucleation, a process influenced by various factors: reaction temperature, oxidation state of the metal precursor, strength of the reducing agent, pH, and reactant concentration. A fast reduction rate is often considered a thermodynamically controlled reaction, yielding shapes with the lowest total Gibbs free energy. For fcc crystals this is the aforementioned truncated octahedrons. On the contrary, a slow reduction rate, considered a kinetically controlled reaction, provides shape-directing agents more time to interact with metal clusters, resulting in shapes more sensitive to the reaction conditions and shape-directing agents.[8,51]

Metal seeds up to 2.5 nm predominantly adopt the lowest thermodynamically energetic shape, the truncated octahedron. Beyond this size, other shapes begin to form.[52] When the shape is determined, the NPs can keep growing by the addition of metal monomers. The platinum atoms will deposit on the corners of the growing platinum nanoparticles as that are the highest energy sites of the particle. It will then diffuse on the surface until it finds a step site where it can be incorporated.[46] The rate of this deposition can be greater or smaller than the rate of surface diffusion on the nanoparticle, influencing the final nanoparticle shape. If the deposition rate is higher than the surface diffusion rate, the deposited atom will become trapped on the corner beneath a newly deposited Pt atom. Shapes with spikes on the corners are the resulting shape. If the deposition rate is smaller than the surface diffusion rate, it will result in conformal growth.[53]

Ridges can also form if the diffusion rate in the solvent is slow compared to the rate at which a growth unit is adsorbed onto the particle surface. In such cases, a supersaturation gradient occurs as the supersaturation at the particle surface is low and increases with distance from the particle. If a ridge forms on the particle's surface, it will have a slightly higher supersaturation at the top of the ridge than at the base. Then, the supersaturation gradient will encourage the growth on the ridge.[19,51]

To further control the final shape of the NPs, specific facets can be stabilised using additives that act as structure-directing agents. They adsorb selectively on specific facets of metal nanoparticles, either stabilising this facet or promoting their growth, influencing the prevalence of facets on the final nanoparticles.[51] With platinum nanoparticles, silver nitrate ($AgNO_3$) is often used as a structure-directing agent. The silver ion adsorbs more selectively on {100} facets than on {111} facets. This is likely caused by the higher desorption energy of reduced Ag species on the kinetically stable Pt{100} facet compared to thermodynamically favoured Pt{111}.[54] According to Song et al. (2005)[23], the Pt salts were reduced spontaneously with the oxidation of adsorbed Ag species – reduced by the polyol first – on the (100) surface by the following favourable electrochemical reaction (Equation 9):

$$\mathbf{4}\,\boldsymbol{Ag} + \boldsymbol{H_2PtCl_6} \rightarrow \mathbf{4}\,\boldsymbol{AgCl} + \boldsymbol{Pt}(\mathbf{0}) + \mathbf{2}\,\boldsymbol{HCl} \qquad (9)$$

The enhanced growth rate along the (100) direction is attributed to the dissolution of AgCl into the solvent.[23] The adsorbed Ag on the Pt{100} seed is continuously exchanged with $[PtCl_6]^{2-}$ through a galvanic displacement process. In this process, Pt precursor ions undergo spontaneous reduction by the oxidation of adsorbed silver to silver chloride.[54]

However, conflicting reports on the shape-directing effect of Ag^+ have been reported. Safo *et al.* (2019) conducted experiments where the PVP concentration was varied while maintaining a constant Ag concentration. Surprisingly, deviations from the PVP concentration of 4M resulted in a notable increase in the occurrence of different shapes, such as tetrahedral, irregular and spherical NPs. Monodispersity was also found to decrease with different PVP concentrations. Intriguingly, the size of the NPs remained relatively unchanged, suggesting a minor influence of the PVP concentration on the growth process of NPs.[54] These findings imply that the concentration of the ligand, in this case, polyvinylpyrrolidone (PVP), is the actual structure-directing agent in this reaction. Whether PVP or $AgNO_3$ is – or both are – the structure-directing agent(s) is still conflicted.

Numerous reports support the role of PVP as a structure-directing agent in the reaction. Ye et al. (2016) discovered that at low PVP loadings, PVP selectively adsorbs on Pt{111} facets rather than Pt{100} facets. Stabilizing the Pt{100} facets over the Pt{111} facets results in the formation of cubic nanoparticles.[55] Moreover, the molecular weight of the PVP contributes to its role as a structure-directing agent. A study with varying PVP molecular weights demonstrated the creation of different silver nanoparticle shapes. Their conclusion was that PVP with a smaller molecular weight has less steric strain and thus has the strongest adsorption interaction between the PVP and silver. However, the drawback is that because of the short chains, there is no full coverage of the PVP on the NP, causing aggregation.[56] Another difference between low and high molecular weight is their binding to the NP; high molecular weight PVP binds to the NP via its O atom, while low molecular weight PVP binds to the NP at two sites, the O and N atoms.[56]

The particle size can be controlled by adjusting the reduction kinetics. Fast reduction results in numerous small clusters, eventually growing into small NPs. Slow reduction produces fewer clusters that grow into larger NPs.[51] One way to influence the reduction kinetics is by changing the pH of the solution. One study found that a higher pH decreases the particle size.[57] Another way is to add the ligand later in the reaction so that the NPs aggregate more at the beginning, forming larger NPs.

2.4. Characterisation techniques

2.4.1. Transmission Electron Microscopy

Visible light microscopy, with a resolution of up to 300 nm, approximately corresponding to 1000 atoms in a row, is surpassed by electron microscopy.[58] To achieve higher resolutions, electrons can be used instead of light. Electrons have the same wave-particle duality as light but have a smaller wavelength, less than an Ångstrom.[59] Additionally, the wavelength decreases when the electron has a higher velocity.[60] This allows Transmission Electron Microscopy (TEM) to achieve high resolutions by applying high voltage to accelerate electrons.

In TEM, when the electron beam encounters a sample, some electrons pass through the sample without losing energy, while others are scattered by atoms of the sample. They can be scattered either elastically or inelastically. Elastic scattering involves no transfer of kinetic energy to the atoms, whereas inelastic scattering results in a loss of kinetic energy to the sample, posing a risk of sample damage. This does not happen often because electrons are predominantly scattered elastically as the mass of the electron and atom have a significant difference.[60]

Transmission electron microscopes consist of an electron gun, electromagnetic lenses, a sample holder, and a detector; a schematic drawing is shown in Figure 6. The electron gun is often a thermionic gun, with materials that are heated up enough to overcome the energy barrier of releasing electrons. A tungsten filament is often used, heated up to 3000–3500 °C. When the electrons are released, they are accelerated with an anode at voltages of up to 200 kV. The electron beam is then focused onto the sample with a condenser lens.

Upon interaction with the sample, the electrons are scattered. An objective lens collects the scattered electrons and makes an intermediate picture. The aperture in the objective lens can adjusted to different sizes, allowing control over the collection of diffracted electrons. Choosing a small aperture enhances the image contrast by excluding electrons with large diffraction angles. A heavy atom has more protons, thus deflecting the electron's path more. When the objective lens removes these electrons from the electron beam, the Pt will appear darker in the picture.[60]

Subsequent lenses will then magnify the intermediate image, the intermediate lens and the projector lens, with a potential magnification of up to 1.5 million times. Finally, the magnified image reaches a detector, often a slow-scan charge-coupled device (CCD) camera, which converts the information from the electrons to a detailed pictured.[61]

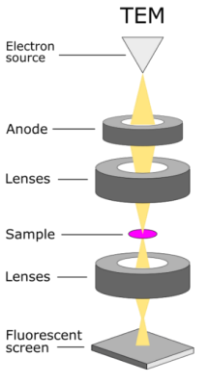

Figure 6 Schematic diagram of a Transmission Electron Microscope.

2.4.2. Diffuse Reflectance Infrared Fourier Transform Spectroscopy

Diffuse Reflectance Infrared Fourier Transform Spectroscopy (DRIFTS) is a specialized technique within Fourier Transform Infrared Spectroscopy (FT-IR). FT-IR uses infrared (IR) light to characterise functional groups in a molecule. Infrared light is light with a wavelength (λ) between 780 nm and 1 mm and can be divided into three distinct regions: near-infrared, mid-infrared and far infrared. FT-IR experiments typically employ mid-infrared light (MIR) with wavelengths ranging from 2500 to 25000 nm.[62] However, it is more commonly expressed in wavenumbers ($\tilde{\nu}$), defined as the number of wavelengths per unit distance (Equation 10).

$$\tilde{\boldsymbol{\nu}} = \frac{\mathbf{1}}{\boldsymbol{\lambda}} \tag{10}$$

Although infrared light lacks the energy to excite electrons, it can excite vibrational motions in molecules. Molecules can have up to six different types of vibrations known as normal modes: symmetric stretch, antisymmetric stretch, bending vibration, rocking vibration, wagging vibration, and twisting vibration. However, not every normal mode can absorb the energy from an IR photon. The vibration must cause a dipole moment change of the molecule. Then, the vibration is IR-active. Additionally, a vibration is only excited when the energy of the IR light exactly matches the vibration energy. Therefore, each vibration occurs at a specific frequency depending on the chemical bond and atoms involved in that bond. The wavenumber of the corresponding band position in an FT-IR spectrum can be calculated using Hooke's law (Equation 11):

$$\tilde{\boldsymbol{\nu}} = \frac{\mathbf{1}}{\mathbf{2}\boldsymbol{\pi c}}\sqrt{\frac{\boldsymbol{k}}{\boldsymbol{\mu}}} \tag{11}$$

Here, c is the speed of light in m s^{-1}, k is the force constant or bond strength in N m^{-1}, and μ is the effective mass in kg (Equation 12).

$$\boldsymbol{\mu} = \frac{\boldsymbol{m_1 m_2}}{\boldsymbol{m_1 + m_2}} \tag{12}$$

An FTIR spectrometer illuminates the sample with a broadband infrared light source ranging from 4000 to 400 cm^{-1}. The sample absorbs light with frequencies corresponding to its vibrational bonds while the detector detects the frequencies of non-absorbed light. This information is then converted with a Fourier Transform from the time domain to the frequency domain. An FTIR spectrum is generated, with transmittance plotted against each wavenumber. Transmittance (T) is defined as the intensity of the light that is transmitted through the sample (I) divided by the intensity of the incident light (I_0). The absorbance (A) of the sample can then be calculated using $\mathrm{A} = \log\left(\frac{1}{T}\right)$.

There are different methods of shining the IR light on the sample. For example, in transmission, FTIR passes IR light through the sample. In DRIFTS, the technique relies on scattering the IR light from the sample. The light can be directly reflected from the surface (specular reflectance) or reflected multiple times within the sample itself (diffusely scattered light), as seen in Figure 7. The penetration depth depends on the measured sample's reflectance and absorbance. The sample then partially absorbs the IR light, and the reflected light goes to the detector.[63] Therefore, in this study, reflectance describes how much light is absorbed.

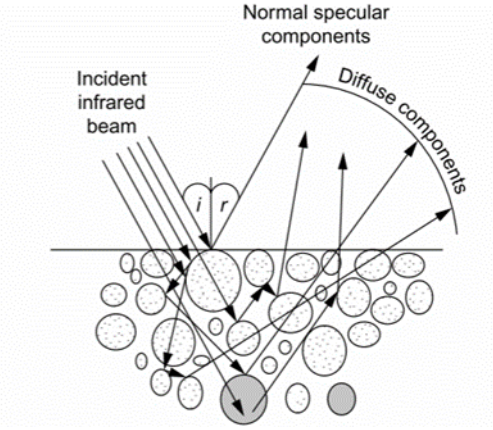

Figure 7 Scattering behaviour of IR light during DRIFTS spectroscopy. Adapted from Armaroli et al. (2004).[63]

Three different measurements are done while measuring the sample. First, a background measurement is done in inert gas with the sample in the sample holder (I_0). Second, the sample is dried in inert gas for approximately 1 hour, and another DRIFTS spectrum is taken (I_{cat}). Third, the sample is measured during CO adsorption measurements (I_{cat+CO}). The relative reflectance of the sample (R) can then be calculated by Equation 13.

$$\boldsymbol{R = \frac{I_{cat+CO}}{I_{cat}}} \qquad (13)$$

The absorbance of the sample can then be calculated in a similar way as using transmittance, $\mathrm{A} = \log\left(\frac{1}{R}\right)$. According to Sirita et al. (2007), $\log\left(\frac{1}{R}\right)$ is the best way to describe the adsorbate surface concentration when the relative reflectance is below 60%, which is valid for full CO coverage on Pt nanoparticles.[64]

The advantages of DRIFTS include the ability to analyse solid samples and non-transparent materials.[59] However, the sample must adhere to certain criteria for optimal results, such as homogenous particle size and uniform distribution of supported metal without aggregation.

3. Experimental

During this thesis, three different reports were reproduced to make different Pt nanoparticle shapes: Song et al. (2005),[23] Hu et al. (2006),[65] and Lee et al. (2006).[66] The objective was to determine which method was the most effective at making uniform Pt shapes. As the Song et al. procedure showed the most promising results, various alterations were made to this procedure to improve reproducibility and achieve more uniform shapes and sizes.

3.1. Chemicals

Chemical substance	Chemical formula or abbreviation	Purity	Supplier
Chloroplatinic acid hydrate	$H_2PtCl_6 \cdot 6\ H_2O$	~38% Pt basis	Sigma-Aldrich
Polyvinylpyrrolidone (mw: 40000)	PVP		Sigma-Aldrich
Silver nitrate	$AgNO_3$	99,9+%	Thermo Fisher Scientific
Ethylene glycol, anhydrous	1,2-Ethanediol	99.8%	Sigma-Aldrich
N-hexane	C_6H_{14}	99+%	Acros Organics
Ethanol	EtOH	100.0%	VWR Chemicals
Hexadecyltrimethylammonium bromide	CTAB	≥98%	Sigma-Aldrich
L-ascorbic acid	Vitamin C	99%	Sigma-Aldrich
Sodium borohydride	$NaBH_4$	>=96%	Sigma-Aldrich
Potassium tetrachloroplatinate	K_2PtCl_4	99.9%	Thermo Fisher Scientific
Silica gel, 35-60 mesh, 150Å	SiO_2	Davisil Grade 646	Sigma-Aldrich

Table 1 Overview of the chemicals used during the experiments, their purity and where they were purchased.

3.2. Equipment

DRIFTS measurements

Diffuse Reflectance Infrared Fourier Transform Spectroscopy measurements were performed with a Bruker Tensor 37 FT-IR spectrometer with an MCT detector. Thirty-two scans were recorded and averaged every minute with a resolution of 1 cm^{-1}. The experiments were carried out in The Praying Mantis™ High Temp. Reaction Chamber. The dome used had ZnSe windows. The reactants were introduced through Bronkhorst EL-FLOW Mass Flow Controllers (Figure 8).

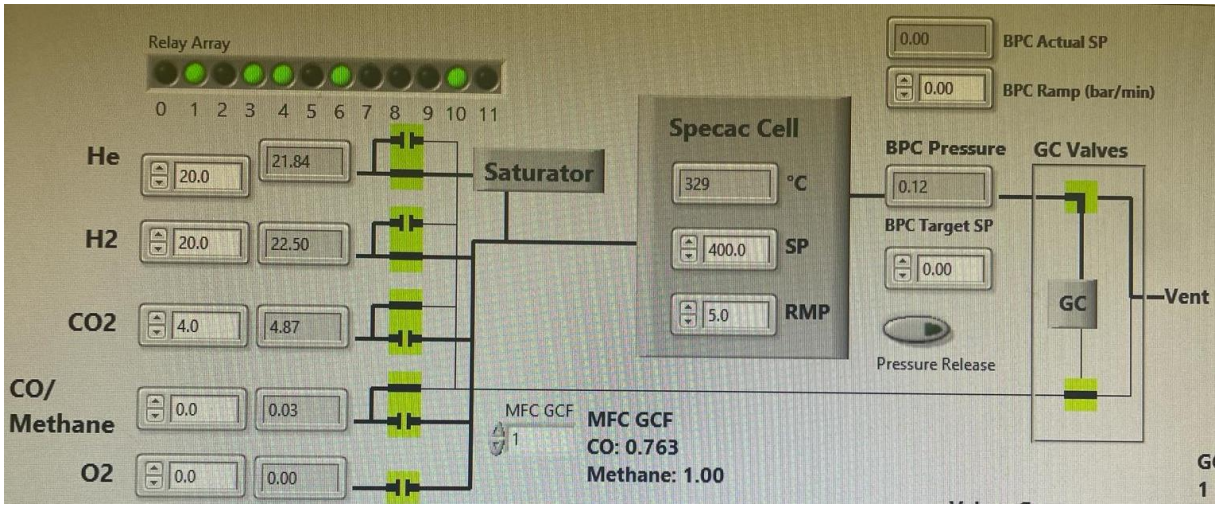

Figure 8 Labview overview of the DRIFTS setup. On the left is shown in which order the gasses are connected to the DRIFTS cell. The O_2 gas can be switched to Ar gas, similarly as the CO and methane gasses are interchangeable. The shown values are not from measurements for this research.

TEM measurements
Transmission Electron Microscopy was performed with either an FEI Talos F20 or an FEI Talos L120. The former was operated at an accelerating voltage of 200 kV, while the latter was operated at 120 kV. The TEM samples were drop cast on a Formvar/carbon-coated copper grid (300 mesh).

HAADF HR STEM measurements
High-Angle Annular Dark-Field High-Resolution Scanning Transmission Electron Microscopy measurements were performed using a double aberration corrected Spectra 300, operated at an acceleration voltage of 300 kV and equipped with an EDX detector.

TGA measurement
Thermal Gravimetric Analysis measurements were performed with a Perkin Elmer TGA 8000. The sample was added to the crucible as a suspension in ethanol and left to dry overnight. The next day, it was heated to 800 °C at 5.00C/min in an O_2 flow of 45.0 mL/min.

UV-Vis measurements
Ultraviolet-visible spectroscopy measurements were performed with an Agilent Cary 60 UV-Vis scanning Spectrophotometer. A quartz cuvette with an optical pathlength of 1 cm was used. A scan rate of 24000 nm/min was used, with data intervals of 5 nm.

3.3. Synthesis of Pt nanoparticles
Forty-two syntheses were done to optimise the synthesis of Pt Nanoparticles. Table 2 gives an overview of the syntheses and which variables were changed: which report was reproduced, which shape was the goal, reaction temperature, heat source, stirring rate, and additional comments if something else was changed. In this thesis, the syntheses will be referred to as S, followed by the synthesis number described in Table 2. In Sections 3.3.1. – 3.3.3. the three different synthesis methods will be explained. The same purification steps were applied to all three synthesis methods, detailed in Section 3.3.4.

Overview of synthesis parameters

#	Paper	Shape	T (°C)	Heat source	Stirring rate (rpm)	Other alterations
1	Song	C	180	HP	460	
2	Song	C	180	HP	460	
3	Song	C	180	HP	460	
4	Song	O	180	HP	430	
5	Song	O	180	HP	430	
6	Song	CO	180	HP	430	
7	Song	C	180	HP	430	PVP and H_2PtCl_6 mixed
8	Song	C	200	HP	430	
9	Song	C	200	HP	430	Slower drop rate of the syringe pumps
10	Song	C	200	HP	430	No $AgNO_3$ added
11	Song	C	200	HP	430	N_2 atmosphere
12	Song	C	200	HP	390	N_2 atmosphere
13	Song	C	200	HP	360	PVP and platinic acid are added with syringes every 30 seconds
14	Hu	C	200	HP	400	
15	Hu	C	200	HP	400	
16	Song	C	200	HP	360	
17	Song	C	200	HP	0	
18	Song	C	200	HM	1170	
19	Song	C	200	HP	950	
20	Song	O	200	HM	450	
21	Lee	C	60	HP	500	
22	Lee	C	90	HP	1180	
23	Song	O	200	HM	1150	
24	Lee	C	70	HP	430	
25	Song	C	200	HM	1170	Tubing instead of needles
26	Song	C	200	HM	1170	PVP and platinic acid are added with Finn pipettes every 30s
27	Song	O	200	HM	1170	PVP and platinic acid are added with Finn pipettes every 30s
28	Song	C	200	HM	1170	Tubing instead of needles
29	Song	C	200	HM	1170	Tubing with larger inner d
30	Song	O	200	HM	1170	Tubing with larger inner d
31	Song	O	200	HM	1170	Tubing with larger inner d, slower drop rate syringe pumps
32	Song	C	200	HM	1170	Tubing with larger inner d, PVP added to flask before reaction
33	Song	C	200	HM	900	Reaction at two different T
34	Song	C	200	HM	900	PVP added to flask before reaction
35	Song	C	160	HM	530	PVP and platinic acid were mixed before the reaction started, added with Finn pipettes every 30 seconds
36	Song	O	160	HM	530	Identical to synthesis 35
37	Song	O	160	HM	530	Identical to synthesis 35
38	Song	O	200	HM	530	Identical to synthesis 35
39	Song	O	180	HM	530	Identical to synthesis 35
40	Song	C	180	HM	530	Identical to synthesis 35
41	Song	O	180	HM	530	Identical to synthesis 35
42	Song	C	200	HM	530	Identical to synthesis 35

Table 2 Overview of all syntheses performed during this thesis and what parameters were changed: which paper was reproduced, the desired shape: cubes (C), octahedrons (O), or cuboctahedrons (CO), reaction temperature, heat source: heating plate (HP) or heating mantle (HM), stirring rate, and other alterations compared to the respective paper.

3.3.1. Polyol synthesis – Song et al. (2005)

3.3.1.1. Preparation of precursor solutions

Three precursor solutions were prepared to reproduce the paper of Song et al. (2005).[23] The platinic acid precursor solution was made by dissolving 0.8093 g of platinic acid in 25 mL of ethylene glycol. 1.0609 g of PVP was dissolved in the same ethylene glycol volume for the PVP precursor solution.

To create different molar concentrations of silver nitrate precursor solutions, different amounts of silver nitrate were dissolved in 25 mL ethylene glycol. Specifically, 0.0085 g (0.002 M), 0.0850 g (0.02 M), and 0.2550 g (0.06 M) of silver nitrate were dissolved to produce the solutions dedicated for cubes, cuboctahedrons, and octahedrons, respectively.

Subsequently, all solutions were sonicated to ensure homogeneity. All solutions were wrapped in aluminium foil and stored in the fridge. This was done to prevent the ethylene glycol from reducing platinum or silver with energy from heat or light.

3.3.1.2. Synthesis method

The synthesis setup can be seen in Figure 9. 2.5 mL ethylene glycol was added to a 50 mL round bottom flask with three necks. On top, there was a reflux condenser, and the side necks were connected to a KD Scientific 100 syringe pump each. The heating plate was set to 200 °C, and a Heat-On attachment was placed on top in which the thermometer was placed. The solution was stirred at 430 rpm. The temperature stabilised at 180 °C, after which it was refluxed for an additional five minutes.

Then 0.05 mL of the silver nitrate was added, 0.002 M, 0.02 M, or 0.06 M for cubes, cuboctahedrons, or octahedrons, respectively. Immediately after, the syringe pumps were started. A 3 mL syringe was placed upon both syringe pumps, connected with a long needle pierced through a septum to the round bottom flask. In one 3 mL syringe, there was 3 mL PVP; in the other 3 mL syringe, there was 1.5 mL platinic acid. The settings of the syringe pumps were as follows:

Diameter	= 11 mm			
Volume	= 1,5 mL	[Platinic acid]	3 mL	[PVP]
Rate	= 5.63 mL/h	[Platinic acid]	11.25 mL/h	[PVP]

In total, it took 16 minutes to empty both syringes fully. The platinic acid and PVP were added in a molar ratio of 1:6. After 16 minutes, the solution was stirred and refluxed for five more minutes. Then, the heating plate was turned off, and the solution was cooled in air to room temperature.

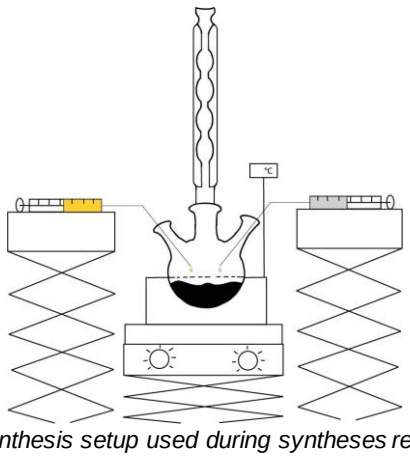

Figure 9 Schematic diagram of the synthesis setup used during syntheses reproduced from Song et al. (2005).[23]

3.3.2. Seed-mediated synthesis – Hu et al. (2006)

3.3.2.1. Preparation of precursor solutions

Five stock solutions were made to reproduce the report from Hu et al. (2006).[65] For the first precursor solution, 0.9150 g CTAB and 0.0093 g platinic acid were dissolved in 25 mL ultrapure water (upw). The second precursor solution was created by dissolving 0.9150 g CTAB and 0.0084 g platinic acid in 20 mL upw. Then, 0.0078 g silver nitrate was dissolved in 2 mL upw. 43.55 µL of this silver nitrate stock solution and an additional 4.956 mL upw were added to the second precursor solution. Lastly, 17.6 mg ascorbic acid was dissolved in 1 mL upw, and 0.0011 g sodium borohydride was dissolved in 3 mL upw.

3.3.2.2. Synthesis method

10 mL of the first stock solution was added to a 50 mL three-necked round bottom flask. The flask was heated to 60 °C and stirred at 400 rpm. When it reached 60 °C, it was kept at this temperature for an additional 7 minutes. Then, 1.3 mL of the sodium borohydride stock solution was added with a 3 mL syringe. The stirring rate was increased to 600 rpm for 5 minutes before being lowered to 200 rpm while the heating source was removed. After 10 minutes, it was put back on the heating plate, with the heating plate set at 50 °C. According to the report, the temperature has to be kept at 25 °C.

In another round bottom flask, 10 mL of the second stock solution was added with 0.42 mL of the ascorbic acid stock solution. This was heated to 60 °C and stirred at 400 rpm. When it reached 60 °C, it was kept at that temperature for 5 minutes. Then, 50 µL of the Pt seeds that were just made and kept at 25 °C were added to this solution. The flask was shaken for a minute, and the content minus the foam was transferred to a glass vial. The Pt seeds that were not used were stored in the fridge wrapped in aluminium foil.

The glass vial was put into an aluminium heating block and kept at room temperature for 48 hours, stirring at 500 rpm. After 48 hours, there was a two-layer system: a white transparent solid supernatant and a "yellow" solid precipitate. It was shaken, and the stirring rate was increased to 900 rpm. After another four days, the colour became light grey. The solution was stirred for an additional seven days. After 13 days, the solution had become darker and was not transparent.

It was centrifuged for 10 minutes at 4000 rpm. There was a white precipitate (CTAB) and a black transparent supernatant. The precipitate was removed. The centrifugation was repeated till there was no separation anymore. Afterwards, the regular washing steps were followed, as described in Section 3.3.4.

The second time this synthesis was reproduced, the Pt seeds of the first time were used again. The Pt seeds were taken out of the fridge beforehand to bring to room temperature. The only change was that the aluminium heating block was heated to 30 °C without stirring. It was kept there for six days. The solution became yellow/brown with a white precipitate. Only the supernatant was centrifuged at 3500 rpm for 5 minutes. There was a black precipitate and yellow/brown supernatant. The supernatant was repeatedly centrifuged till there was little to no separation anymore. Then, the regular washing steps were followed.

3.3.3. Morphology control by adjusting reduction method – Lee et al. (2006)

3.3.3.1. Preparation of precursor solutions

To reproduce the report of Lee et al. (2006),[66] 0.0042 g potassium tetrachloroplatinate and 0.3645 g CTAB were dissolved in 10 mL upw. A second precursor solution was created by dissolving 0.0113 g sodium borohydride in 500 µL upw.

3.3.3.2. Synthesis method

The potassium tetrachloroplatinate solution was heated to 50 °C while stirring at 500 rpm. When it reached 50 °C, it was kept at that temperature for 5 minutes. It became increasingly more transparent with time. After 5 minutes, the sodium borohydride solution was added. A glass stopcock was placed on one of the necks of the round bottom flask, through which the formed H_2 gas could be released. The stopcock was turned open the whole time. The solution was kept at 50 °C for 4.5 hours when the colour still had not changed. So, the temperature was increased to 60 °C, and aluminium foil was added around the round bottom flask. After another 1.5 hours, the heat was turned off, and the solution was light brown. The flask was then flushed with N_2 gas for 15 minutes. After centrifugation, there was almost no product left.

On the second try, this synthesis was done at 60 °C from the start. When adding the sodium borohydride, the temperature was 66 °C. After 3.5 hours, the solution was still yellow/light brown. The temperature was then increased to 120 °C for 30 minutes, after which it was decreased to 90 °C for another 1.5 hours. Then, the heat source was removed and flushed with N_2 for 15 minutes.

The product was centrifuged for 30 minutes at 3000 rpm. There was a black supernatant and black precipitate. The supernatant was centrifuged at 4000 rpm for another 30 minutes. Again, a two-layer system was created with a black precipitate and supernatant. After this, the regular washing steps were followed, as explained in Section 3.3.4.

The third time the synthesis was carried out, the temperature was set at 70 °C the whole time, stirring at 430 rpm. Three hours after adding sodium borohydride, the colour turned dark brown. After an additional three hours, the colour turned black. The same washing steps as before were applied.

3.3.4. Purification

After each synthesis for every synthesis method, the solution was transferred from the round bottom flask into a plastic vial when the product was cooled to room temperature. It was centrifuged at 4000 rpm for 15 minutes. A two-layer system was created: a black, solid-like precipitate and a black, liquid supernatant. This step is there to remove the solvent from the Pt NPs. Acetone was added to the supernatant in a ratio of 3:1, approximately 30 mL. This was centrifuged at 3000 rpm for five minutes. It separated into a black precipitate and often light-yellow supernatant. The supernatant was centrifuged longer if it was not clear and transparent after one round.

The resulting precipitate was dissolved in ethanol with sonication. Hexane was then added in a ratio of 3:1. In general, it was dissolved in 3 mL ethanol, and 9 mL hexane was then added, approximately. This solution was centrifuged at 3000 rpm for five minutes and gave a black precipitate and clean, transparent supernatant. This washing process was done three times in total. At the end, the Pt NPs were dissolved in 3 mL ethanol unless this was insufficient.

3.4. Different parameters

As the syntheses reproduced from the report of Song et al. gave the best results, different reaction parameters were changed for optimal results. An overview of the differences is given in Table 2.

Synthesis #7

To evaluate the effect of adding the PVP and platinic acid separately, they were added together in this synthesis. The PVP and platinic acid stock solutions, 3 mL and 1.5 mL, were mixed before the reaction. This mixture was added with one syringe pump with the following settings:

Diameter = 12.50 mm
Volume = 4.8 mL
Rate = 18 mL/h

Everything was added after dripping for 15 minutes.

Synthesis #8

Before this synthesis, the temperature of the heating plate was set at 200 °C. However, heat is lost because it is not perfectly insulated, and the round bottom flask never reached above 180 °C. During synthesis #8, the heating plate was set at a higher temperature than needed, namely 270 °C. This temperature increase would also increase the surface diffusion rate, aiming for less spikes forming on the nanoparticles' corners. Implementing this change led to the heating block reaching a temperature of 200 °C, and from this point onwards, this temperature was always used during the syntheses unless stated otherwise.

Synthesis #9

Another way to reduce the chance of spikes forming on the nanoparticles' corners is by reducing the atom adsorption rate. This was tried by increasing the total addition time of the PVP and platinic acid. The syringe pumps were set to a slower drop rate, resulting in the addition of the ligands and precursor taking 90 minutes in total. The diameter and volume settings of the syringe pumps were kept the same, but the drop rate was changed as follows:

Drop rate of PVP stock solution = 2 mL/h
Drop rate of platinic acid stock solution = 1 mL/h

Synthesis #10

Silver nitrate was not added in this synthesis to see the effect of silver nitrate on the platinum nanoparticles' shape. After the 5-minute reflux of ethylene glycol, the syringe pumps containing the ligand and precursor were started.

Synthesis #11 and #12

A nitrogen environment should increase the reaction kinetics, leading to more cubes. Therefore, synthesis #11 and #12 were performed under a N_2 atmosphere. Nitrogen gas was connected via a tube with a needle at the end pierced through a septum on the side neck of the 50 mL round bottom flask. As seen in Figure 9, the gas was leaving the flask via the reflux condenser, which was connected to a bubbler. The N_2 gas was added from the beginning. When the reaction temperature was stabilised at 200 °C, the N_2 bubbling was stopped.

Synthesis #13, #26 and #27

The original paper stated that every 30 seconds, a small amount of the precursors was added and not continuously added with a syringe pump. Therefore, instead of using syringe pumps,

the PVP and platinic acid stock solutions were added separately every 30 seconds by hand during these syntheses. Each time, 94 µL of PVP and 47 µL of platinic acid stock solution were added. During synthesis #13, 1 mL syringes were used, while Finn pipettes were used for syntheses #26 and #27. The time was too short to "accurately" fill the syringes each time and remove the bubbles; thus, it was not reproducible. With the Finn pipettes, 30 seconds was enough to change the pipette tip and get the needed amount before adding it again to the round bottom flask. The tips melted due to the high temperature, so we had to add the solution quickly every time and then change the tip.

Synthesis #17, #18, and #19

To study the effect of the stirring rate on the resulting nanoparticles, the stirring rate was changed from no stirring to vigorous stirring. During synthesis #17, the reaction was not stirred at all. The solution stabilised at 223 °C and was boiling. Synthesis #18 and #19 were vigorously stirred at 1170 and 950 rpm, respectively. The difference between synthesis #18 and #19 is that a heating mantle with a thermocouple was used instead of the heating plate during synthesis #18. The thermocouple was placed in a glass tube inserted into the round bottom flask. However, because such little solvent is used during the reaction (final volume = 7 mL) in a 50 mL round bottom flask, the glass tube with thermocouple barely touches the solution. However, this still gives a more accurate representation of the actual temperature of the solution, and the heating mantle better distributes the heat. The temperature was set to 200 °C and stabilised at 197 °C. After synthesis #19, a heating mantle with a thermocouple was used instead of the heating plate every time.

Synthesis #25, #28 – #32

To address potential contamination issues, Teflon (PTFE) tubing was used instead of the needles to connect the syringes to the round bottom flask. At first, tubes with an inner diameter of 0.25 mm were used. However, the PVP stock solution was too viscous, and a high flow rate was applied, causing backpressure to disconnect the needle from the syringe. Because of this, not all PVP went into the flask, and what did go in did not go in at the wanted dripping rate. Starting from synthesis #29, tubing with an inner diameter of 0.8 mm was used to resolve this.

During synthesis #31, the drop rate was again decreased, as tried in synthesis #9. This time, the total dripping time was 32 minutes. The rate of the syringe pumps was set as follows:

Rate of PVP stock solution = 5.6 mL/h
Rate of platinic acid stock solution = 2.8 mL/h

During synthesis #32, the 3 mL PVP was already added to the round bottom flask with the 2.5 mL ethylene glycol at the start of the synthesis. Only platinic acid was dripped into the solution with a syringe pump. After synthesis #32, the tubing was no longer used; needles were used instead.

Synthesis #33

To prevent polydispersity, the reaction temperature was set higher in the first half of the reaction than in the second half. The aim was that seeds are created at a high temperature, then at a low temperature, the seeds can grow, and no new seeds would be created. The ethylene glycol was heated at the start of the reaction to 220 °C and stabilised at 193 °C. The syringe pumps were started after 5 minutes of refluxing at this temperature. When 0.80 mL platinic acid and 1.60 mL PVP were dropped into the round bottom flask, the heating mantle was turned off and removed. The rest of the PVP and platinic acid were added while the temperature gradually

cooled down to 80 °C in the end. After that, it was stirred for an additional 5 minutes, during which the temperature cooled further down to 49.9 °C.

Synthesis #34

To prevent aggregation of nanoparticles and, therefore, polydispersity, all PVP was added at the beginning of the reaction. Before the reaction started, the 3 mL PVP stock solution was added to the round bottom flask instead of being dripped into the flask with a syringe pump.

Synthesis #35 – #42

For the last syntheses, the setup (Figure 10) and multiple parameters were changed:

- Glassware was cleaned with aqua regia beforehand to ensure that no residual Pt of past syntheses was left on the glassware, which could act as a seed;
- All volumes were tripled. So, 7.5 mL ethylene glycol was in the flask at the beginning, and 4.5 mL platinic acid, 9 mL PVP, and 1.5 mL $AgNO_3$ stock solution were added during the reaction. This change was done as the thermocouple was not fully inserted into the solution before, and now the temperature would be more accurate;
- The PVP and platinic acid stock solutions were mixed before the reaction. This mixture was then added to the reaction with a Finn pipette instead of a syringe pump. Every 30 seconds, 422 µL was added for 16 minutes in total;
- It was stirred at 530 rpm;
- The reaction was done multiple times at different temperatures, namely 160 °C, 180 °C, and 200 °C.

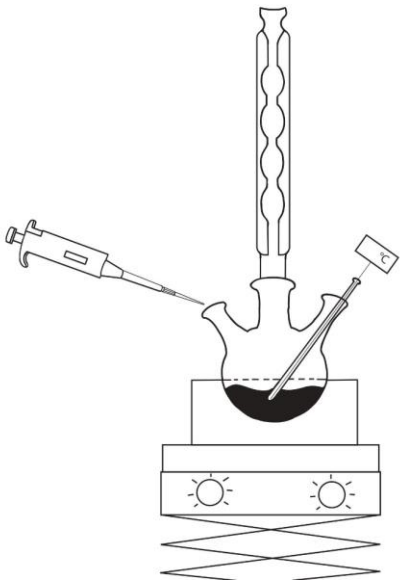

Figure 10 Schematic diagram of the synthesis setup used during syntheses 35 – 42.

3.5. Supporting on silica

After synthesising the Pt nanoparticles, they were supported on silica for eventual use in DRIFTS experiments. To achieve this, 100 mg SiO_2 was submerged in 2 mL ethanol. This was sonicated for 1 hour to ensure homogeneity of the silica. Subsequently, the Pt nanoparticles were added dropwise into the SiO_2/ethanol solution using a pipette while stirred at 300 rpm. The aim was to attain 5 wt.% Pt on SiO_2. The resulting suspension was stirred for an additional 30 minutes, followed by sonication for 3 hours. Finally, the ethanol was removed via drying in the air.

3.6. TEM measurements

3.6.1. TEM preparation

The dissolved Pt nanoparticles in ethanol were first diluted with a 1:1 ratio. 100 µL of the Pt NPs solution was mixed with 100 µL of ethanol. Then, it was dropped onto Formvar/carbon-coated copper grids (300 mesh) using a pipette.

3.6.2. Data processing

The mean size of the Pt NPs was determined using the Fiji software.[67] At least 100 nanoparticles from the TEM images were measured for every sample using Fiji. Subsequently, a histogram was generated to visualise the size distribution.

For facet determination, The HR-TEM images were used. The d-spacing was calculated for approximately 20 nanoparticles per sample. First, a Fourier Transform was taken of a nanoparticle that did not overlap with other nanoparticles. Second, a diffraction point was highlighted. After that, an inverse Fourier Transform was taken of that picture. This generated a black-and-white image of the nanoparticle displaying clear rows of atoms within the nanoparticle. A line was then drawn along one of these rows. A perpendicular line to the first one was drawn using a Macro plugin with the code written hereafter. A Plot Profile is then taken of that perpendicular line, plotting the grey value against the distance. The distance between the band maxima was averaged, giving the d-spacing. The entire process can be seen in Figure 11.

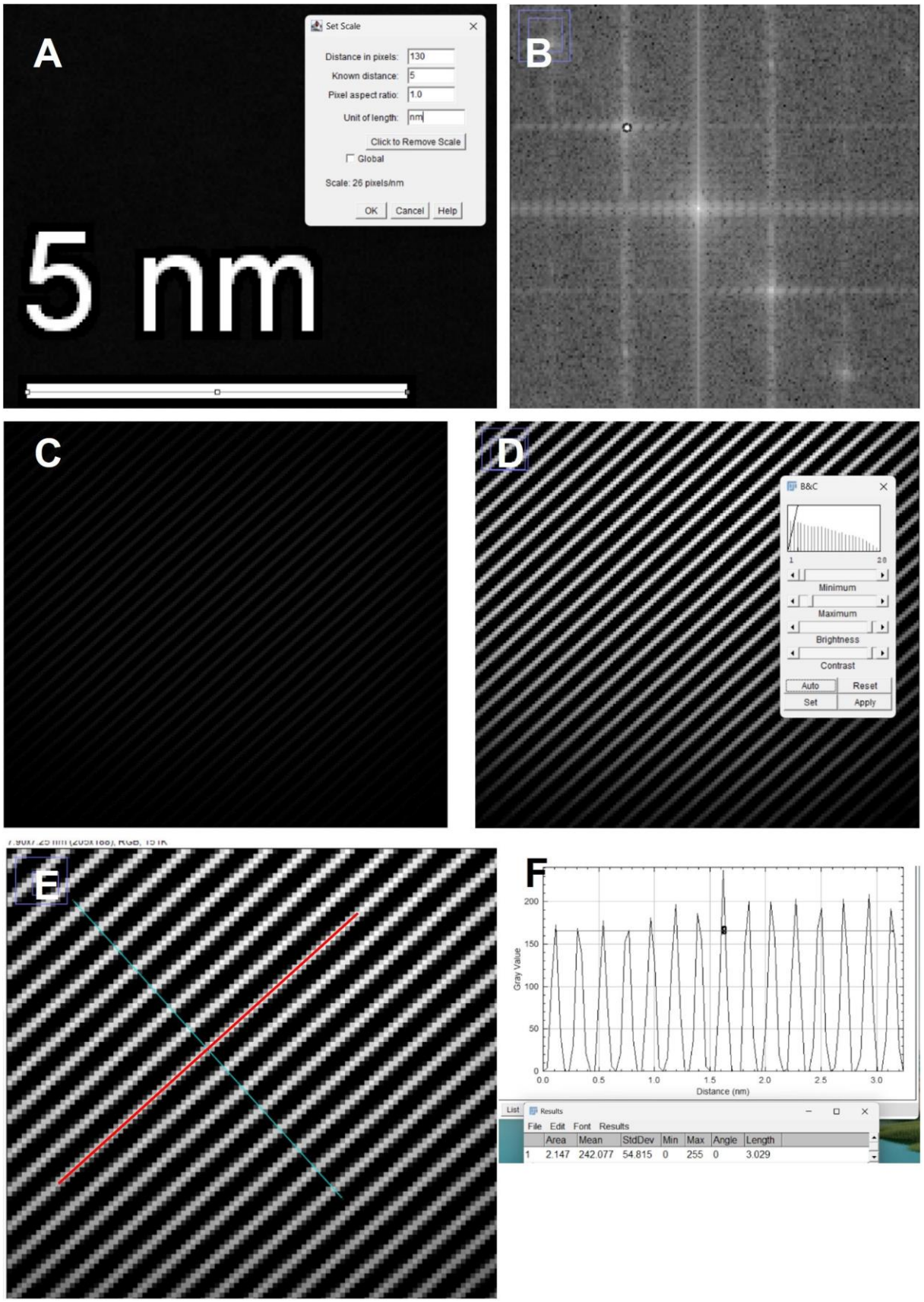

Figure 11 Steps taken to determine the surface facet. ***A:*** *Scale was set.* ***B:*** *A Fourier transform was taken of a single, non-overlapping Pt nanoparticle. A diffraction point is circled and filled in (Ctrl + F).* ***C:*** *An inverse Fourier transform was taken of the Fourier transform.* ***D:*** *The brightness of the inverse Fourier transform is changed to see the atom rows.* ***E:*** *A line (red) is drawn parallel to the atom rows, and with the Macro plugin a perpendicular line (green) is drawn.* ***F:*** *A Plot Profile (Ctrl + K) is taken of the perpendicular line. The d-spacing is determined by averaging the space between the maxima in this plot.*

Code used in Macro plugin:

```
count = roiManager("count");
if (count==0)
        exit("ROI Manager line selection required");
roiManager("select", count-1);
if (selectionType!=5)
        exit("Straight line selection required");
run("Rotate...", "angle=90");
roiManager("Add");
roiManager("Show All without labels");
```

Pt has an fcc crystal structure, which is part of the cubic crystal family. The d-spacing for cubic crystals can be calculated with Equation 14.

$$d_{hkl} = \frac{a}{\sqrt{h^2 + k^2 + l^2}} \qquad (14)$$

For Pt, the unit cell (*a*) has dimensions of approximately 3.912 Å for length, width, and height.[68] The Miller indices (*h, k,* and *l*) indicate where the given plane intercepts the unit cell. Diffraction selection rules for specific crystal structures tell which *hkl* combinations are allowed and which are forbidden. In an fcc crystal structure, like Pt, the Miller indices must all be even or odd. In our study, the low index facets ({100}, {111}, and {110} are relevant. However, {100} is a forbidden reflection, as 0 is an even number, and 1 is odd, violating the all-even/odd rule. Similarly, the {110} facets are forbidden for the same reason.

Thus, the theoretical values of the d-spacing for the {200}, {111}, and {220} facets were calculated, as they are allowed reflections (Table 3). {200} and {220} are higher-order reflections of the 100 and 110 reflections, respectively. Each experimental d-spacing value was then categorised as one of the three facets based on their proximity to these theoretical values, within 1 nm above or below that value.

Facet	Theoretical d-spacing (nm)	Experimental d-spacing (nm)
110	0.138	0.13 – 0.15
100	0.196	0.19 – 0.21
111	0.226	0.22 – 0.24

Table 3 Calculated theoretical d-spacing of different facets in a fcc crystal structure and the experimentally determined d-spacing.

3.7. Monitoring CO adsorption with FTIR spectroscopy

3.7.1. Sample preparation

The Pt supported on SiO_2 was ground using a mortar. It was then sieved to have a final grain size of 75–125 µm. To prepare the DRIFTS cell, quartz wool was first put into the sample holder, after which a small layer of ground Pt/SiO_2 was added. Three different DRIFTS measurements were done on the Pt samples: CO adsorption onto pristine Pt nanoparticles, H_2 and O_2 pretreatments, and CO oxidation.

3.7.2. CO adsorption onto pristine Pt nanoparticles

The Pt/SiO_2 was dried first in the cell by flowing argon through the cell for two hours. Thereafter, the CO flow was alternately turned on and off a total of seven times, increasing the CO to argon ratio each time. The CO adsorption measurements began with 3.33% CO/Ar, incrementally increasing to a final concentration of 33.33% CO/Ar. After each CO adsorption step, the DRIFTS cell was purged with argon. The gas flows and temperatures in each step during the measurement can be seen in Table 4.

Step	Time (min)	T (°C)	Ar (mL/min)	CO (mL/min)
1	120	20	60	0
2	10	20	58	2
3	7	20	60	0
4	10	20	56	4
5	7	20	60	0
6	10	20	54	6
7	7	20	60	0
8	5	20	52	8
9	7	20	60	0
10	5	20	50	10
11	7	20	60	0
12	5	20	45	15
13	7	20	60	0
14	5	20	40	20
15	7	20	60	0

Table 4 DRIFTS program for CO adsorption at room temperature.

3.7.3. H_2-O_2 cycle measurements

To recreate the report of Altantzis et al. (2019)[69] with FTIR spectroscopy, the following FT-IR program was used (Table 5). After pretreatment in H_2 at 300 °C for 1 hour and 15 minutes, the IR cell was cooled down again to room temperature, after which the CO adsorption measurements, as explained in Section 3.7.2, were started. This cycle was then repeated, but instead of an H_2 pretreatment, an O_2 pretreatment was done at 300 °C for 1 hour and 15 minutes. Due to the O_2 and Ar gases sharing a common channel, O_2 was mixed with helium as the inert gas instead.

Step	Time (min)	T (°C)	T ramp (°C/min)	He (mL/min)	CO (mL/min)	H_2 (mL/min)	O_2 (mL/min)	Ar (mL/min)
1	75	300	20	60	0	5	0	0
2	30	20	20	0	0	0	0	60
3	10	20	0	0	2	0	0	58
4	7	20	0	0	0	0	0	60
5	10	20	0	0	4	0	0	56
6	7	20	0	0	0	0	0	60
7	10	20	0	0	6	0	0	54
8	7	20	0	0	0	0	0	60
9	5	20	0	0	8	0	0	52
10	7	20	0	0	0	0	0	60
11	5	20	0	0	10	0	0	50
12	7	20	0	0	0	0	0	60
13	5	20	0	0	15	0	0	45
14	7	20	0	0	0	0	0	60
15	5	20	0	0	20	0	0	40
16	7	20	0	0	0	0	0	60
17	75	300	20	60	0	0	50	0
18	30	20	20	0	0	0	0	60
19	10	20	0	0	2	0	0	58
20	7	20	0	0	0	0	0	60
21	10	20	0	0	4	0	0	56
22	7	20	0	0	0	0	0	60
23	10	20	0	0	6	0	0	54
24	7	20	0	0	0	0	0	60
25	5	20	0	0	8	0	0	52
26	7	20	0	0	0	0	0	60
27	5	20	0	0	10	0	0	50
28	7	20	0	0	0	0	0	60
29	5	20	0	0	15	0	0	45
30	7	20	0	0	0	0	0	60
31	5	20	0	0	20	0	0	40
32	7	20	0	0	0	0	0	60

Table 5 DRIFTS program for CO adsorption at room temperature following H_2 and O_2 pretreatments at 300 °C.

3.7.4. CO oxidation

While ramping from 100 °C to 300 °C, O_2 and CO were flowed through in a 1:4 ratio. After that, it is cooled to room temperature, and the CO adsorption measurements, as explained in Section 3.7.2, are done again. The cycle is then repeated once more. The DRIFTS program can be seen in Table 6.

Step	Time (min)	T (°C)	T ramp (°C/min)	Ar (mL/min)	CO (mL/min)	O_2 (mL/min)
1	15	100	20	60	0	0
2	10	100	0	60	8	0
3	200	300	1	0	8	32
4	10	300	0	60	0	0
5	30	20	50	60	0	0
6	10	20	0	58	2	0
7	7	20	0	60	0	0
8	10	20	0	54	6	0
9	7	20	0	60	0	0
10	5	20	0	50	10	0
11	7	20	0	60	0	0
12	5	20	0	40	20	0
13	7	20	0	60	0	0
14	15	100	20	60	0	0
15	10	100	0	60	8	0
16	200	300	1	0	8	32
17	10	300	0	60	0	0
18	30	20	50	60	0	0
19	10	20	0	58	2	0
20	7	20	0	60	0	0
21	10	20	0	54	6	0
22	7	20	0	60	0	0
23	5	20	0	50	10	0
24	7	20	0	60	0	0
25	5	20	0	40	20	0
26	7	20	0	60	0	0

Table 6 DRIFTS program of two consecutive CO oxidation cycles with CO adsorption at room temperature following each cycle.

3.7.5. Data processing

The single-channel spectra were imported into Matlab. A code was written, with the help of Dr. Bettina Baumgartner, to convert the raw data to an absorbance spectrum and set a certain point in the spectra at zero (baseline correction). The script can be found in Appendix B.

After plotting the raw data, the last spectrum before CO was dosed was chosen as the background spectrum. Using the definition of absorbance, it is calculated using Equation 15.

$$A = \log\left(\frac{I_0}{I}\right) \tag{15}$$

As the Pt-CO band is the area we are interested in, the baseline for each spectrum must be similar in that area. Thus, in each spectrum at the wavelength of 2451.47 cm^{-1}, the intensity is set to 0.

After these steps, the peak fitting is done by fitting Gaussian peaks into the Pt-CO band between 2000–2100 cm^{-1}.[70] Gaussians were found to fit better than Lorentzians for linear adsorbed CO on Pt.[71] The Matlab script is provided in Appendix C. At first, for every peak, the code was used to plot Gaussian peaks up to a maximum of five with the best fit. After this was done for every sample, the resulting peaks were divided into groups with similar wavenumbers. The average wavenumber of each group was calculated, and these averages were then reused to see if the fit for each sample was still adequate. The averages were changed by a few cm^{-1} to see which peak positions fit the best for every sample. When the peak positions were fixed, the peak fitting was repeated to determine the width of each peak. The averages of the peak widths were taken (excluding outliers). With the fixed peak positions and widths, each peak's average area for each sample could be calculated.

The absorbance spectra were first calculated for the CO oxidation experiments as with the CO adsorption spectra. After that, the peak between 2140–2240 cm^{-1} was integrated to see the change in the CO gas phase, and the peak between 2240–2400 cm^{-1} was integrated to see a change in the concentration of the CO_2 in the gas phase. After that, the CO gas bands were subtracted from the spectra before the CO band was plotted. The Matlab script can be found in Appendix D.

4. Results and discussion: Synthesis of platinum nanoparticles

4.1. TEM measurements

4.1.1. Syntheses reproduced from Song et al. (2005)

The synthesis procedure of Pt nanoparticles, as detailed in the study by Song et al. (2005),[23] was replicated six times during our research. In the initial three attempts, the goal was to make cube-shaped Pt NPs. However, as seen in Figure 12A-C, the synthesised cubes exhibited irregularities, particularly spikes forming at their corners. This phenomenon can be attributed to the atom adsorption rate being greater than the surface diffusion rate, as explained in Section 2.3.

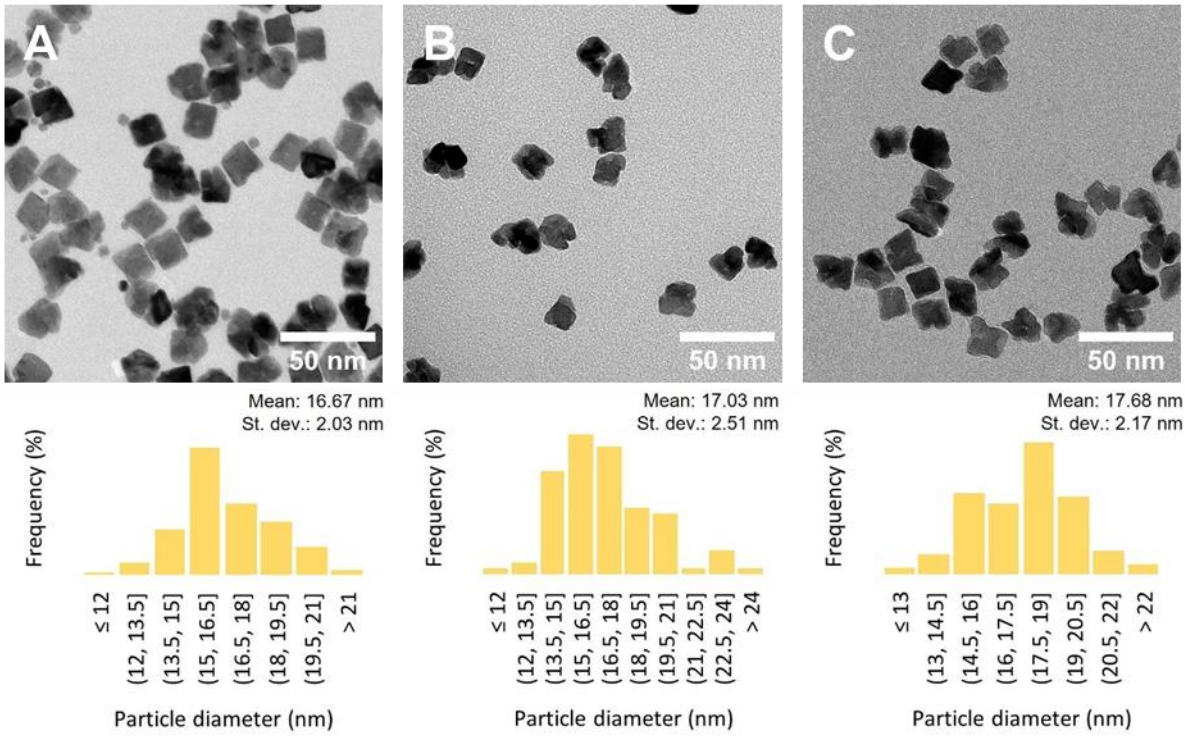

Figure 12 TEM images of different syntheses using 0.002 M $AgNO_3$ aiming for cubic shaped NPs: S1 (A), S2 (B), and S3 (C). 'S' refers to synthesis, each synthesis' conditions can be found in Table 2.

In the fourth and fifth syntheses, 0.06 M $AgNO_3$ was added, aiming for octahedron-shaped Pt NPs. The TEM images (Figure 13A-B) showed that stars and tetrahedrons were formed mainly. Although the desired octahedrons were not formed, tetrahedrons also have only {111} facets. This indicates that the more $AgNO_3$ is added, the more {111} facets are formed. An additional observation was that the particles aggregated more, forming circular aggregates. In the sixth synthesis, 0.02 M $AgNO_3$ was added to form cuboctahedral-shaped NPs. Octahedrons were mainly formed (Figure 13C).

From these initial syntheses, we could see that adding more silver nitrate to the synthesis caused the shape to change from cubes to octahedrons to tetrahedrons and stars. However, the addition of more silver nitrate appeared to be the cause of the nanoparticles' tendency to aggregate. Besides the shape, the size of these NPs was all relatively large, around 17 nm for cubes and 35 nm for octahedrons and cuboctahedrons.

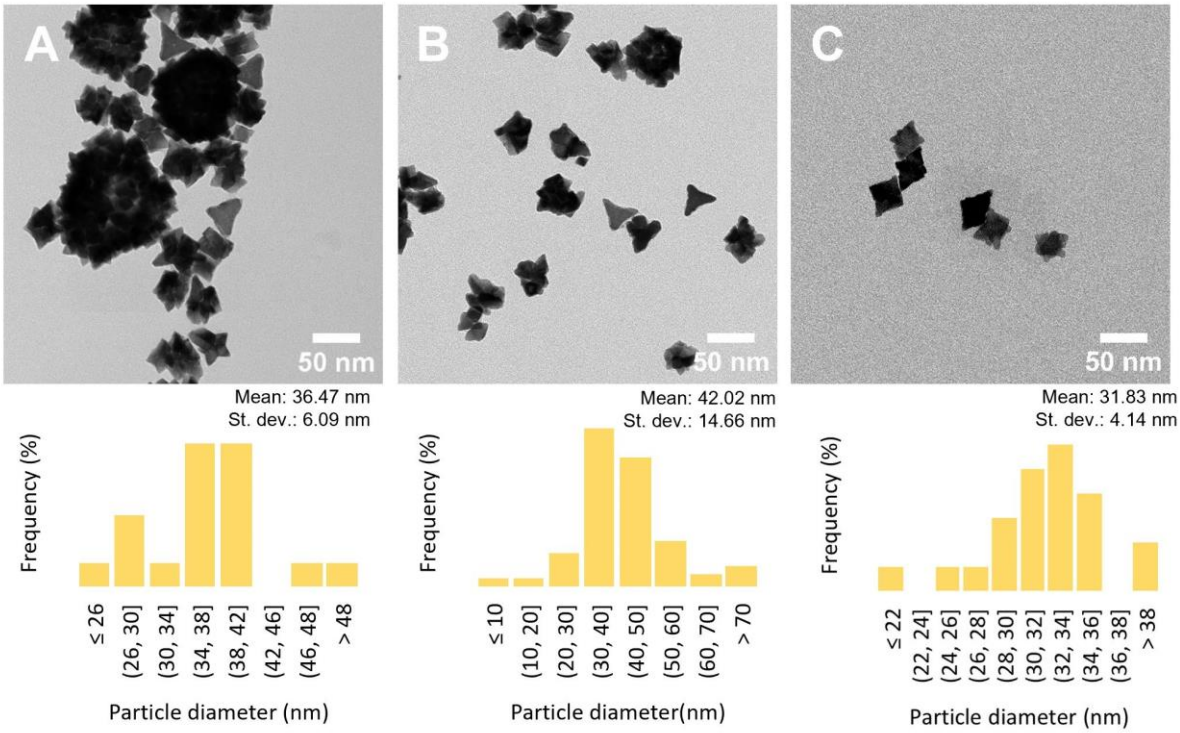

Figure 13 TEM images of different syntheses using either 0.06 M $AgNO_3$ with octahedrons as goal – S4 (A) and S5 (B) – or 0.02 M $AgNO_3$ with cuboctahedrons as goal – S6 (C). 'S' refers to synthesis, each synthesis' conditions can be found in Table 2.

Effect of an increased surface diffusion rate or decreased adsorption rate

The biggest issue was the formation of spikes at the corners. A solution could be reducing the atom adsorption rate or increasing the surface diffusion rate. We tried to do this by lowering the syringe pumps' dripping rate (S9) or increasing the reaction temperature (S8), respectively. The syringe pumps' slower drop rate resulted in either relatively small nanoparticles or large aggregates (Figure 14A). On the contrary, using a reaction temperature of 200 °C, NPs with cube-like shapes with rounded corners were formed (Figure 14B). Furthermore, the average nanoparticle size became much smaller, approximately 5 nm. Because the temperature increase seemed essential to getting cube-shaped particles, this temperature was used from S8 onwards.

Various modifications were introduced, such as mixing the PVP and platinic acid before the reaction and adding them with one syringe pump (S7). This gave very polydisperse NPs with ill-defined shapes (Figure 14C). To determine the effect of silver nitrate, during S10, the silver nitrate was not added, producing a few cubes with rounded corners but less well-defined shapes than S8. Additionally, the sample was polydisperse in size (Figure 14D). S8 was reproduced to determine if it was not luck (S16). The results seemed to agree with each other. Cube-shaped particles were formed. However, many still had no definite shape (Figure 14H). The average NP size of S16 is unknown, as the TEM images were exported without a scale bar.

Effect of a N_2 environment

According to Herricks et al. (2004)[19], air influences the reaction kinetics. They found that the reaction goes quicker when under an argon or nitrogen environment, resulting in more cubes. Whereas, when performed in air, the reaction goes slower, resulting in more anisotropic shapes like tetrahedrons and octahedrons. However, in our case (S11 and S12), an N_2 environment produced undefinable shapes and polydisperse samples (Figure 14E-F).

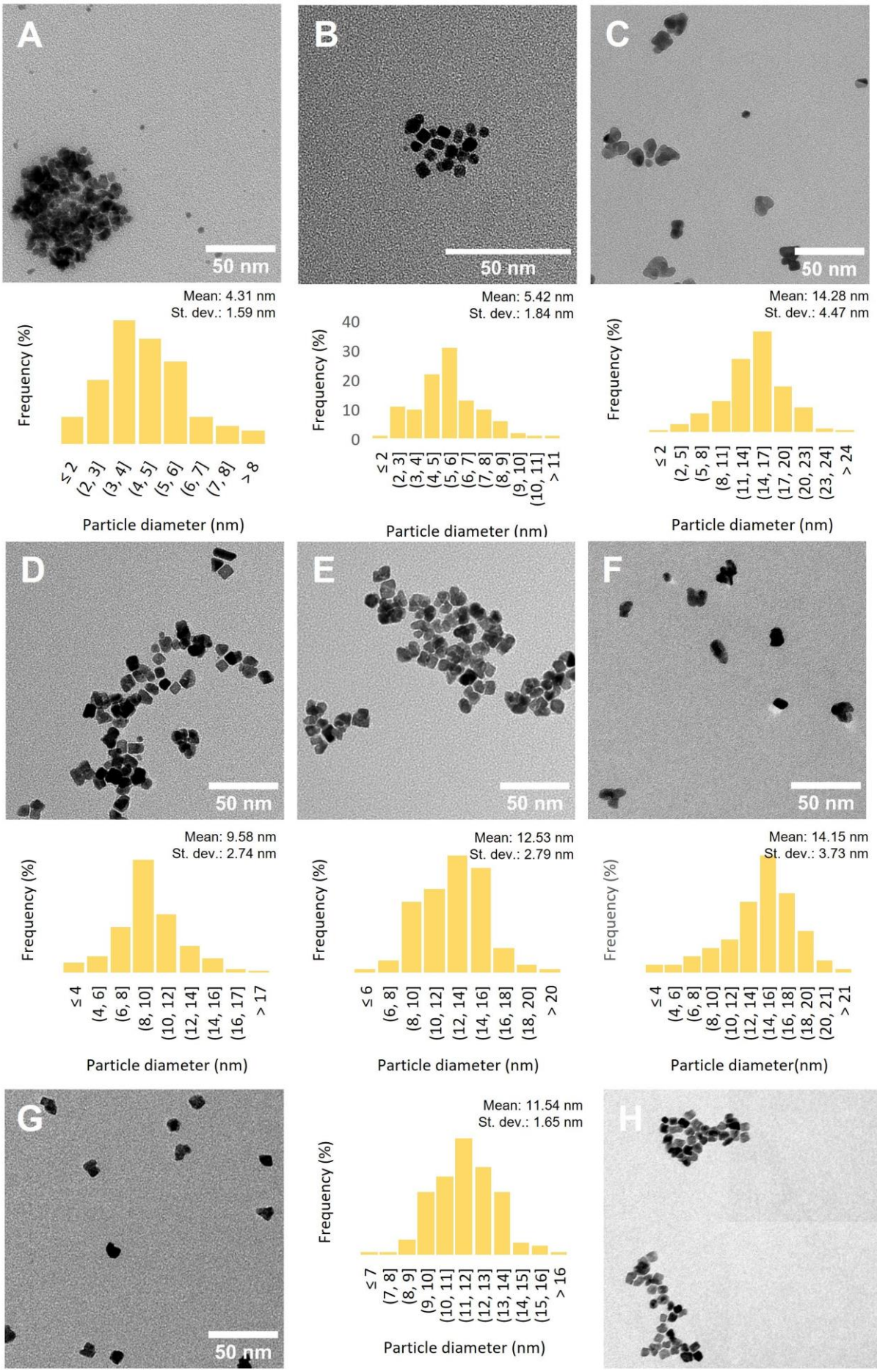
A
50 nm
B
50 nm
C
50 nm
Mean: 4.31 nm
St. dev.: 1.59 nm
Frequency (%)
≤ 2
(2, 3]
(3, 4]
(4, 5]
(5, 6]
(6, 7]
(7, 8]
> 8
Particle diameter (nm)
Mean: 5.42 nm
St. dev.: 1.84 nm
Frequency (%)
40
30
20
10
0
≤ 2
(2, 3]
(3, 4]
(4, 5]
(5, 6]
(6, 7]
(7, 8]
(8, 9]
(9, 10]
(10, 11]
> 11
Particle diameter (nm)
Mean: 14.28 nm
St. dev.: 4.47 nm
Frequency (%)
≤ 2
(2, 5]
(5, 8]
(8, 11]
(11, 14]
(14, 17]
(17, 20]
(20, 23]
(23, 24]
> 24
Particle diameter (nm)
D
50 nm
E
50 nm
F
50 nm
Mean: 9.58 nm
St. dev.: 2.74 nm
Frequency (%)
≤ 4
(4, 6]
(6, 8]
(8, 10]
(10, 12]
(12, 14]
(14, 16]
(16, 17]
> 17
Particle diameter (nm)
Mean: 12.53 nm
St. dev.: 2.79 nm
Frequency (%)
≤ 6
(6, 8]
(8, 10]
(10, 12]
(12, 14]
(14, 16]
(16, 18]
(18, 20]
> 20
Particle diameter (nm)
Mean: 14.15 nm
St. dev.: 3.73 nm
Frequency (%)
≤ 4
(4, 6]
(6, 8]
(8, 10]
(10, 12]
(12, 14]
(14, 16]
(16, 18]
(18, 20]
(20, 21]
> 21
Particle diameter(nm)
G
50 nm
Mean: 11.54 nm
St. dev.: 1.65 nm
Frequency (%)
≤ 7
(7, 8]
(8, 9]
(9, 10]
(10, 11]
(11, 12]
(12, 13]
(13, 14]
(14, 15]
(15, 16]
> 16
Particle diameter (nm)
H

Figure 14 TEM images of different syntheses aiming for cubes: S9 with a slower dripping rate (A), S8 at 200 °C (B), S7 with one syringe pump (C), S10 without $AgNO_3$ (D), S11 in a N_2 atmosphere (E), S12 in a N_2 atmosphere (F), S13 with no syringe pumps (G), and S16 (H). 'S' refers to synthesis, each synthesis' conditions can be found in Table 2.

Syringe pump effect

In one synthesis (S13), the syringe pumps were not used, and instead, the PVP and platinic acid stock solutions were added by hand with syringes every 30 seconds. This decision was made as the original paper[23] stated that every 30 seconds, a small amount was injected into the solution and not continually dripped in. It resulted in a well-dispersed sample, but the NPs had no identifiable shape (Figure 14G).

Stirring rate effect

The stirring rate during the reaction was the next parameter that was varied to investigate its impact on the final NP shape. Different stirring conditions were employed: no stirring (S17), high stirring rates of 1170, 950, and 1150 rpm (S18, S19, and S23), and a medium stirring rate of 450 rpm (S20). Additionally, the heat source was changed to a heating mantle in S18. This gave excellent results, with well-defined cubes of approximately 8 nm (Figure 15A).

When comparing no stirring (S17) to vigorous stirring (S19), both utilizing a heating plate as the heat source (Figure 15B and Figure 16A), the NPs' shapes were cubic when the solution was not stirred and formed large aggregates when vigorously stirred. S17 was polydisperse, and S19's average NP size could not be measured as there were not enough single particles.

Temperature again proved to be important to the final NP shape. Given these observations, a heating mantle was also used to make octahedrons in S20 (450 rpm) and S23 (1150 rpm), as seen in Figure 16B and Figure 15C. However, these attempts yielded unsatisfactory results with indistinct shapes for both samples and low yields for S20.

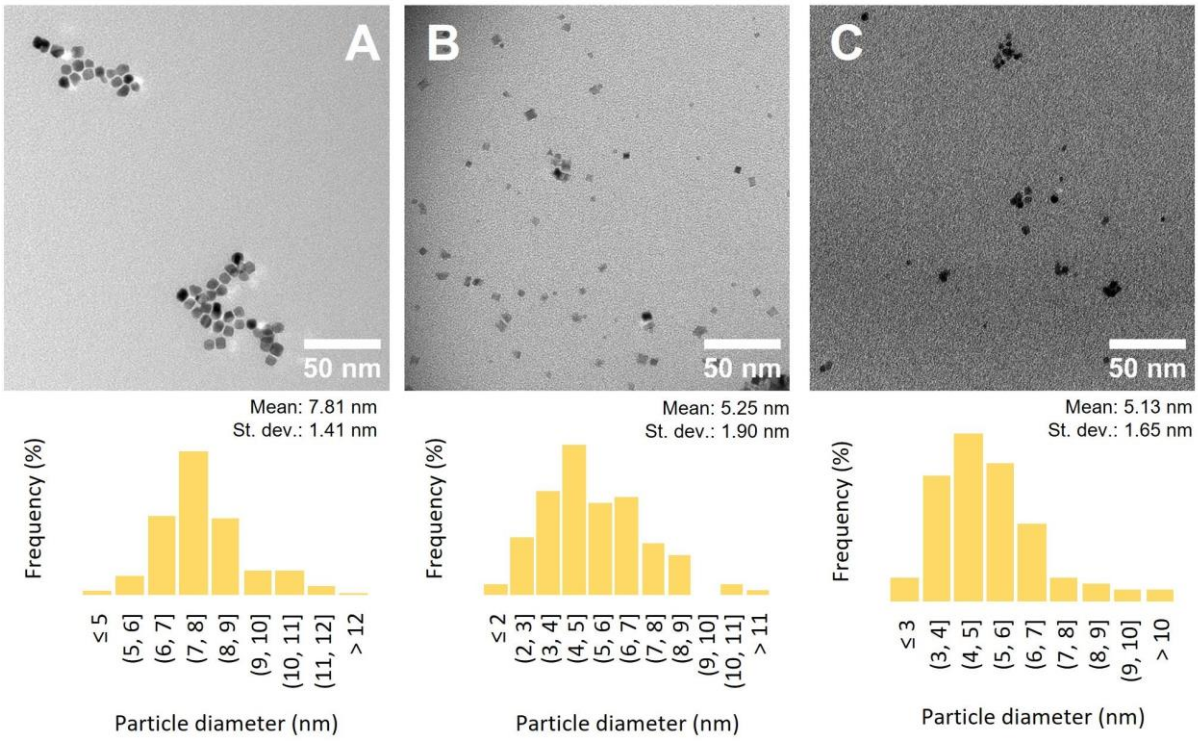

Figure 15 TEM images of different syntheses: S18 cubes with strong stirring (A), S17 with no stirring (B), S23 octahedrons with strong stirring (C). 'S' refers to synthesis, each synthesis' conditions can be found in Table 2.

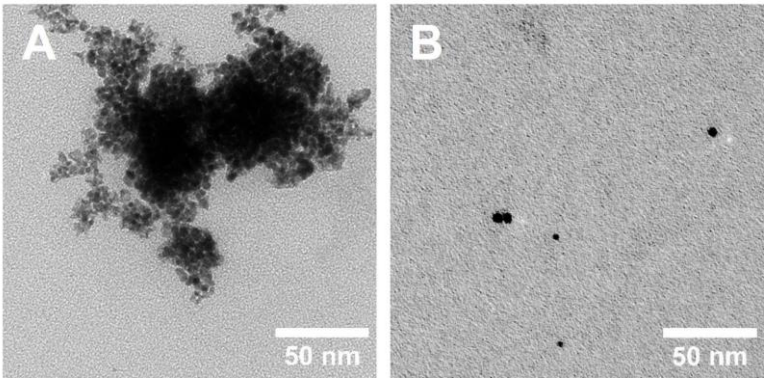

Figure 16 TEM images of different syntheses: S19 cubes with strong stirring (A) and S20 (B). 'S' refers to synthesis, each synthesis' conditions can be found in Table 2.

Syringe pump effect

As the original paper clearly stated that they added the stock solutions every 30 seconds, and our first attempt with the syringes was not reproducible and had poor results, we still wanted to find a way to reproduce this. S26 and S27 were the syntheses where it was tried again; however, Finn pipettes were used instead of syringes this time, making it more accurate. Both cubes (S26) and octahedrons (S27) were synthesised, as shown in Figure 17A and B. The desired cubes yielded less-than-ideal results for the first attempt. In S27, aiming for octahedrons, the process was more organised, resulting in well-dispersed NPs of approximately 13 nm with some octahedrons. Nevertheless, overall, most NPs were not clear octahedrons.

Effect of using tubing instead of needles

The syringes' metal needles were replaced with Teflon tubing in S25, S28–S32 to address potential contamination issues. Initially, Teflon tubing with an inner diameter of 0.25 mm was used. However, this led to backpressure, especially in the syringe filled with the PVP stock solution. Therefore, with both S25 and S28, not all the PVP was added to the reaction flask. As seen in Figure 17C, D, the results show no well-defined particles and polydisperse samples. When Teflon tubing with an inner diameter of 0.8 mm was used, the backpressure issues were solved. With S29 and S30, we aimed for cubes and octahedrons, respectively (Figure 17E, F). However, both yielded ill-defined NPs and again, the samples were polydisperse.

In the subsequent two syntheses, two parameters were varied. First, the dripping rate was slowed down (S31). We can see in Figure 18A that the resulting NPs were relatively large and had no particular shape. Second, the PVP stock solution was added to the reaction flask before the reaction began instead of dripping it into the flask during the reaction (S32). This leads to cubic-shaped NPs (Figure 18B). A downside of both samples was that they were polydisperse, as were all other samples, since we began using tubing instead of needles. The decision was made to switch back to using needles, as it seemed to cause polydispersity.

As S32 showed promising results, this synthesis was repeated using needles instead of tubing (S34). However, the transition back to needles did not lead to a less polydisperse sample; there were mainly large aggregate formations, and the well-defined cubic shape observed in S32 was not reproduced (Figure 18C).

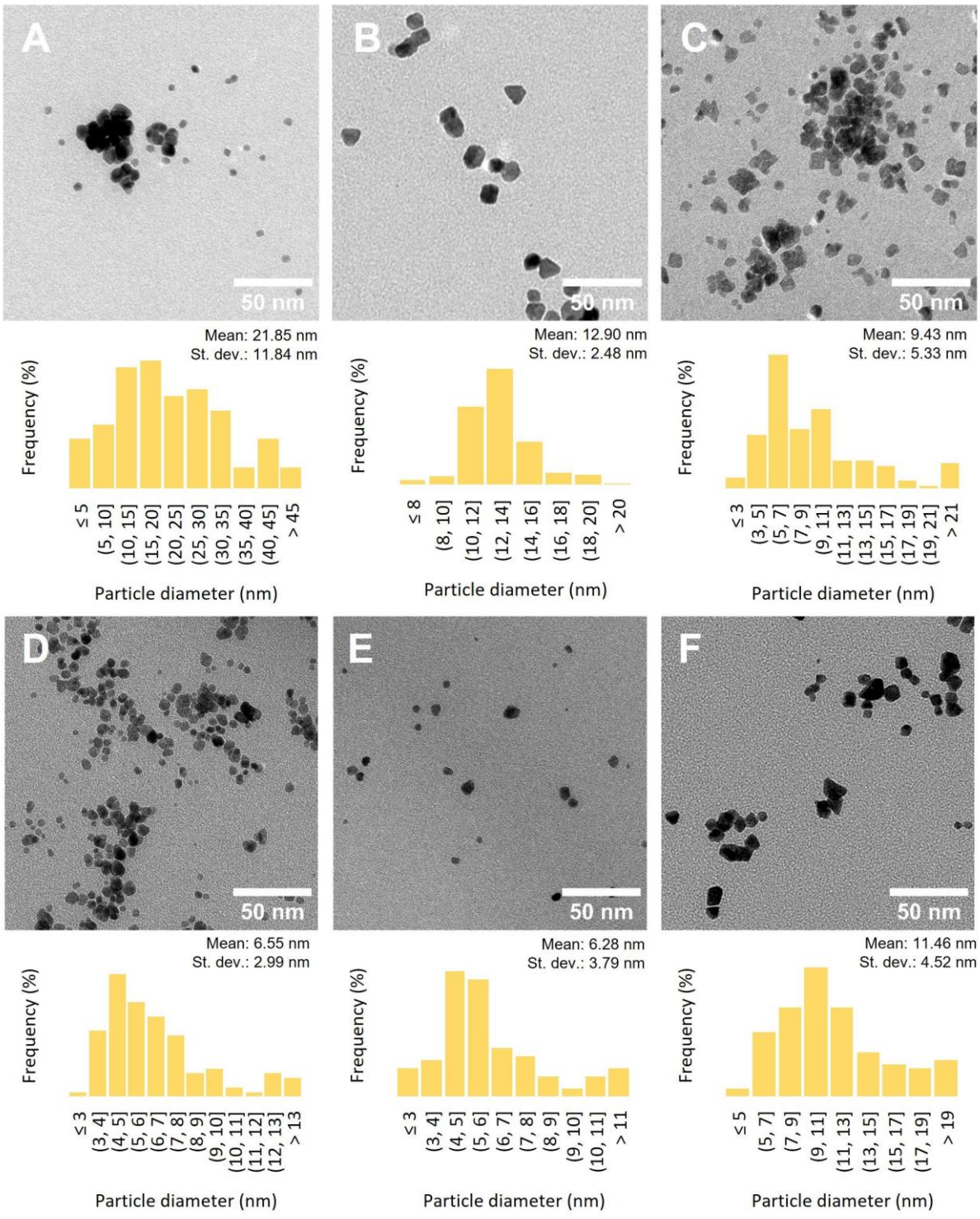

Figure 17 TEM images of different syntheses:, S26 (A) with Finn pipettes, S27 with Finn pipettes (B), S25 (C) with tubing (0.25 mm), S28 with tubing (0.25 mm) (D), S29 with tubing (0.8 mm) (E), and S30 with tubing (0.8 mm) (F). 'S' refers to synthesis, each synthesis' conditions can be found in Table 2.

Effect of a two-step temperature method

As polydispersity was a common issue, we tried to influence the reduction kinetics by first creating numerous Pt seeds at high temperatures and then at low temperatures, allowing the already formed seeds to grow uniformly (S33). Contrary to expectations, this approach did not remove the polydispersity, as seen in Figure 18D, and the particles remained poorly defined.

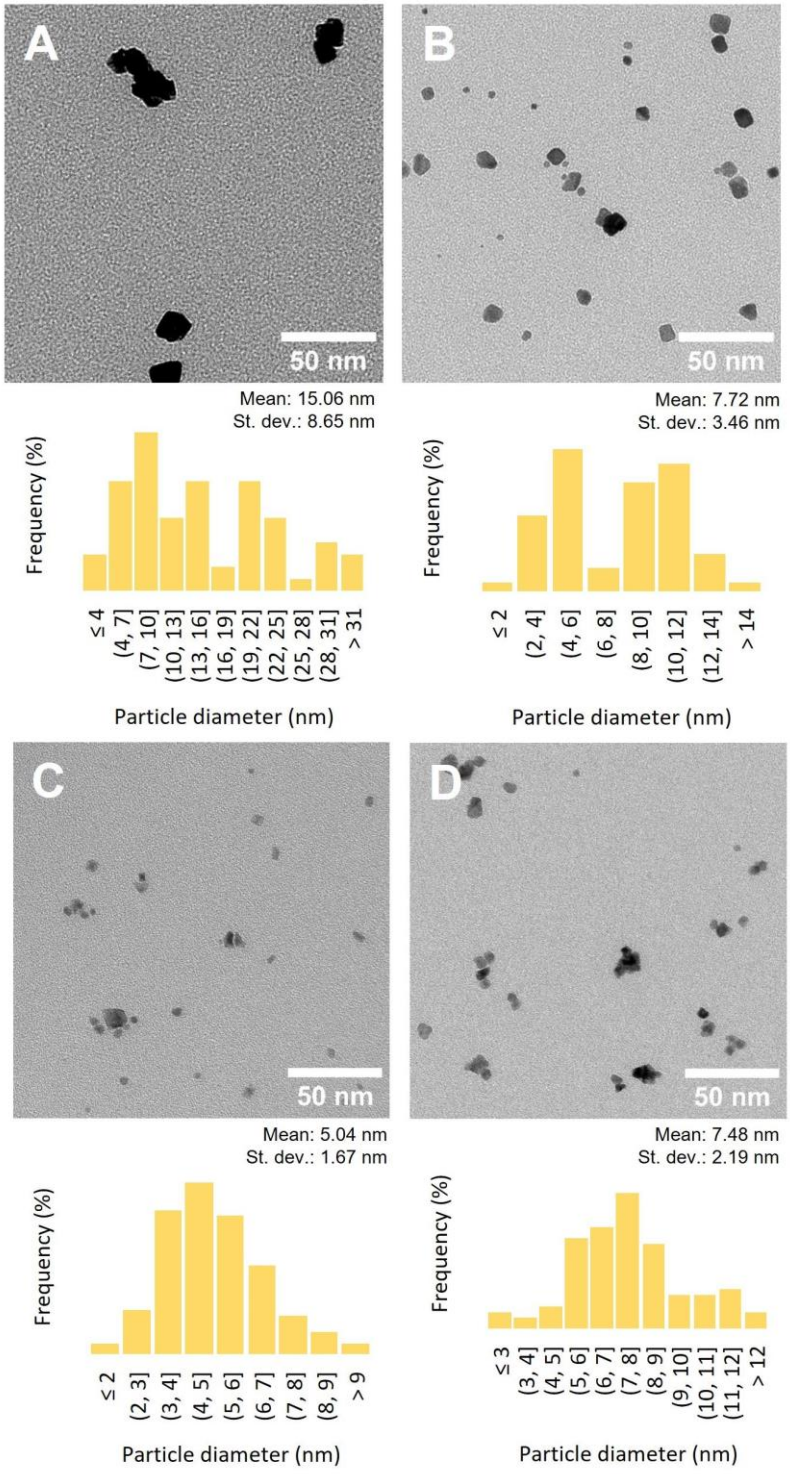

Figure 18 TEM images of different syntheses: S31 with slower dripping rate and tubing (0,8 mm) (A), S32 with PVP already in the flask and tubing (0.8 mm) (B), S34 with PVP already in the flask (C), and S33 with different temperature at the start and end of the reaction (D). 'S' refers to synthesis, each synthesis' conditions can be found in Table 2.

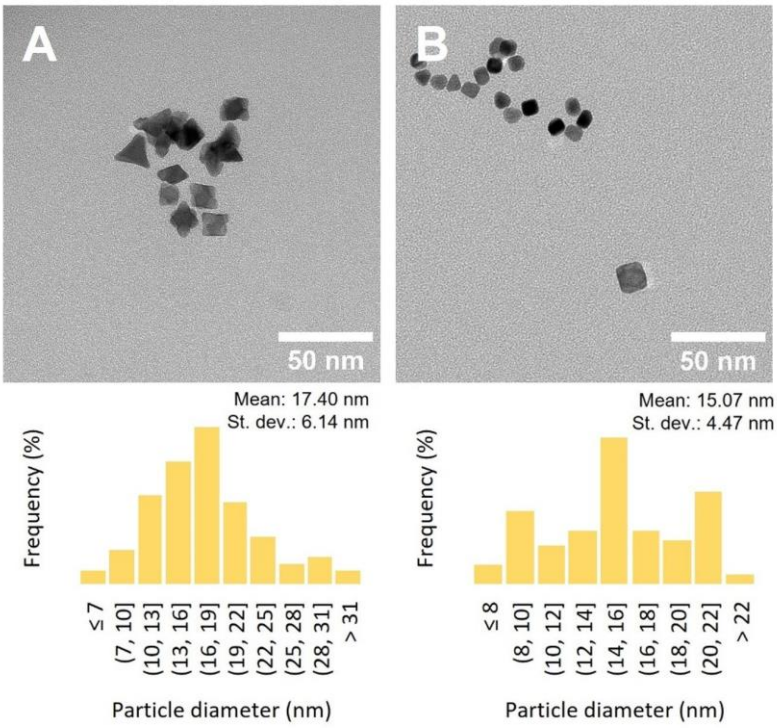

Figure 19 TEM images of different syntheses: S36 octahedrons at 160 °C (A) and S41 octahedrons at 180 °C (B). 'S' refers to synthesis, each synthesis' conditions can be found in Table 2.

Temperature effect

In the final set of experiments, cubes and octahedrons were synthesised at different temperatures (160, 180, and 200 °C) in S35, S40, S42 (cubes), S37, S39, and S38 (octahedrons). The syringe pumps were replaced, and a mixed PVP and platinic acid solution was added with Finn pipettes every 30 seconds. The octahedrons synthesised at 160 °C gave poorly defined octahedrons (S36), as seen in Figure 19A, and therefore repeated in S37. We also did a second try at the octahedrons synthesised at 180 °C (S39), which were aggregated and therefore also repeated (S41), which yielded a worse result (Figure 19B).

The TEM images of the cubes and octahedrons are shown in Figure 20A–C and D–F, respectively. This synthesis method yielded excellent results for both cubes and octahedrons. For the cubes, the TEM images show no significant differences between the three temperatures. The shape is well-defined, and the samples are monodisperse, increasing polydispersity with increasing temperature. However, for the octahedrons, the well-defined shape observed at 160 °C worsened with increasing temperature. At 200 °C, it had completely lost its octahedral shape. Polydispersity remained an issue for the octahedron samples, with the highest polydispersity observed in the sample synthesised at 180 °C.

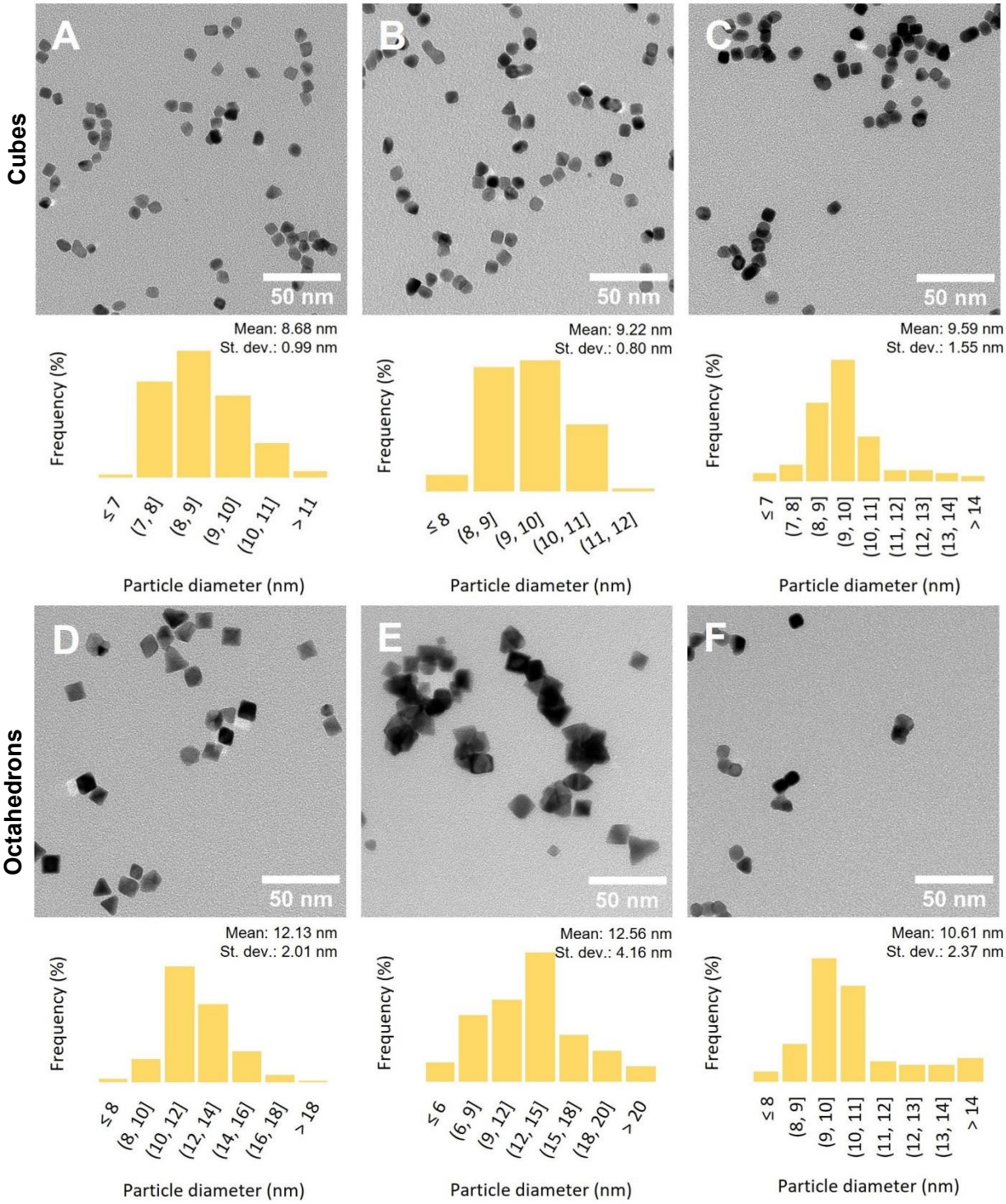

Figure 20 TEM images for different syntheses varying the $AgNO_3$ molarity and temperature: S35 (A), S40 (B), S42 (C), S37 (D), S39 (E), and S38 (F). 'S' refers to synthesis, each synthesis' conditions can be found in Table 2.

4.1.2. Syntheses reproduced from Hu et al. (2006)

The synthesis, as written in Hu et al. (2006)[65], was reproduced twice. The first attempt resulted in very little product, insufficient for further characterization with TEM and/or FTIR spectroscopy. In the second attempt, as shown in Figure 21, at low magnification, it appears that Pt nanosheets have formed. The nanosheets are also frequently shaped like an octahedron. When a higher magnification was used, large aggregates of approximately 30 nm can be seen next to the sheets. Alongside the aggregates are numerous small Pt nanoparticles. This synthesis resulted in a polydisperse result and did not have the desired shape.

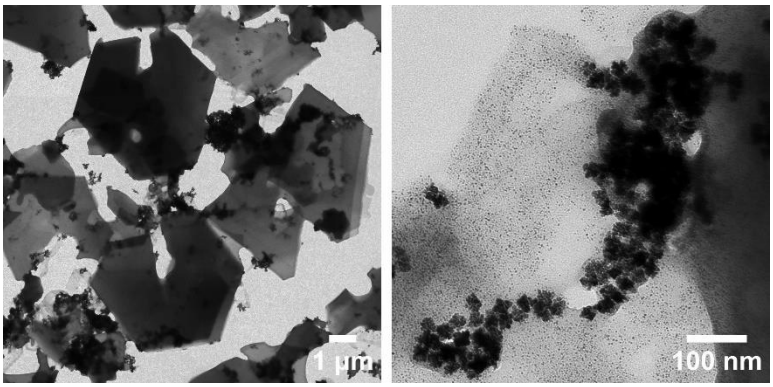

Figure 21 TEM images of S15. 'S' refers to synthesis, each synthesis' conditions can be found in Table 2.

4.1.3. Syntheses reproduced from Lee et al. (2006)

The synthesis described by Lee et al. (2006)[66] was attempted thrice. The first attempt had a low yield and was insufficient for TEM characterization and/or FTIR spectroscopy. The second and third attempts of this synthesis can be seen in Figure 22, which revealed a significant issue of this synthesis. CTAB is used as a ligand, but the washing process applied could not entirely remove them. Additionally, the formed NPs were very small and had no distinguishable shape.

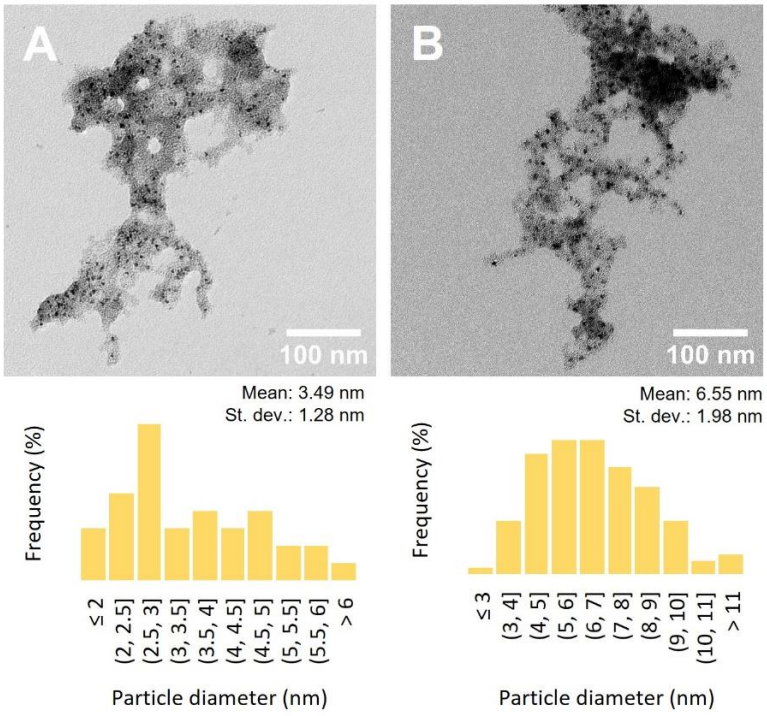

Figure 22 TEM images of different syntheses: S22 (A) and S24 (B). 'S' refers to synthesis, each synthesis' conditions can be found in Table 2.

4.2. Stock solution storage

For the experiments, 25 mL stock solutions of both PVP and platinic acid in ethylene glycol were prepared and stored in the refrigerator, wrapped in aluminium foil. Given that ethylene glycol also acts as the reducing agent in the reaction, it could reduce the platinic acid catalysed by light and/or temperature. UV-Vis spectroscopy was used to analyse the stock solution sample after 7 and 26 days of refrigeration to ensure that the platinic acid was not reduced while it was stored. A reference sample of platinic acid in ethylene glycol was taken that was stored for 12 days in a fume hood without the protective layer of aluminium foil. The three UV-Vis spectra can be seen in Figure 23.

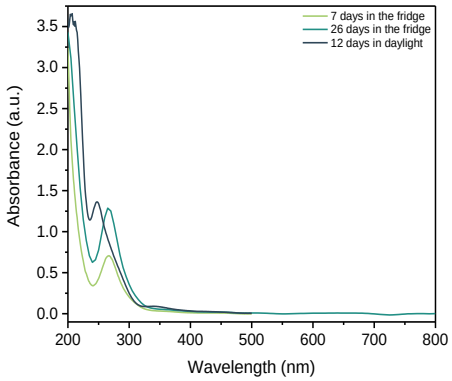

Figure 23 UV-Vis spectra of platinic acid in ethylene glycol: (Green) Sample stored for 7 days in the refrigerator with aluminium foil; (Blue) Sample stored for 26 days in the refrigerator with aluminium foil; (Dark blue) Reference sample stored for 12 days in a fume hood without aluminium foil.

As shown in Figure 23, both samples kept in the fridge have a peak around 266 nm, and the sample kept in the fume hood has a peak at 248 nm. $PtCl_6^{2-}$ has a distinctive peak at 268 nm, while $PtCl_4^{2-}$ has a distinctive peak at 228 nm. It was reported that when reduced with ethylene glycol, the peak at 268 nm quickly disappears while moving to a lower wavelength.[19] Thus, the sample left in the fume hood is slowly being reduced to Pt(II) and eventually Pt(0). However, the peak of the sample in the fridge has not changed after 26 days. In conclusion, platinic acid dissolved in ethylene glycol is not reduced when stored in the fridge wrapped in aluminium foil; thus, using month-old stock solutions will not influence the reaction rate.

4.3. Characterisation of residual ligands

PVP is used as a ligand to stabilise the Pt NPs. However, when doing CO adsorption, the concern is that the PVP will block the CO from accessing the NP surface. This would cause low CO adsorption, and then no analysis of the Pt-CO band can be done. We wash away some PVP after the synthesis, but not all of it. The characteristic bands of PVP can be seen in the DRIFTS spectra; an example is shown in Figure 24. Zoomed-in spectra of areas 1 and 2 show bands due to the following vibrations: ν(C-H) (2900–3000 cm^{-1}), ν(C=O) (~1700 cm^{-1}), ν(C=C) (~1650 cm^{-1}), ν(C-N) in O=C-N (~1500 cm^{-1}), $\delta(CH_2)$ bending (multiple bands from 1400-1470 cm^{-1}), and ν(C-N) (1270–1300 cm^{-1}).[54,72–75]

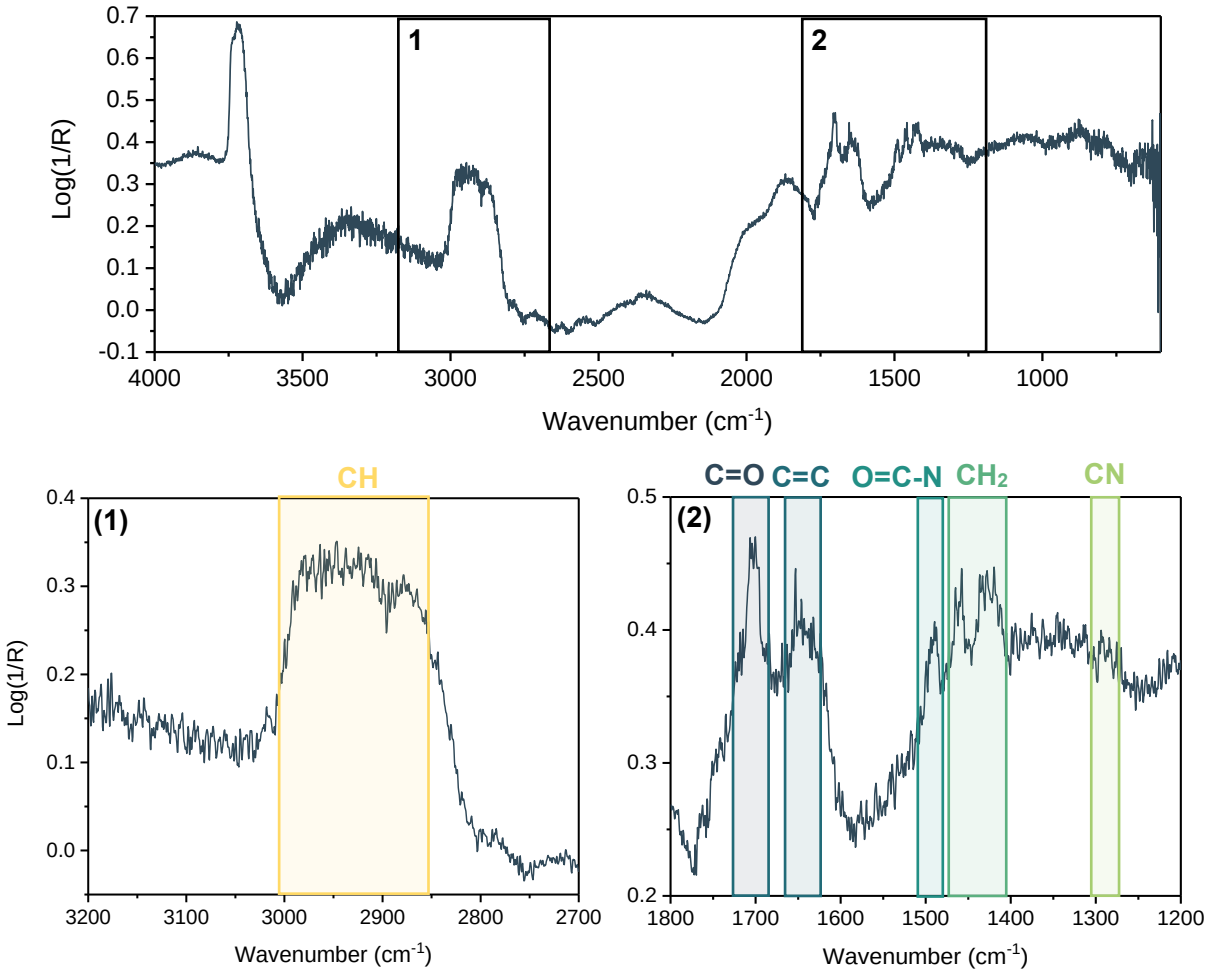

Figure 24 Above: Full DRIFTS spectrum of S18 on SiO_2 at room temperature. Below: Zoomed in areas of the full DRIFTS spectrum showing characteristic bands of PVP. 'S' refers to synthesis, each synthesis' conditions can be found in Table 2.

TGA was done on one sample to determine how much PVP was on the surface of the Pt NPs (Figure 25). After 220 °C, there was a 73% weight loss till 430 °C, mainly caused by burning off the PVP. This is a sizeable amount; however, after doing CO-IR spectroscopy with the samples and often getting significant absorbance, it was decided not to remove the PVP from the samples. Nevertheless, how the PVP influences the CO-IR spectroscopy results could be interesting to research.

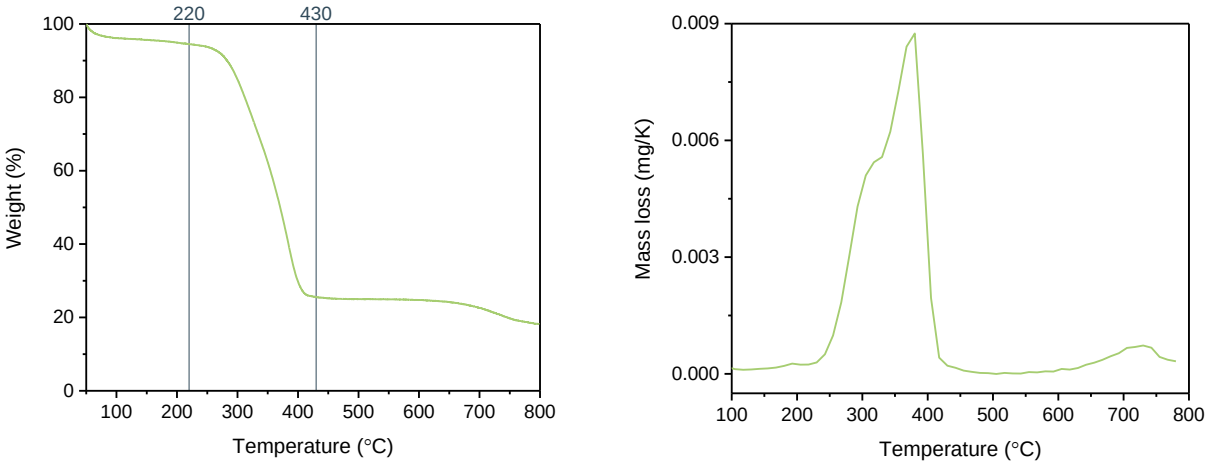

Figure 25 TGA spectra of S20. Left: Spectra showing how much of the initial weight is lost at each temperature. Right: Mass loss in mg K^{-1} for each temperature. 'S' refers to synthesis, each synthesis' conditions can be found in Table 2.

5. Results and discussion: CO-IR spectroscopy

5.1. CO adsorption on Pt nanoparticles monitored by FTIR spectroscopy

DRIFTS spectra following CO adsorption on S18 are shown in Figure 26. The spectrum shows four distinct bands: a CO_2 gas band at 2300–2400 cm^{-1}, an oxidized Pt-CO at 2170 cm^{-1} (likely due to Pt^{3+}) [31–33], a metallic Pt-CO band at 2080 cm^{-1}, and a smaller band at 1850 cm^{-1} attributed to CO adsorbing in a bridged configuration.[34]

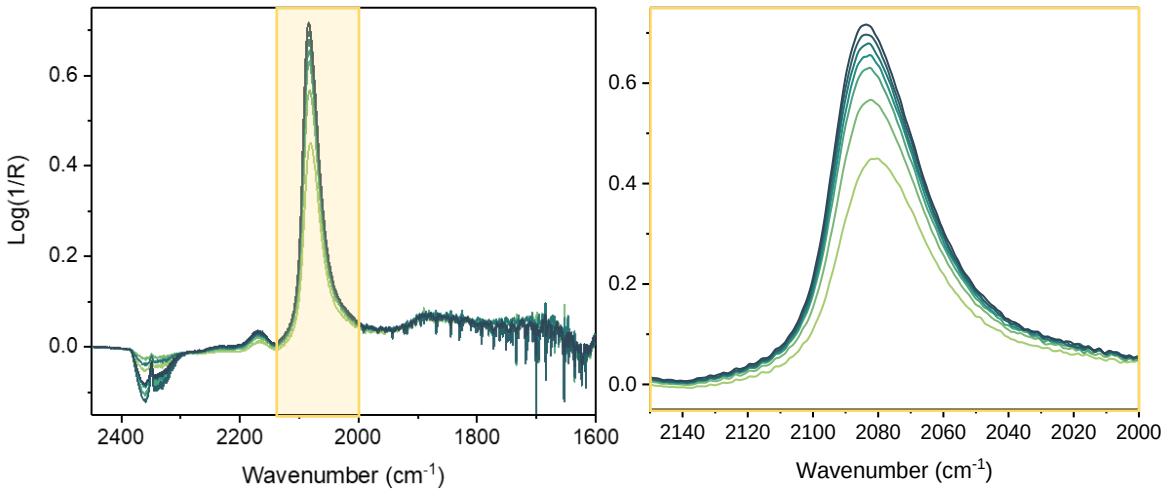

Figure 26 DRIFTS spectrum of S18 on SiO_2 after CO adsorption at room temperature. From light green to dark blue the CO concentration of the gas stream increases from 3% to 33%. 'S' refers to synthesis, each synthesis' conditions can be found in Table 2.

Zooming in on the Pt(0)-CO band shows a blueshift with increasing CO adsorption. This shift is due to CO-CO dipole coupling. As the CO coverage of the Pt NP increases, more CO dipoles are next to each other. When the CO molecules are vibrating in phase with each other, it has a higher frequency than CO molecules vibrating out of phase or alone.[38] In Figure 27, the CO band position is plotted against the CO concentration in the applied gas stream. A sudden increase in band position is observed from 3% to 6% CO concentration, followed by a slower increase. Beyond 24% CO concentration, the band position stabilises, suggesting CO saturation is achieved during the CO adsorption measurement. This observation ensures that the CO adsorption experiments are comparable, as CO coverage is equal for all samples.

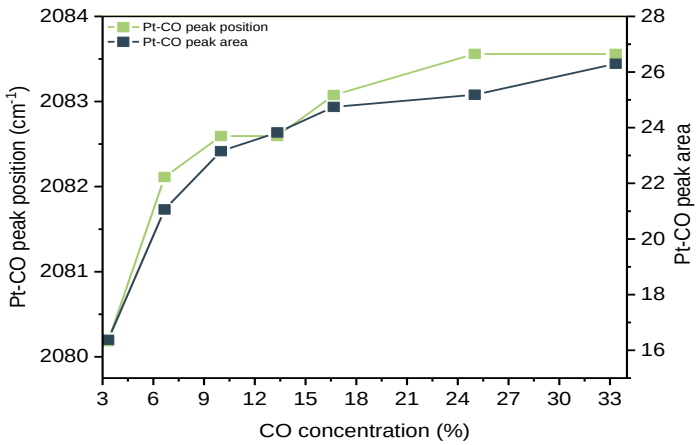

Figure 27 Pt-CO peak position versus the applied CO concentration on S18 at room temperature. 'S' refers to synthesis, each synthesis' conditions can be found in Table 2.

5.2. Facet-dependent CO adsorption: Cubes versus octahedrons

Ten different cubes and four different octahedrons, all synthesized at 200 °C, were characterized with CO-IR spectroscopy. The Pt-CO band positions of the predominant bands, excluding shoulders, are plotted in Figure 28. Most cubes showed a Pt-CO band ranging from 2070 to 2080 cm^{-1}, with the initial cubes synthesized in this study showing a band around 2060 cm^{-1}. This variation could be attributed to the spikes on the corners (S1 and S3), creating more under-coordinated adsorption sites and consequently lowering the Pt-CO band frequency. The results suggested the synthesized octahedrons were similar to the cubes as the Pt-CO band showed at similar wavenumbers. However, only four octahedral-shaped samples were tested with CO adsorption. Thus, the limited number of samples limits us from reaching a definite conclusion. Nonetheless, one curious observation of the octahedrons was an outlier (S27) at 2019 cm^{-1}. This outlier will be discussed in Section 5.3.

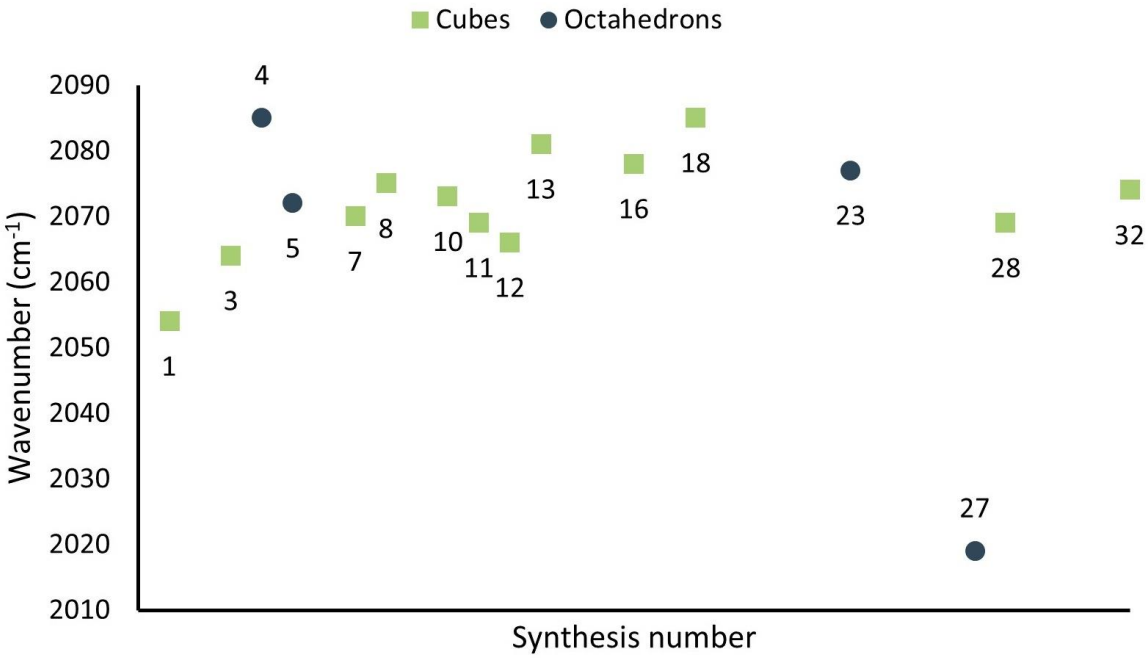

Figure 28 Wavenumber of the highest peak position of the Pt-CO peak for various syntheses synthesized at 200 °C. Each synthesis' conditions can be found in Table 2.

Upon altering the synthesis from a reaction temperature of 200 °C to 160 °C, a shift in the CO-IR spectroscopy results can be observed, as seen in Figure 29. The Pt-CO band shifted from 2070–2080 cm^{-1} to 2050–2060 cm^{-1}. According to Brandt et al. (1992), a change of 10 cm^{-1} corresponds to a change in coordination number by one.[76] This suggests an absence of {111} and/or {100} facets, as those show at a higher frequency, and an increase in under-coordinated sites, such as {110} facets and/or edge sites.

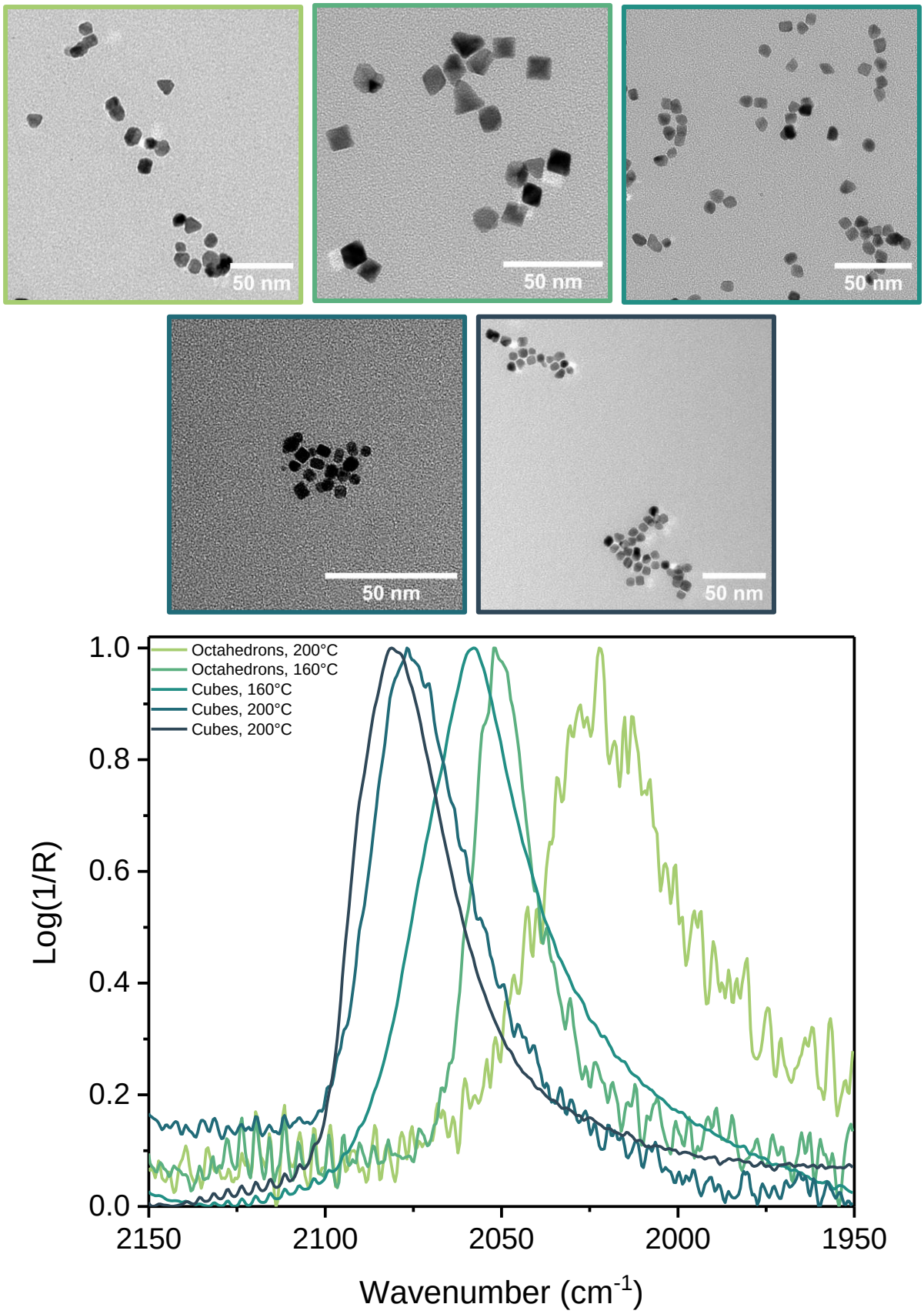

Figure 29 DRIFTS spectra of various Pt NPs with different shapes and synthesized at different temperatures. Light green: S27, green: S37, teal: S35, blue: S16, dark blue: S18. 'S' refers to synthesis, each synthesis' conditions can be found in Table 2.

5.3. Role of synthesis temperatures on CO adsorption

As the reaction temperature influenced the Pt-CO band position, the synthesis was reproduced at three different temperatures: 160, 180, and 200 °C. The FT-IR spectra are shown in Figure 30. The Pt-CO band shifted to higher wavenumbers with increasing temperatures for both the cubes and octahedrons, except for the octahedrons synthesized at 200 °C (S38). They show the Pt-CO band at 2011 cm^{-1}, similar to the results of S27. These results suggest that more under-coordinated sites, such as edges and corners, are formed at lower reaction temperatures. One hypothesis is that ridges have formed on the surface of the nanoparticles instead of a smooth surface. Higher-resolution HR-TEM pictures of the Pt nanoparticles were obtained to investigate these surfaces further. The surfaces of four samples were examined: cubes and octahedrons synthesised at 200 °C and 160 °C, as shown in Figure 31.

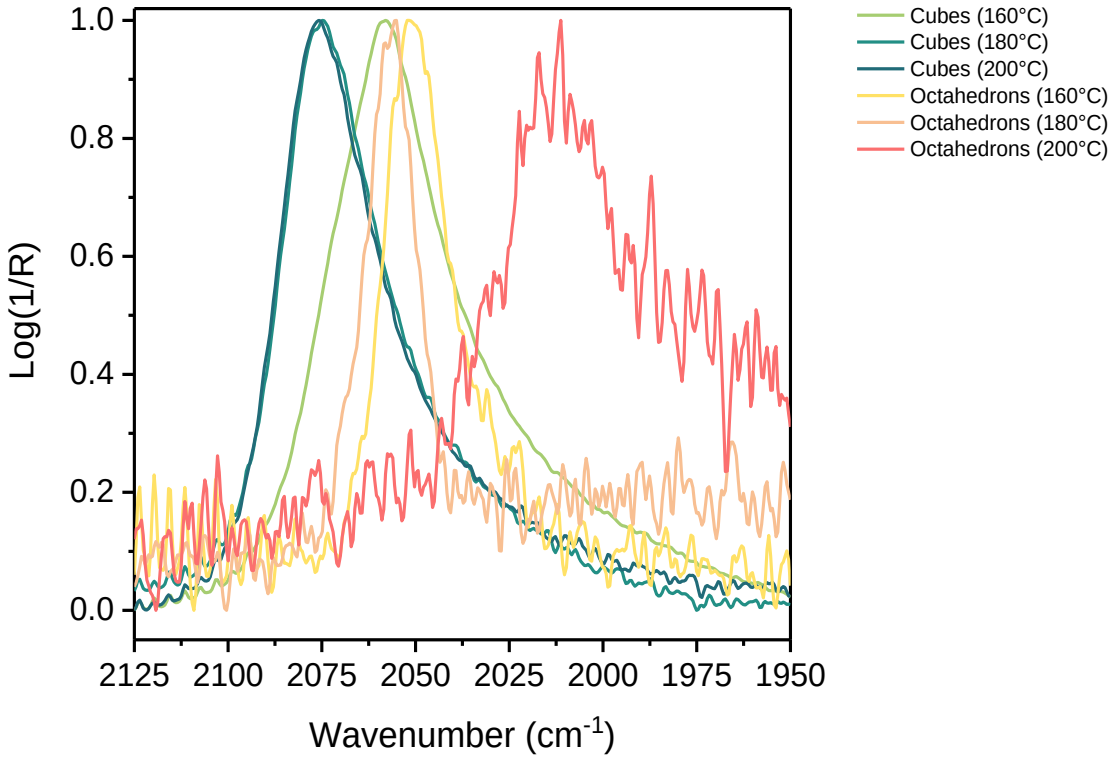

Figure 30 DRIFTS spectra after CO adsorption at room temperature for six different nanoparticles with a different shape and synthesized at different temperatures. Depicted are cubes at 160 °C (S35), cubes at 180 °C (S40), cubes at 200 °C (S42), octahedrons at 160 °C (S37), octahedrons at 180 °C (S39), octahedrons at 200 °C (S38). 'S' refers to synthesis, each synthesis' conditions can be found in Table 2.

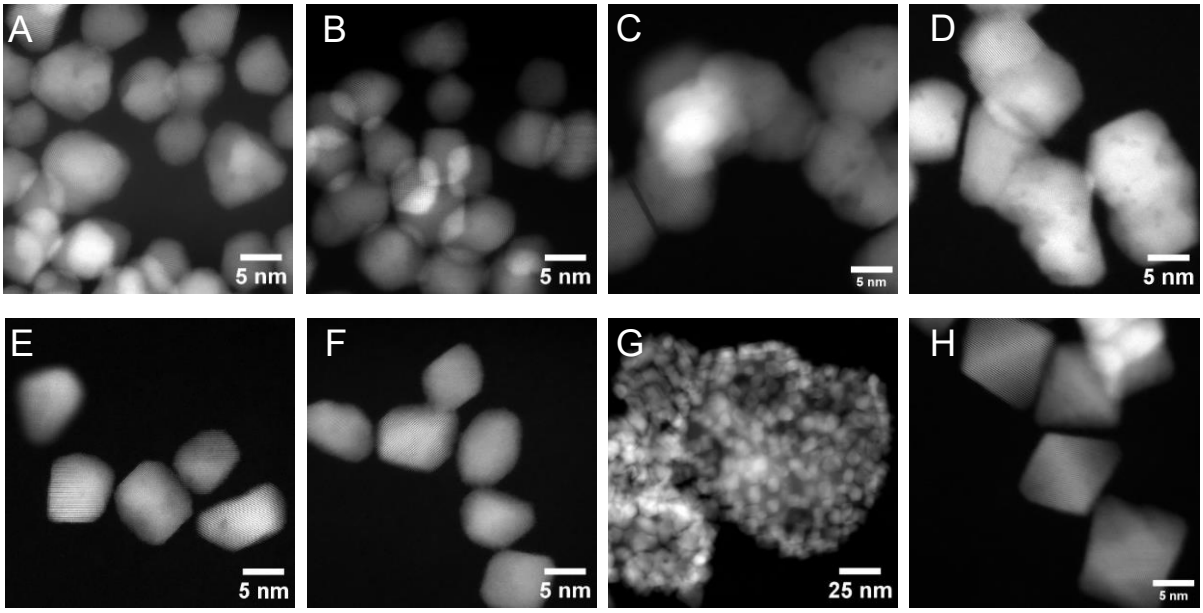

Figure 31 HR-TEM images of cubes at 200 °C – S18 (A and B), octahedrons at 200 °C – S27 (C and D), cubes at 160 °C – S35 (E and F), and octahedrons at 160 °C – S37 (G and H). 'S' refers to synthesis, each synthesis' conditions can be found in Table 2.

When comparing the HR-TEM images of the cubes synthesized at 200 °C (S18, Figure 31A, B) with those at 160 °C (S35, Figure 31E, F), no apparent differences are observed, although S18 seems less cubic-shaped than S35 and S35 has numerous shapes with two straight edges and two edges that appeared to be less straight and with more indentations and protrusions at the edge. This could confirm the hypothesis regarding the presence of ridges on S35. However, when looked at S18, they also appear to have these non-straight edges. It requires further investigation whether the edges of S18 and S35 are similar.

When comparing the octahedrons synthesized at 200 °C (S27, Figure 31C, D) with those synthesized at 160 °C (S37, Figure 31G, H), S37 reveals straighter edges and clear octahedron shapes, whereas S27 has no clear octahedron shape and many dark spots on the Pt NPs, indicating defects on the surface. These defects cause more adsorption sites with a low coordination number, causing the low Pt-CO band frequency of 2019 cm^{-1}. Additionally, the octahedrons were forming circle aggregates, clearly depicted in Figure 31G, and the beginning of a circle aggregation can also be seen in Figure 31C. The FT-IR signal of the octahedrons is often low, which could be explained by this aggregation. Because of this aggregation, less surface area is available for the CO to adsorb on.

Darker areas between Pt nanoparticles were seen in S27, as seen in the lower left corner of Figure 31C. An HR-TEM image and its corresponding EDX map can be seen in Figure 32. It identifies these darker areas as mainly silver atoms. It reveals that the silver is not washed away during the washing process and mainly concentrates itself between the Pt nanoparticles to form silver bridges. The silver could block the adsorption sites or alter the Pt electronic structure, causing a lower absorbance of the Pt-CO band.[77] When the CO adsorbs on the silver, this could also alter the Pt-CO band position if the Ag-CO band is in the same region.

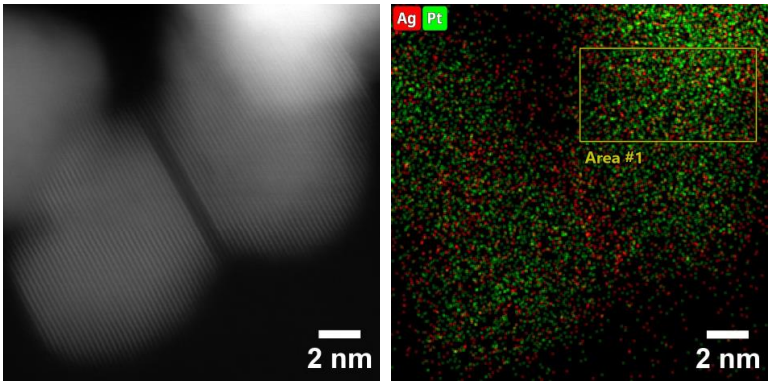

Figure 32 HR-TEM images with EDX mapping for Ag and Pt of S27 – octahedrons at 200 °C. 'S' refers to synthesis, each synthesis' conditions can be found in Table 2.

To determine whether a change in the surface facet caused the difference in the Pt-CO band position, the d-spacing of each sample was determined. Of at least 21 nanoparticles from each sample, the d-spacing was taken and categorized in one of the three categories: {111}, {100}, or {110} facets, as explained in Section 3.6.2. The results are shown in Figure 33. It shows that both cubic-shaped samples have more {111} facets than {100} facets, with the cubes synthesized at 160 °C having 90% {111} facets, making them the most octahedral-shaped nanoparticles of these four samples. In contrast, the octahedrons synthesized at 200 °C have the most {100} facets of these four samples and are thus the most cubic-shaped. However, these results seem contradictory to the TEM pictures, and it should be stated that these assessments were made to the best of my knowledge, and more research should be done on the surface facets of the synthesized Pt NPs.

Comparing these results to their corresponding Pt-CO band positions yields unexpected outcomes. It is expected from these results that the order from a high to low wavenumber will be as follows: cubes (S35, 160 °C) > octahedrons (S37, 160 °C) > cubes (S18, 200 °C) > cubes (S27, 200 °C). Comparing this to the FT-IR results, S27 is the only sample with the same position. Additionally, according to both results, S35 has a higher frequency band than S37. However, more HR-TEM pictures of different samples and facet determination on a more extensive nanoparticle set are required before any conclusions can be drawn.

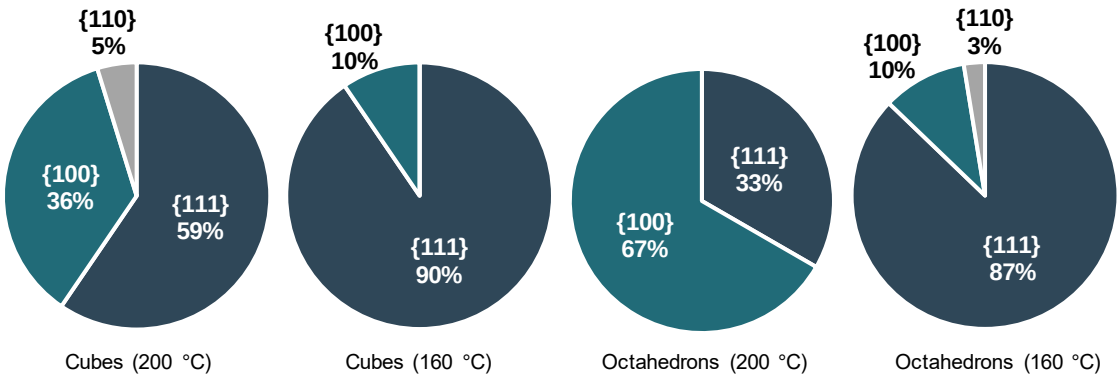

Figure 33 Facet determination of four Pt NP samples synthesized in a different way. The characterization of the surface facets was performed on HR-TEM images of the Pt NPs using Fourier transform. From left to right: S18, S35, S27, and S37. 'S' refers to synthesis, each synthesis' conditions can be found in Table 2.

5.4. Contributions of different CO sorption sites on CO band

CO adsorption measurements showed broad Pt-CO bands in the range of 2000–2100 cm^{-1} due to the contributions of various CO adsorption sites on Pt nanoparticles. Peak fitting allowed us to determine these individual peak positions and widths; the method is detailed in Section 3.7.5. In Figure 34, the fitted peaks in the DRIFTS spectrum of S18 can be seen. The exact peak positions and widths and the vibration causing each peak are documented in Table 7.

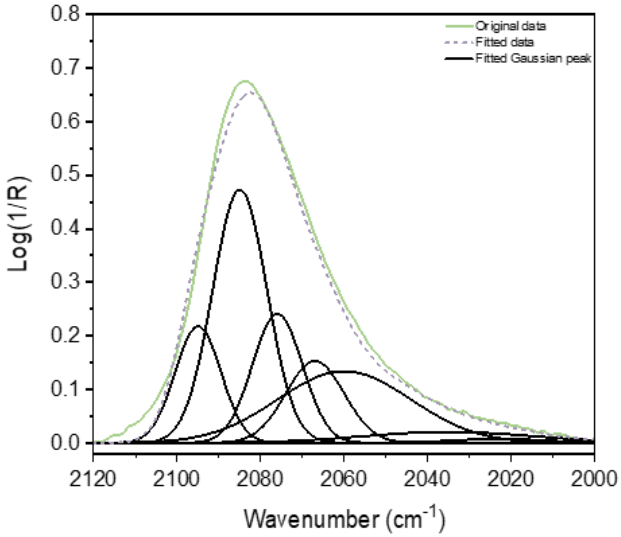

Figure 34 DRIFTS spectrum of S18 fitted with Gaussian peaks. 'S' refers to synthesis, each synthesis' conditions can be found in Table 2.

There is a linear relation between the Pt coordination number and peak position. With increasing coordination numbers, the peak frequency increases. However, assigning each peak to a definite adsorption site remains challenging. The edge adsorption sites alone received various assignments in the literature, ranging from 2050–2080 cm^{-1}. Therefore, two peaks are assigned to edge adsorption sites. It is more likely that, for instance, the 2076 cm^{-1} peak is due to Pt{111) or Pt{100} with defect sites, making the coordination number lower. Alternatively, it may be due to Pt{110} as it has a coordination number of 7, but no literature for this could be found. Furthermore, at low frequencies, peak assignment becomes even more difficult. The 2023 cm^{-1} peak is therefore assigned to all highly under-coordinated sites.

Peak position (cm^{-1})	Width (cm^{-1})	Assignment
2023	23	CO on highly under-coordinated sites[37]
2035	41	CO on corners[34,37,78]
2060	32	CO on defect sites[17]
2067	14	CO on edges[34,76,79]
2076	12	CO on edges[25]
2085	13	CO on Pt{100}[17,25,34,37,76,78,80]
2095	11	CO on Pt{111}[17,25,34,37,39,78,80]

Table 7 Fixed peak positions and widths of the fitted Gaussian peaks and the vibrational bond it is assigned to.

Later, it was observed that the synthesized octahedrons were covered in silver atoms, blocking the CO adsorption sites. Therefore, the peak fitting was solely done for Pt cubes and only one octahedron sample (S4). Consequently, discerning differences between cubes and octahedrons in CO adsorption measurements remains inconclusive. Furthermore, evaluating the peak areas in each fitted sample (Figure 35 and Figure 36) revealed no clear correlation between Pt nanoparticle size and adsorption sites. The irregular shapes of the synthesized Pt nanoparticles might contribute to this. In future research, more uniform Pt NPs in shape and size should be synthesized to study the effect of size and shape on the Pt-CO band.

However, when looking at the cubes synthesized at different temperatures – 160 °C (S35), 180 °C (S40), and 200 °C (S42), a difference can be seen. In S35, there is no contribution of the Pt{100} peak to the Pt-CO band. However, when the synthesis was done at higher temperatures, the Pt{100} and Pt{111} peak contributions appeared, and the under-coordinated peak contributions decreased. This aligns with our hypothesis; however, it contradicts our findings in the FFT analysis of the HR-TEM images in Section 5.3.

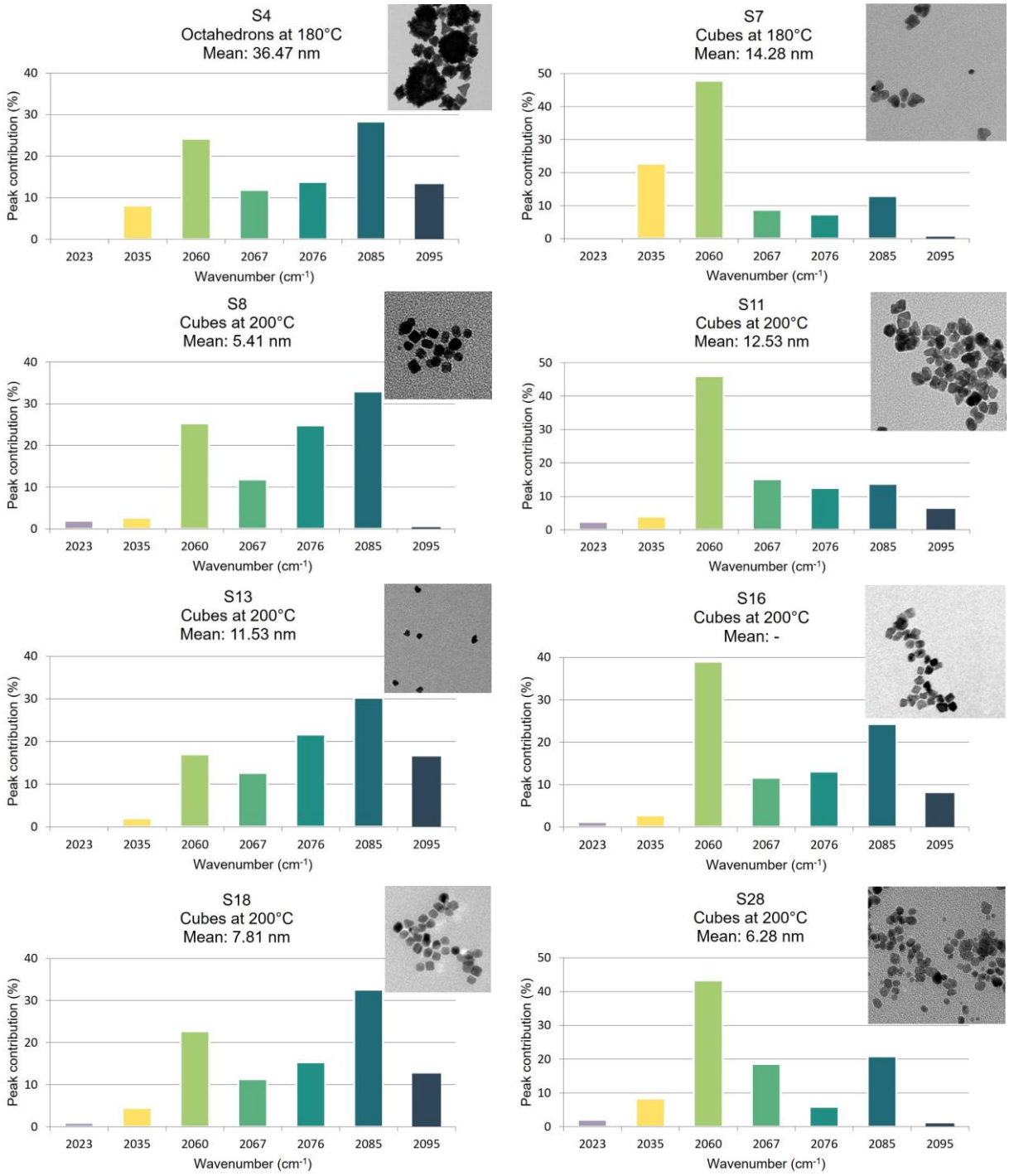

Figure 35 Bar charts of each sample that was used for the peak fitting, with the contribution of each peak to the total Pt-CO peak area in %. For S16 no average particle size is known. 'S' refers to synthesis, each synthesis' conditions can be found in Table 2.

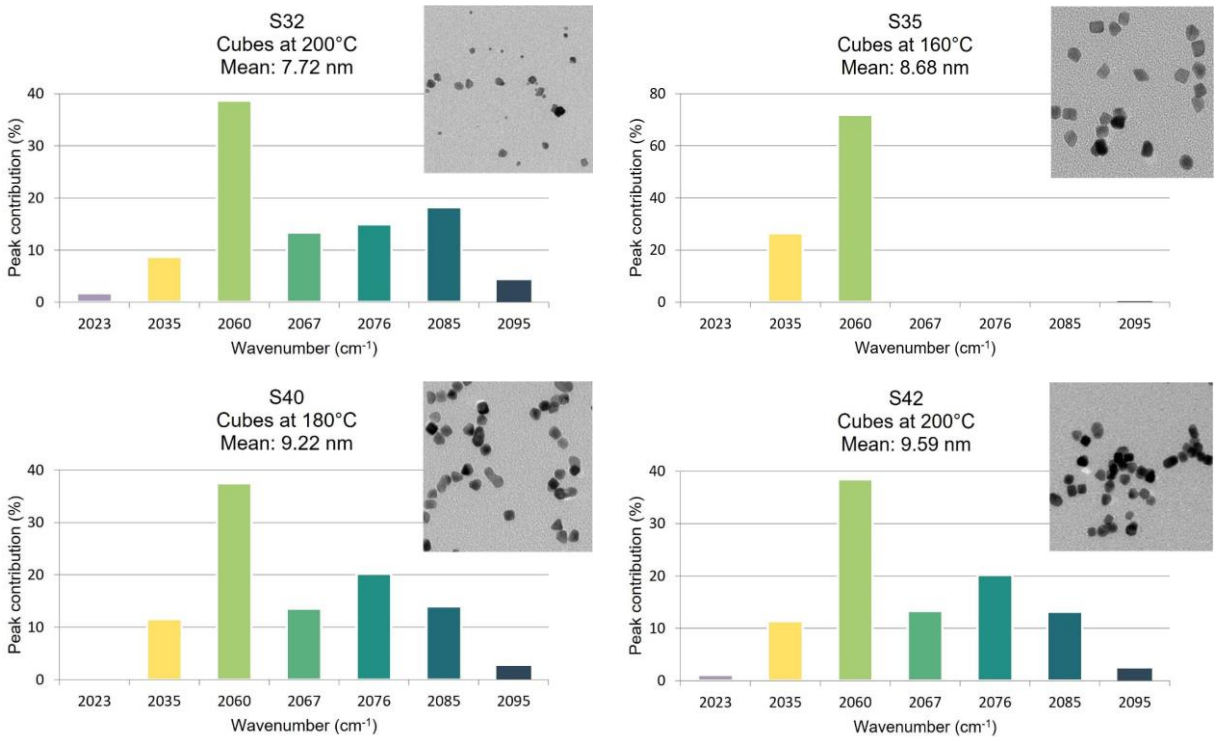

Figure 36 Bar charts of each sample that was used for the peak fitting, with the contribution of each peak to the total Pt-CO peak area in %. 'S' refers to synthesis, each synthesis' conditions can be found in Table 2.

5.5. Influence of oxidative and reductive heat treatments on Pt nanoparticles and CO adsorption

The primary objective is to monitor the shape change of Pt NPs during a reaction using CO-IR spectroscopy. A recent study captured 3D HAADF-STEM images of in situ hydrogenation and oxidation of Pt NPs, as seen in Figure 37. Following H_2 pretreatment, the truncated cube-shaped Pt nanoparticle transformed into a truncated octahedron. Subsequent O_2 pretreatment led to further transformation into a more spherical nanoparticle, featuring a high percentage of higher order index facets and a notable decrease in {100} facets. The reversibility of these changes was observed when the cycle was repeated, but it never entirely changed back to its original shape.

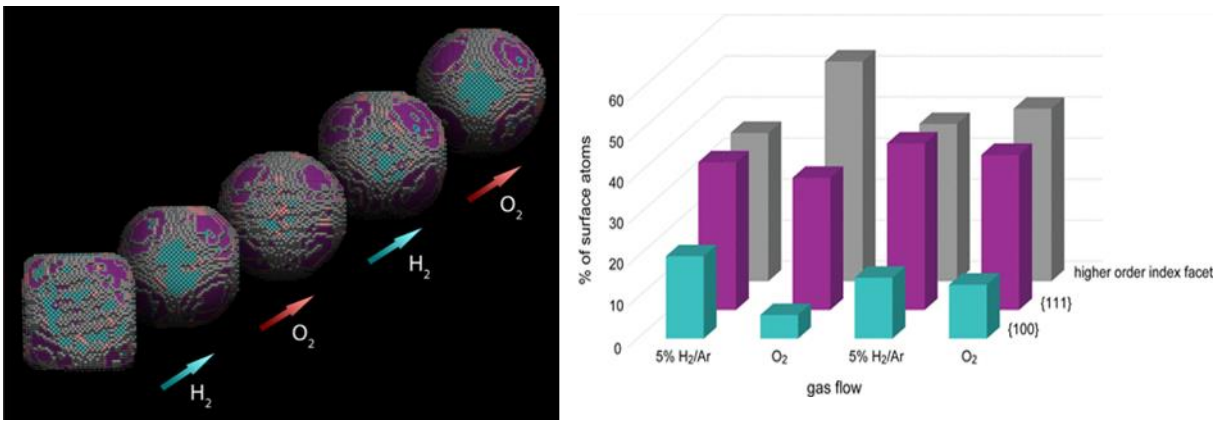

Figure 37 Left: Structural evolution of a Pt cubic NP after different gaseous environments. Right: Corresponding occurrence of different surface facets after different gaseous environments. Adapted from Altantzis et al. (2019).[69]

This study was replicated using CO-IR spectroscopy instead of HR-TEM to analyse the surface facet change. A single cycle of H_2 and O_2 pretreatments, with CO adsorption at room temperature in between, was performed on two samples: a cubic-shaped sample (S18) and a “shapeless” sample (S7). The CO-IR spectroscopy results are shown in Figure 38.

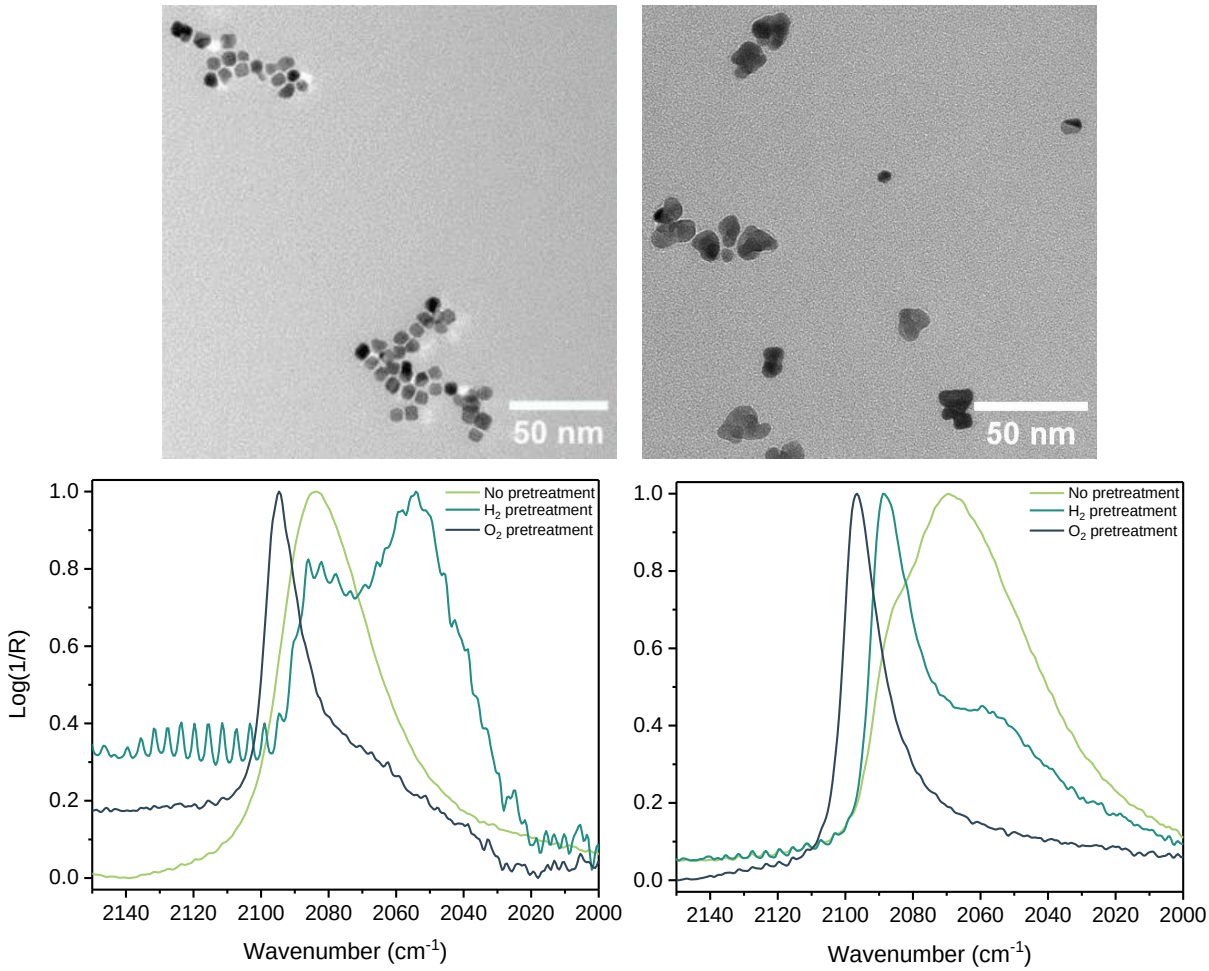

Figure 38 DRIFTS spectra of CO adsorption after subsequent H_2 and O_2 pretreatments. Left: Cubes (S18), right: Shapeless nanoparticles (S7). 'S' refers to synthesis, each synthesis' conditions can be found in Table 2.

After the H_2 pretreatment, both S18 and S7 show two distinct bands. The first band, around 2080 cm^{-1}, corresponds to well-coordinated adsorption sites such as {111} and {100} facets, and a second band, around 2050 cm^{-1}, corresponds to more under-coordinated sites such as edges. For the cubes, the overall band shifts to lower frequencies, and the band around 2050 cm^{-1} shows the highest intensity, which contrasts the results of the "shapeless" NPs, which show the highest band intensity around 2080 cm^{-1}. This band shift suggests that the H_2 reorders the "shapeless" nanoparticle into a more faceted shape while making the cube more roughly shaped.

Following O_2 pretreatment, the Pt-CO band for both cubes and "shapeless" nanoparticles shifts to higher wavenumbers. This observation aligns with the oxidation of Pt NPs during the pretreatment. When the Pt is oxidized, the d orbitals are less filled. This weakens the backdonation to the antibonding orbital in the CO bond, resulting in a stronger CO bond and a higher frequency for the CO stretching vibration.[30] Furthermore, as seen in Appendix E, TEM images of the Pt nanoparticles on silica were taken before and after this DRIFTS measurement and did not appear to change. This shows that CO-IR spectroscopy is a very sensitive technique, which shows changes in the nanoparticles not visible in TEM.

5.6. Catalytic reactivity during CO oxidation

CO oxidation measurements are done to measure the catalysts' activity. The activity difference between cubes synthesized at 200 °C (S18) and those synthesized at 160 °C (S35) was tested. The results of the CO oxidation measurements can be seen in Figure 39 for S18 and Figure 40 for S35. In both samples, the Pt-CO band shifted after the first CO oxidation cycle to higher wavenumbers, just below 2100 cm^{-1}, and then to wavenumbers just above 2100 cm^{-1} following a second CO oxidation cycle. This observation agrees with the theory that CO adsorption on oxidized Pt leads to a blueshift of the Pt-CO band.

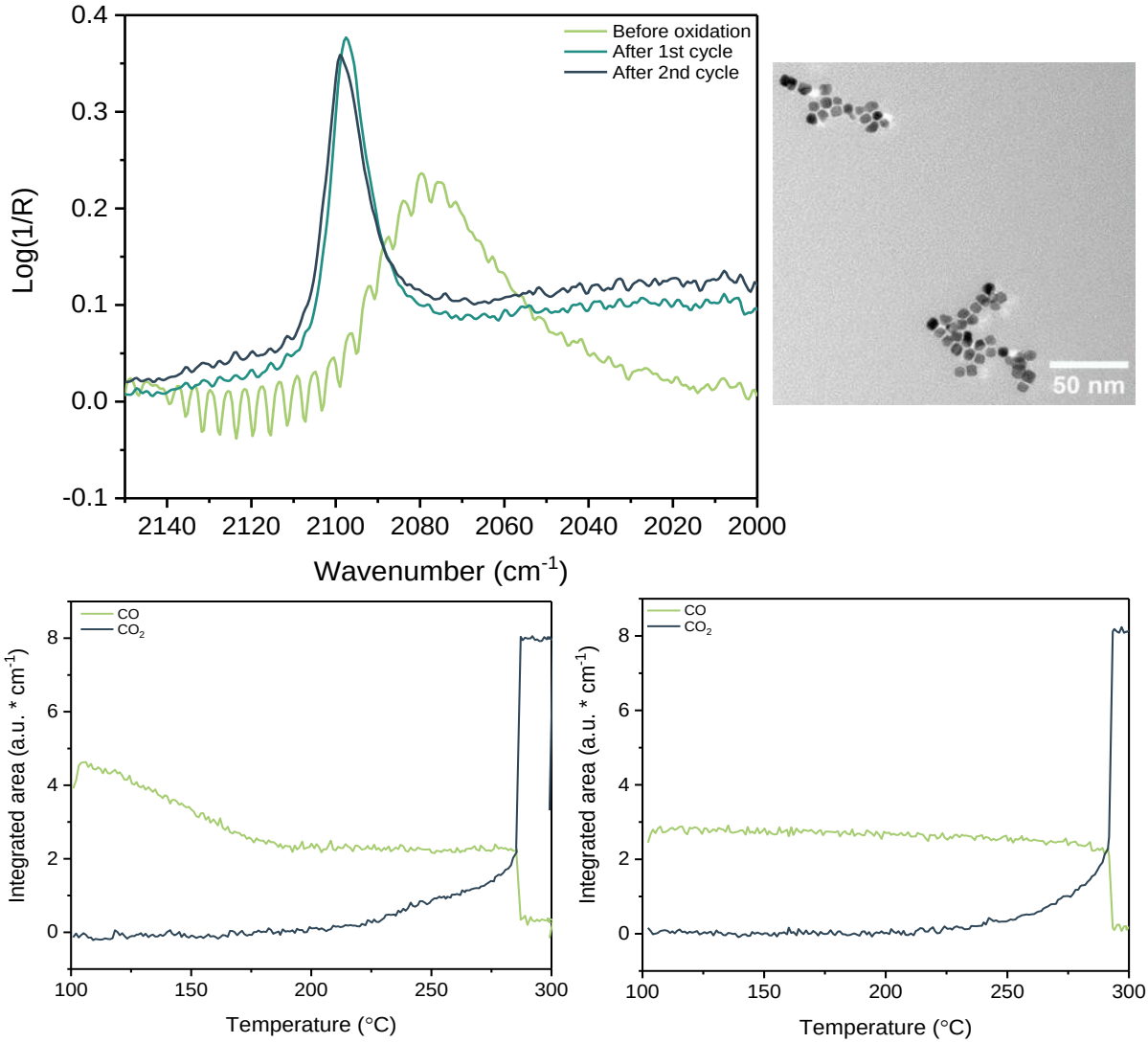

Figure 39 Top: DRIFTS spectrum of CO adsorption on S18 before and after two cycles of oxidation. Bottom: Integrated area change of the CO and CO_2 band plotted against temperature. Bottom left: First CO oxidation cycle. Bottom right: Second CO oxidation cycle. 'S' refers to synthesis, each synthesis' conditions can be found in Table 2.

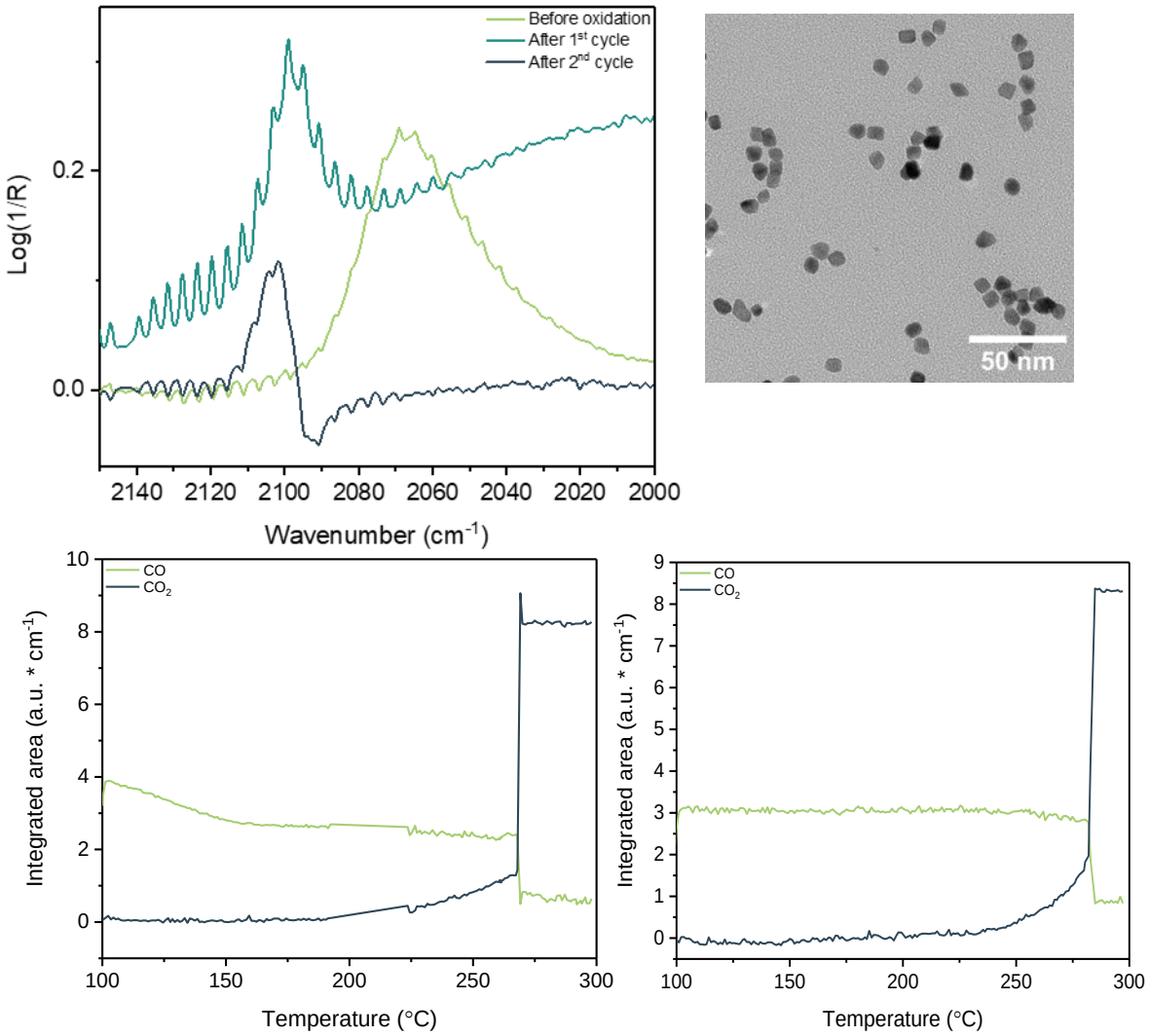

Figure 40 Top: DRIFTS spectrum of CO adsorption on S35 before and after two cycles of oxidation. Bottom: Integrated area change of the CO and CO_2 band plotted against temperature. Bottom left: First CO oxidation cycle. Bottom right: Second CO oxidation cycle. 'S' refers to synthesis, each synthesis' conditions can be found in Table 2.

Integration of the CO and CO_2 gas phase bands revealed a gradual increase in CO_2 concentration in all CO oxidation cycles. For the first cycle, both S18 and S35 show a gradual decrease in CO concentration at the beginning of the reaction, when the CO_2 concentration has not yet increased. In the second cycle, the CO concentration seems relatively stable throughout the reaction until a specific temperature threshold is reached; then, CO is rapidly converted into CO_2. A possible reason for the gradual decrease in CO concentration during the first cycle could be that the Pt NPs are already changing their shape at low temperatures, which causes fewer CO adsorption sites. However, it can also be due to an incorrect background subtraction. Ongoing research is being done to verify the correct background correction and accurate CO and CO2 peaks integration.

The DRIFTS spectra during heating at 100 °C and 200 °C for the first and second cycles are compared in Figure 41. Both cubic samples show similar behaviour: After the first oxidation cycle, the Pt-CO band splits into two bands, with the largest band showing at lower wavenumbers and a smaller band at higher wavenumbers, and after the second oxidation cycle, the Pt-CO band shifts only to lower wavenumbers.

When comparing the redshift of the Pt-CO band in both cycles, the redshift of the Pt-CO band is larger in the first cycle for both cubic samples. This observation suggests that the Pt NPs are rearranged primarily during the first cycle. The Pt-CO band splits into two bands, which can be assigned to well-coordinated (higher wavenumber) and more under-coordinated (lower wavenumber) adsorption sites. During the second cycle, both cubic Pt NPs (S18 and S35) have a similar shape. This is concluded from the conversion temperature being in the same range and the Pt-CO peak showing around the same frequency.

The conversion temperature varied for each sample and in each cycle (Table 8). S18 converts the CO to CO2 at 287 °C in its first cycle and at 290 °C in its second cycle, while S35 showed lower temperatures at 259 °C for the first cycle and 283–285 °C for the second cycle.

	Conversion temperature CO to CO_2 (°C)	
	Cubes at 160 °C (S35)	**Cubes at 200 °C (S18)**
Cycle 1	259	287
Cycle 2	283–285	290

Table 8 Temperature at which CO is almost completely converted to CO_2 on two different Pt/SiO_2 catalysts, cubic Pt NPs synthesized at 160 °C (S35) and 200 °C (S18). The CO oxidation reaction is repeated for a total of two times. 'S' refers to synthesis; each synthesis' conditions can be found in Table 2.

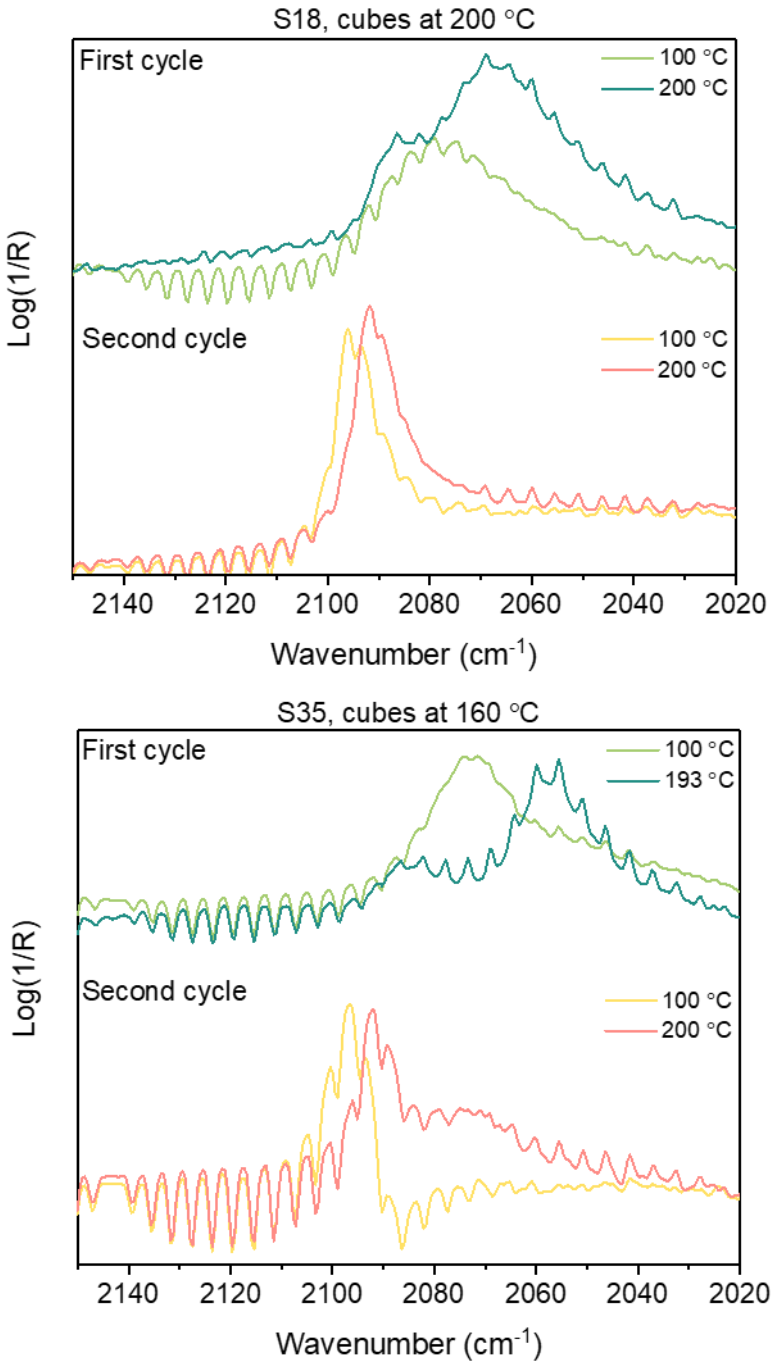

Figure 41 DRIFTS spectra during CO oxidation measurements at 100 °C and 200 °C. Top: Cubes synthesized at 200 °C. Bottom: Cubes synthesized at 160 °C. 'S' refers to synthesis, each synthesis' conditions can be found in Table 2.

6. Conclusions and outlook

In the polyol synthesis, multiple variables significantly influence the final shape and size of the Pt nanoparticle, such as temperature, stirring rate, and the method of adding the metal precursor and ligand. Increasing reaction temperatures were observed to shift the Pt-CO band to higher wavenumbers. While TEM revealed no apparent differences between the cubes synthesized at 160 °C and 200 °C (S35 and S18), HR-TEM showed a difference between the straightness of the samples' edges. Further image analysis on the edge straightness is planned. Additionally, it was found that S35 had more {111} facets than S18, although this warrants further investigation due to a small sample size.

Octahedrons often showed low absorption in CO adsorption measurements, sometimes showing a Pt-CO band at wavenumbers around 2015 cm^{-1}. HR-TEM images of octahedrons suggested that the low absorbance is likely caused by the incomplete washing of Ag from the NP surface, leaving silver bridges between nanoparticles, and circular aggregation of the nanoparticles, reducing the surface area and CO adsorption sites.

Facet determination from HR-TEM images showed that it is challenging to determine the facet with the help of TEM pictures. It is, therefore, difficult to say much about the CO adsorption results. However, variations in the Pt-CO band position change with different samples, suggesting that CO-IR spectroscopy is a promising characterization technique. Also, the Pt-CO bands' peak fitting showed no conclusive relations between Pt NP size and peak position. In the future, this should be redone with Pt NPs that are more uniform in shape and size. Nevertheless, seven peaks were found at 2095, 2085, 2076, 2067, 2060, 2035, and 2023 cm^{-1}. The highest-frequency peaks could be attributed to the Pt{111} and Pt{100} facets, respectively. Then, the peaks are attributed to edge, defects, corner, and highly undercoordinated adsorption sites, in that order.

When H_2 and O_2 pretreatments were applied, changes in the Pt-CO band showed potential for future in situ measurements. CO oxidation measurements proved that the activity of the Pt nanoparticles is facet-dependent, with cubes possessing more under-coordinated adsorption sites converting CO to CO_2 at lower temperatures than cubes with well-coordinated adsorption sites.

For future research, it is essential to study the synthesis parameters more, aiming for more uniformity in the Pt nanoparticles' shape and size. Subsequently, the surface facets should be characterized with HR-TEM, as it was shown that TEM is insufficient for characterization. EDX would be helpful to quantify any residual silver on the nanoparticles after the washing steps. This is particularly crucial when synthesizing octahedron-shaped Pt nanoparticles, where silver on the Pt nanoparticles was found to be adverse in CO-IR spectroscopy. Further research on developing techniques for removing silver without altering the shape and size of the Pt nanoparticles is needed. Additionally, for a catalysis study, Temperature Programmed Oxidation (TPO) can be used to establish at which temperature the Pt nanoparticles get oxidized, providing insights into their catalytic behaviour.

Acknowledgements

First and foremost, I would like to express my deepest appreciation to Dr. Bettina Baumgartner for being my daily supervisor and teaching me so much about doing research! Thank you for always staying late when the FTIR setup did not do what I wanted it to do again. I admire your enthusiasm, creativity in solving problems and overall knowledge, especially about spectroscopy. I loved working with you for the past year!

I am extremely grateful to Dr. Matteo Monai for always giving great feedback and tips during the meetings.

I want to thank Prof. Dr. Eelco Vogt for your valuable feedback and for being my examiner.

I would also like to thank Bram Kappé and Dr. Chunning Sun for tips for the synthesis and Joëlle Siewe, Savannah Turner, and Angela Melcherts for help with the setups. And, of course, the technicians in VMB, Jules van Leusden, Tim Prins, and Ramon Oord, for answering my technical questions.

Last, I want to thank the Inorganic Chemistry & Catalysis (ICC) group, whom I enjoyed working with in the lab. And, of course, the master students in VMB, Zamorano, Job, Singa, Alex, Ada, and Matthijs, from whom I learned so much and also had a lot of fun together.

Bibliography

1. Narayan, N., Meiyazhagan, A. & Vajtai, R. Metal Nanoparticles as Green Catalysts. *Materials* **12**, 3602 (2019).

2. Furukawa, S., Komatsu, T. & Shimizu, K.-I. Catalyst Design Concept Based on a Variety of Alloy Materials: A Personal Account and Relevant Studies. *J. Mater. Chem. A* **8**, 15620–15645 (2020).

3. Huang, L. *et al.* Advanced Platinum-Based Oxygen Reduction Electrocatalysts for Fuel Cells. *Acc. Chem. Res.* **54**, 311–322 (2021).

4. Jin, H. *et al.* Capping Agent-Free Synthesis of Surface Engineered Pt Nanocube for Direct Ammonia Fuel Cell. *Int. J. Energy Res.* **45**, 18281–18291 (2021).

5. Lin Hsin, Y., Chu Hwang, K. & Yeh, C.-T. Poly(vinylpyrrolidone)-Modified Graphite Carbon Nanofibers as Promising Supports for PtRu Catalysts in Direct Methanol Fuel Cells. *J. Am. Chem. Soc.* **129**, 9999–10010 (2007).

6. Dong, C. *et al.* Size-Dependent Activity and Selectivity of Carbon Dioxide Photocatalytic Reduction over Platinum Nanoparticles. *Nat. Commun.* **9**, 1252 (2018).

7. Haselmann, G. M. *et al.* In Situ Pt Photodeposition and Methanol Photooxidation on Pt/TiO2: Pt-Loading-Dependent Photocatalytic Reaction Pathways Studied by Liquid-Phase Infrared Spectroscopy. *ACS Catal.* **10**, 2964–2977 (2020).

8. Chen, J., Lim, B., Lee, E. P. & Xia, Y. Shape-Controlled Synthesis of Platinum Nanocrystals for Catalytic and Electrocatalytic Applications. *Nano Today* **4**, 81–95 (2009).

9. Grigoriev, S. A., Fateev, V. N., Middleton, H., Saetre, T. O. & Millet, P. A Comparative Evaluation of Palladium and Platinum Nanoparticles as Catalysts in Proton Exchange Membrane Electrochemical Cells. *Int. J. Nuclear Hydrogen Production and Application* **1**, 343 (2008).

10. Odularu, A. T., Ajibade, P. A., Mbese, J. Z. & Oyedeji, O. O. Developments in Platinum-Group Metals as Dual Antibacterial and Anticancer Agents. *J. Chem.* **2019**, 1–18 (2019).

11. Safdar, M. *et al.* Synthesis, Characterization and Applications of a Novel Platinum-Based Nanoparticles: Catalytic, Antibacterial and Cytotoxic Studies. *J. Inorg. Organomet. Polym. Mater.* **30**, 2430–2439 (2020).

12. Gutiérrez de la Rosa, S. Y., Muñiz Diaz, R., Villalobos Gutiérrez, P. T., Patakfalvi, R. & Gutiérrez Coronado, Ó. Functionalized Platinum Nanoparticles with Biomedical Applications. *Int. J. Mol. Sci.* **23**, 9409 (2022).

13. Rottenberg, S., Disler, C. & Perego, P. The Rediscovery of Platinum-Based Cancer Therapy. *Nat. Rev. Cancer* **21**, 37–50 (2021).

14. Zhang, C., Xu, C., Gao, X. & Yao, Q. Platinum-Based Drugs for Cancer Therapy and Anti-Tumor Strategies. *Theranostics* **12**, 2115–2132 (2022).

15. Subhramannia, M. & Pillai, V. K. Shape-Dependent Electrocatalytic Activity of Platinum Nanostructures. *J. Mater. Chem.* **18**, 5858–5870 (2008).

16. Cheong, S., Watt, J. D. & Tilley, R. D. Shape Control of Platinum and Palladium Nanoparticles for Catalysis. *Nanoscale* vol. 2 2045–2053 Preprint at https://doi.org/10.1039/c0nr00276c (2010).

17. Schmidt, E., Kleist, W., Krumeich, F., Mallat, T. & Baiker, A. Platinum Nanoparticles: The Crucial Role of Crystal Face and Colloid Stabilizer in the Diastereoselective Hydrogenation of Cinchonidine. *Chem. Eur. J.* **16**, 2181–2192 (2010).

18. Sarıbıyık, O. Y., Resasco, D. E., Sarıbıyık, O. Y. & Resasco, D. E. Selective Hydrogenation of Croton Aldehyde on Pt Nanoparticles Controlled by Tailoring Fraction of Well-Ordered Facets Under Different Pretreatment Conditions. *Catal. Lett.* 1–13 (2023) doi:10.1007/s10562-023-04453-5.

19. Herricks, T., Chen, J. & Xia, Y. Polyol Synthesis of Platinum Nanoparticles: Control of Morphology with Sodium Nitrate. *Nano Lett.* **4**, 2367–2371 (2004).

20. Chen, J., Herricks, T. & Xia, Y. Polyol Synthesis of Platinum Nanostructures: Control of Morphology through the Manipulation of Reduction Kinetics. *Angew. Chem. Int. Ed.* **44**, 2589–2592 (2005).

21. Fievet, F. *et al.* The Polyol Process: A Unique Method for Easy Access to Metal Nanoparticles with Tailored Sizes, Shapes and Compositions. *Chem. Soc. Rev.* **47**, 5187–5233 (2018).

22. Viet Long, N. *et al.* Sharp Cubic and Octahedral Morphologies of Poly(vinylpyrrolidone)-Stabilised Platinum Nanoparticles by Polyol Method in Ethylene Glycol: Their Nucleation, Growth and Formation Mechanisms. *J. Exp. Nanosci.* **7**, 133–149 (2012).

23. Song, H., Kim, F., Connor, S., Somorjai, G. A. & Yang, P. Pt Nanocrystals: Shape Control and Langmuir-Blodgett Monolayer Formation. *J. Phys. Chem. B* **109**, 188–193 (2005).

24. Lentz, C., Jand, S. P., Melke, J., Roth, C. & Kaghazchi, P. DRIFTS Study of CO Adsorption on Pt Nanoparticles Supported by DFT Calculations. *J. Mol. Catal. A Chem.* **426**, 1–9 (2017).

25. Avanesian, T. *et al.* Quantitative and Atomic-Scale View of CO-Induced Pt Nanoparticle Surface Reconstruction at Saturation Coverage via DFT Calculations Coupled with in Situ TEM and IR. *J. Am. Chem. Soc.* **139**, 4551–4558 (2017).

26. Garnier, A., Sall, S., Garin, F., Chetcuti, M. J. & Petit, C. Site Effects in the Adsorption of Carbon Monoxide on Real 1.8 nm Pt Nanoparticles: An Infrared Investigation in Time and Temperature. *J. Mol. Catal. A Chem.* **373**, 127–134 (2013).

27. Kale, M. J. & Christopher, P. Utilizing Quantitative in Situ FTIR Spectroscopy To Identify Well-Coordinated Pt Atoms as the Active Site for CO Oxidation on Al2O3-Supported Pt Catalysts. *ACS Catal.* **6**, 5599–5609 (2016).

28. Meunier, F. C. Relevance of IR Spectroscopy of Adsorbed CO for the Characterization of Heterogeneous Catalysts Containing Isolated Atoms. *J. Phys. Chem. C* **125**, 21810–21823 (2021).

29. Primet, M., Basset, J. M., Mathieu, M. V & Prettre, A. M. Infrared Study of CO Adsorbed on Pt/Al2O3. A Method for Determining Metal-Adsorbate Interactions. *J. Catal.* **29**, 213–223 (1973).

30. Zaera, F. Infrared Absorption Spectroscopy of Adsorbed CO: New Applications in Nanocatalysis for an Old Approach. *ChemCatChem* **4**, 1525–1533 (2012).

31. Ivanova, E., Mihaylov, M., Thibault-Starzyk, F., Daturi, M. & Hadjiivanov, K. FTIR Spectroscopy Study of CO and NO Adsorption and Co-Adsorption on Pt/TiO2. *J. Mol. Catal. A Chem.* **274**, 179–184 (2007).

32. Mihaylov, M., Chakarova, K., Hadjiivanov, K., Marie, O. & Daturi, M. FTIR Spectroscopy Study of CO Adsorption on Pt-Na-Mordenite. *Langmuir* **21**, 11821–11828 (2005).

33. Hadjiivanov, K. I. IR Study of CO and H2O Coadsorption on Pt n+/TiO2 and Pt/TiO2 Samples. *J. Chem. Soc. Faraday Trans.* **94**, 1901–1904 (1998).

34. Cheah, S. K., Bernardet, V. P., Franco, A. A., Lemaire, O. & Gelin, P. Study of CO and Hydrogen Interactions on Carbon-Supported Pt Nanoparticles by Quadrupole Mass Spectrometry and Operando Diffuse Reflectance FTIR Spectroscopy. *J. Phys. Chem. C* **117**, 22756–22767 (2013).

35. Maillard, F., Savinova, E. R., Simonov, P. A., Zaikovskii, V. I. & Stimming, U. Infrared Spectroscopic Study of CO Adsorption and Electro-oxidation on Carbon-Supported Pt Nanoparticles: Interparticle versus Intraparticle Heterogeneity. *J. Phys. Chem. B* **108**, 17893–17904 (2004).

36. Hammer, B., Nielsen, O. H. & Nørskov, J. K. Structure Sensitivity in Adsorption: CO Interaction with Stepped and Reconstructed Pt Surfaces. *Catal. Lett.* **46**, 31–35 (1997).

37. Kappers, M. J. & Van Der Maas, J. H. Correlation Between CO Frequency and Pt Coordination Number. A DRIFT Study on Supported Pt Catalysts. *Catal. Lett.* **10**, 365–374 (1991).

38. Greenler, R. G. & Brandt, R. K. The Origins of Multiple Bands in the Infrared Spectra of Carbon Monoxide Adsorbed on Metal Surfaces. *Colloids Surf. A: Physicochem. Eng. Asp.* **105**, 19–26 (1995).

39. Brandt, R. K., Hughes, M. R., Bourget, L. P., Truszkowska, K. & Greenler, R. G. The Interpretation of CO Adsorbed on Pt/SiO2 of Two Different Particle-Size Distributions. *Surf. Sci.* **286**, 15–25 (1993).

40. Fievet, F., Lagier, J. P., Blin, B., Beaudoin, B. & Figlarz, M. Homogeneous and Heterogeneous Nucleations in the Polyol Process for the Preparation of Micron and Submicron Size Metal Particles. *Solid State Ion.* **32–33**, 198–205 (1989).

41. Philipse, A. P. *Colloidal Dispersions [Course Material]*. (2023).

42. Wu, S., Li, M. & Sun, Y. Colloidal Nanoparticles In Situ Synchrotron X-ray Characterization Shining Light on the Nucleation and Growth Kinetics of Colloidal Nanoparticles. *Angew. Chem.* **131**, 9083–9091 (2019).

43. Thanh, N. T. K., Maclean, N. & Mahiddine, S. Mechanisms of Nucleation and Growth of Nanoparticles in Solution. *Chem. Rev.* **114**, 7610–7630 (2014).

44. Van Embden, J., Chesman, A. S. R. & Jasieniak, J. J. The Heat-Up Synthesis of Colloidal Nanocrystals. *Chem. Mater.* **27**, 2246–2285 (2015).

45. Varghese, N. & Rao, C. N. R. Growth Kinetics of Platinum Nanocrystals Prepared by Two Different Methods: Role of the Surface. *J. Colloid Interface Sci.* **365**, 117–121 (2012).

46. Xia, Y., Xiong, Y., Lim, B. & Skrabalak, S. E. Shape-Controlled Synthesis of Metal Nanocrystals: Simple Chemistry Meets Complex Physics? *Angew. Chem. Int. Ed.* **48**, 60–103 (2009).

47. Nguyen, T. D. From Formation Mechanisms to Synthetic Methods toward Shape-Controlled Oxide Nanoparticles. *Nanoscale* vol. 5 9455–9482 Preprint at https://doi.org/10.1039/c3nr01810e (2013).

48. Matsumoto, T. *et al.* Dissolution and Reduction of Cobalt Ions in the Polyol Process using Ethylene Glycol: Identification of the Active Species and its Role. *New J. Chem.* **39**, 5008–5018 (2015).

49. Biacchi, A. J. & Schaak, R. E. The Solvent Matters: Kinetic versus Thermodynamic Shape Control in the Polyol Synthesis of Rhodium Nanoparticles. *ACS Nano* **5**, 8089–8099 (2011).

50. Rodrigues, T. S. *et al.* Synthesis of Colloidal Metal Nanocrystals: A Comprehensive Review on the Reductants. *Chem. Eur. J.* **24**, 16944–16963 (2018).

51. Leong, G. J. *et al.* Shape-Directed Platinum Nanoparticle Synthesis: Nanoscale Design of Novel Catalysts. *Appl. Organometal. Chem.* **28**, 1–17 (2014).

52. Ding, R. *et al.* Size-Dependent Shape Distributions of Platinum Nanoparticles. *Nanoscale Adv.* **4**, 3978–3986 (2022).

53. Xia, Y., Gilroy, K. D., Peng, H. & Xia, X. Seed-Mediated Growth of Colloidal Metal Nanocrystals. *Angew. Chem. Int. Ed.* **56**, 60–95 (2017).

54. Safo, I. A., Werheid, M., Dosche, C. & Oezaslan, M. The Role of Polyvinylpyrrolidone (PVP) as a Capping and Structure-Directing Agent in the Formation of Pt Nanocubes. *Nanoscale Adv.* **1**, 3095–3106 (2019).

55. Ye, J.-Y. *et al.* Explicit Detection of the Mechanism of Platinum Nanoparticle Shape Control by Polyvinylpyrrolidone. *J. Phys. Chem. C* **120**, 7532–7542 (2016).

56. Song, T. *et al.* A Review of the Role and Mechanism of Surfactants in the Morphology Control of Metal Nanoparticles. *Nanoscale* vol. 13 3895–3910 Preprint at https://doi.org/10.1039/d0nr07339c (2021).

57. Fang, B., Chaudhari, N. K., Kim, M. S., Jung, H. K. & Yu, J. S. Homogeneous Deposition of Platinum Nanoparticles on Carbon Black for Proton Exchange Membrane Fuel Cell. *J. Am. Chem. Soc.* **131**, 15330–15338 (2009).

58. Williams, D. B. (David B. & Carter, C. Barry. *Transmission Electron Microscopy: A Textbook for Materials Science*. (Springer, 2009).

59. Niemantsverdriet, J. W. *Spectroscopy in Catalysis: An Introduction*. *Spectroscopy in Catalysis: An Introduction: Third Edition* (Wiley-VCH, 2007). doi:10.1002/9783527611348.

60. Franken, L. E., Grünewald, K., Boekema, E. J. & Stuart, M. C. A. A Technical Introduction to Transmission Electron Microscopy for Soft-Matter: Imaging, Possibilities, Choices, and Technical Developments. *Small* **16**, 1906198 (2020).

61. Wang, Z. L. Transmission Electron Microscopy of Shape-Controlled Nanocrystals and Their Assemblies. *J. Phys. Chem. B* **104**, 1153–1175 (2000).

62. McMurry, J. E. *Organic Chemistry*. (Cengage Learning, 2012).

63. Armaroli, T., Bécue, T. & Gautier, S. Diffuse Reflection Infrared Spectroscopy (DRIFTS): Application to the in situ Analysis of Catalysts. *Oil Gas Sci. Technol.- Rev. IFP* **59**, 215–237 (2004).

64. Sirita, J., Phanichphant, S. & Meunier, F. C. Quantitative Analysis of Adsorbate Concentrations by Diffuse Reflectance FT-IR. *Anal. Chem.* **79**, 3912–3918 (2007).

65. Hu, X., Wang, T. & Pong, S. Rapid Synthesis of Cubic Pt Nanoparticles and Their Use for the Preparation of Pt Nanoagglomerates. *J. Nanosci. Nanotechnol.* **6**, 2056–2061 (2006).

66. Lee, H. *et al.* Morphological Control of Catalytically Active Platinum Nanocrystals. *Angew. Chem.* **118**, 7988–7992 (2006).

67. Schindelin, J. *et al.* Fiji: An Open-Source Platform for Biological-Image Analysis. *Nat. Methods* **9**, 676–682 (2012).

68. Davey, W. P. Precision Measurements of the Lattice Constants of Twelve Common Metals. *Phys. Rev.* **25**, 753–761 (1925).

69. Altantzis, T. *et al.* Three-Dimensional Quantification of the Facet Evolution of Pt Nanoparticles in a Variable Gaseous Environment. *Nano Lett.* **19**, 477–481 (2019).

70. O'Haver, T. peakfit.m. *MATLAB Central File Exchange* https://www.mathworks.com/matlabcentral/fileexchange/23611-peakfit-m (2024).

71. Kappers, M. J., Miller, J. T. & Koningsberger, D. C. Deconvolution and Curve Fitting of IR Spectra for CO Adsorbed on Pt/K-LTL: Potassium Promoter Effect and Adsorption Site Distribution. *J. Phys. Chem.* **100**, 3227–3236 (1996).

72. Bai, J., Li, Y., Zhang, C., Liang, X. & Yang, Q. Preparing AgBr Nanoparticles in Poly(vinyl pyrrolidone) (PVP) Nanofibers. *Colloids Surf. A Physicochem. Eng. Asp.* **329**, 165–168 (2008).

73. Xian, J., Hua, Q., Jiang, Z., Ma, Y. & Huang, W. Size-Dependent Interaction of the Poly(N-vinyl-2-pyrrolidone) Capping Ligand with Pd nanocrystals. *Langmuir* **28**, 6736–6741 (2012).

74. Loría-Bastarrachea, M. I. *et al.* A TG/FTIR Study on the Thermal Degradation of Poly(Vinyl Pyrrolidone). *J. Therm. Anal. Calorim.* **104**, 737–742 (2011).

75. Borodko, Y., Lee, H. S., Joo, S. H., Zhang, Y. & Somorjai, G. Spectroscopic Study of the Thermal Degradation of PVP-Capped Rh and Pt Nanoparticles in H2 and O2 Environments. *J. Phys. Chem. C* **114**, 1117–1126 (2010).

76. Brandt, R. K., Sorbello, R. S. & Greenler, R. G. Site-Specific, Coupled-Harmonic-Oscillator Model of Carbon Monoxide Adsorbed on Extended, Single-Crystal Surfaces and on Small Crystals of Platinum. *Surf. Sci.* **271**, 605–615 (1992).

77. Grass, M. E. *et al.* Silver Ion Mediated Shape Control of Platinum Nanoparticles: Removal of Silver by Selective Etching Leads to Increased Catalytic Activity. *J. Phys. Chem. C* **112**, 4797–4804 (2008).

78. Coloma, F., Coronado, J. M., Rochester, C. H. & Anderson, J. A. Infrared Study of Crotonaldehyde and CO Adsorption on a Pt/TiO2 Catalyst. *Catal. Lett.* **51**, 155–162 (1998).

79. Raskó, J. CO-Induced Surface Structural Changes of Pt on Oxide-Supported Pt Catalysts Studied by DRIFTS. *J. Catal.* **217**, 478–486 (2003).

80. Pillonel, P. *et al.* Impact of the Support on the Heat of Adsorption of the Linear CO Species on Pt-Containing Catalysts. *App. Catal. A: Gen.* **278**, 223–231 (2005).

81. Peng, Z. & Yang, H. Designer Platinum Nanoparticles: Control of Shape, Composition in Alloy, Nanostructure and Electrocatalytic Property. *Nano Today* **4**, 143–164 (2009).

82. Wang, Y., Liu, Z., Pan, H. & Tang, R. Biomineralization Inspired Crystal Growth for Biomimetic Materials Preparation. *J. Cryst. Growth* **603**, 127029 (2023).

83. Livshits, V., Philosoph, M. & Peled, E. Direct Ethylene Glycol Fuel-Cell Stack - Study of Oxidation Intermediate Products. *J. Power Sources* **178**, 687–691 (2008).

Appendix

Appendix A: Calculation of the proportionality constant $\boldsymbol{\beta}$

The surface contribution of the total Gibbs free energy of a cluster changes with total surface area (A) and the surface tension (γ), as seen in Equation 16.

$$\Delta \boldsymbol{G(surface) = \gamma A} \tag{16}$$

The proportionality constant $\boldsymbol{\beta}$ of each shape can be calculated by setting Equation 16 equal to Equation 2, as seen in Equations 17 and 18.

$$\boldsymbol{\gamma A = \gamma \beta (\nu_m N)^{\frac{2}{3}}} \tag{17}$$

$$\boldsymbol{A = \beta (\nu_m N)^{\frac{2}{3}}} \tag{18}$$

As $\nu_m = \frac{V}{N}$, $\nu_m N$ is equal to the total volume of the cluster. In conclusion, the proportionality constant is calculated by Equation 19.

$$\boldsymbol{\beta = \frac{A}{V^{\frac{2}{3}}}} \tag{19}$$

In Table 9, equations for the surface area and volume of the shapes relevant to this research can be seen. Here, *r* is the radius of a sphere, *d* is the side of a cube, and *a* is the edge of an octahedron.

Shape	*Surface area, A*	*Volume, V*
Sphere	$4\pi r^2$	$\frac{4}{3}\pi r^3$
Cube	$6d^2$	d^3
Octahedron	$2\sqrt{3}a^2$	$\frac{\sqrt{2}a^3}{3}$

Table 9 Equations for the surface area and volume for three different shapes: sphere, cube, and octahedron.

By inserting the equations for surface area and volume into Equation 19, the following proportionality constants are calculated for spheres, cubes, and octahedrons (Equations 20–22):

$$\boldsymbol{\beta_{sphere} = \frac{4\pi r^2}{\left(\frac{4}{3}\pi r^3\right)^{\frac{2}{3}}} = \frac{4\pi}{\left(\frac{4}{3}\pi\right)^{\frac{2}{3}}} \approx 4.84} \tag{20}$$

$$\boldsymbol{\beta_{cube} = \frac{6d^2}{(d^3)^{\frac{2}{3}}} = 6} \tag{21}$$

$$\boldsymbol{\beta_{octahedron} = \frac{2\sqrt{3}a^2}{\left(\frac{\sqrt{2}a^3}{3}\right)^{\frac{2}{3}}} = \frac{2\sqrt{3}}{\left(\frac{\sqrt{2}}{3}\right)^{\frac{2}{3}}} \approx 5.72} \tag{22}$$

Appendix B: Matlab code DRIFTS analysis

```
%% loading
clc, clearvars, close all

addpath('C:\...\MATLAB\Natsortfiles')

% Get a list of all files in the folder with the desired file name pattern.
ascfiles = dir('*.txt');
N = length(ascfiles);
ascfiles2 = struct2cell(ascfiles);
filenames = ascfiles2(1,:);
sortedfilenames = natsortfiles(filenames(1, :));
delimiterIn = '\t';
wavenumbers = {};
baseline0 = {};
raw = {};


for r = 1
    tempfile = importdata(sortedfilenames{r}, delimiterIn);
    wavenumbers = [wavenumbers, tempfile(:, 1)];
end

for r = ..
    tempfile = importdata(sortedfilenames{r}, delimiterIn);
    baseline0 = [baseline0, tempfile(:, 2)];
end

for r = 1:N
    tempfile = importdata(sortedfilenames{r}, delimiterIn);
    raw = [raw, tempfile(:, 2)];
end

%Cell to matrix
wn = cell2mat(wavenumbers);
baseline0 = cell2mat(baseline0);
raw2 = cell2mat(raw);

%%
%Plot raw data

x = wn(:, 1);
y = raw2(:, :);

figure;
plot (x,y)

% set color
cmap = flip(summer(N),1); % (for N-1 lines)
set(gca(),'ColorOrder',cmap)
set(gca, 'XDir','reverse')

% add names and labels
xlabel("Wavenumber (cm-1)")
ylabel("Energy (J)")

%% Convert energy to absorption

for r = 1:N
```

```
    absorption0(:, r) = log(baseline0(:, 1)./ raw2(:, r));
end

%absorption0(:,all(absorption0 == 0))=[]; % removes column if the entire column is zero

%%
figure;
plot(x, absorption0(:, 1:N))

% set color
cmap = flip(summer(N),1); % (for # lines)
set(gca(),'ColorOrder',cmap)
set(gca, 'XDir','reverse')

% add names and labels
xlabel("Wavenumber (cm-1)")
ylabel("Absorbance (a.u.)")

%% Set certain point to zero
% set y-value to zero when x = 2451.47 in each column of y
[~, idx] = min(abs(wn - 2451.47), [], 1);
for r = 1:N
    data(:, r) = absorption0(:, r) - absorption0(idx, r);
end

% Plot data

figure;
plot(wn, data(:, 1:N));

% set color
cmap = flip(summer(N),1); % (for amount of lines lines)
set(gca(),'ColorOrder',cmap)
set(gca, 'XDir','reverse')

% add names and labels
xlabel("Wavenumber (cm-1)")
ylabel("Absorbance (a.u.)")


%% Plot only CO peak (2300 cm-1 - 1850 cm-1) 880:1137

figure;
plot (wn(3525:4458), data(3525:4458, [30, 47, 64, 76, 88, 100, 112]))

% set color
cmap = flip(summer(7),1); % (for N-2 lines)
set(gca(),'ColorOrder',cmap)
set(gca, 'XDir','reverse')

% add names and labels
xlabel("Wavenumber (cm-1)")
ylabel("Absorbance (a.u.)")


%% Plot only CO  and CO2 peaks (2450 cm-1 - 1850 cm-1) 880:1137

figure;
plot (wn(3266:4458), data(3266:4458, 107:205))
```

```
% set color
cmap = flip(summer(99),1); % (for N-2 lines)
set(gca(),'ColorOrder',cmap)
set(gca, 'XDir','reverse')

% add names and labels
xlabel("Wavenumber (cm-1)")
ylabel("Absorbance (a.u.)")
```

Appendix C: Peak fitting Matlab code

```
%%

absoshort=data(wn>2000 & wn<2100, (153));
wnshort=wn(wn>2000 & wn<2100);
figure(678)
plot(wnshort,absoshort)

%%

center=0;
    window=0;
    NumPeaks=5;
    NumTrials=100;
    autozero=1;
    shape=16; % 16 for fixed position Gauss, 1 for just Gauss; 17 for fixed postin Lorentz, 50 for mix

     %position=[2039 2058 2079 2087]';
     position=[2039 2058 2068 2079 2087 2092]';
     %position=[2037 2060 2067 2077 2085]';
    %position=[1 1 1 1; 2040 2068 2079 2087; 36.6 30 22.8 16.5]';
    %position=[1 1 1; 2040 2079 2095; 36.6 22.8 10]';
    %position=[1 1 1; 2040 2068 2079; 40.8 29.9 22.2]';
     minwidth=1;
    signal=[wnshort absoshort];
    figure(78)
[FitResults, GOF, xi, yi] = peakfit(signal,center,window,NumPeaks,shape,1,NumTrials,0,autozero,position,1,0,minwidth);
```

Appendix D: CO integration Matlab code

```
clearvars -except raw wn areascn1
%% Important Inputs
scantime=1; %time for one scan in opus in s
navg=1; %number of spectra to be averaged
saveresults=true;
addpath('C:\...\Natsortfiles');
%% Load all Spectra in folder
files = dir('*sample*.txt');
filescells=struct2cell(files);
sortedfiles=string(natsortfiles(filescells(1,:))');

raw=load(char(sortedfiles(1)));
wn=raw(:,1);
raw=[raw(:,2) zeros(length(files)-1,length(raw(:,2)))'];

for uu=2:length(files)
    temp=load(char(sortedfiles(uu)));
    raw(:,uu)=temp(:,2);
end
%%
raw2=raw(wn>800 & wn<4000,:);
wn2=wn(wn>800 & wn<4000);
%% calculate Background spectrum
%bg=mean(raw(:,1:floor(bgtime/scantime)),2);
bgnum=12;
bg=raw2(:,bgnum);


%% calculate spectrum

figure(1)
plot(wn2,raw2)

abso=log10(bg./raw2);


from=1;
to=600;
absoshort=abso(:,from:to);
figure(2)
clf
hold on
 set(gca, 'XDir','reverse')
plot(wn2,absoshort)
%xlim([1900 2500])

%% BG corr
clearvars absocorr pp
for pp=1:size(abso,2)

    absocorr(:,pp)=abso(:,pp)-abso(wn2>2440 & wn2<2440.5,pp);

end
figure(223)
clf
plot(wn2,absocorr)
```

```
%% define time axis
%t=linspace(scantime*(navg/2),scantime*(size(raw2,2)-navg/2),size(spectraavg,2)); %in min
t=[1:size(absocorr,2)];
%% CO integration
clearvars area_CO2_0deg area_CO2_90deg
blleftbn=5; %averaging wavenumber above area
blrightbn=5; %averaging wavenumber below area

intCN= [2250 2140]; %CO

for oo=1:size(absocorr,2)
abso=absocorr(:,oo);
blbn1=mean(abso((wn2<(intCN(1)+blleftbn)) & (wn2>(intCN(1))),:));
blbn2=mean(abso((wn2>(intCN(2)-blrightbn)) & (wn2<(intCN(2))),:));
k1=(blbn2-blbn1)/(intCN(2)-blrightbn/2-intCN(1)-blleftbn/2);
d1=blbn1-k1*(intCN(1)+blleftbn/2);

% Integration Area defined
integrationarea=absocorr((wn2>intCN(2)) & (wn2<intCN(1)),oo);
baseline2=k1.*wn2((wn2>intCN(2)) & (wn2<intCN(1)))+d1;
wnshort1=wn2((wn2>intCN(2)) & (wn2<intCN(1)));
% Integration

areabn=trapz(flip(wnshort1),integrationarea-baseline2,1);
area_CO(oo,:)=areabn;

end

figure(8)
plot(t,area_CO)
xlabel('time(min)')
ylabel('CO area (A.U.*cm^-1)')

%% CO2 integration
clearvars area_CO2_0deg area_CO2_90deg
blleftbn=5; %averaging wavenumber above area
blrightbn=5; %averaging wavenumber below area

intCN= [2400 2240]; %CO

for oo=1:size(absocorr,2)
abso=absocorr(:,oo);
blbn1=mean(abso((wn2<(intCN(1)+blleftbn)) & (wn2>(intCN(1))),:));
blbn2=mean(abso((wn2>(intCN(2)-blrightbn)) & (wn2<(intCN(2))),:));
k1=(blbn2-blbn1)/(intCN(2)-blrightbn/2-intCN(1)-blleftbn/2);
d1=blbn1-k1*(intCN(1)+blleftbn/2);

% Integration Area defined
integrationarea=absocorr((wn2>intCN(2)) & (wn2<intCN(1)),oo);
baseline2=k1.*wn2((wn2>intCN(2)) & (wn2<intCN(1)))+d1;
wnshort1=wn2((wn2>intCN(2)) & (wn2<intCN(1)));
% Integration

areabn=trapz(flip(wnshort1),integrationarea-baseline2,1);
area_CO2(oo,:)=areabn;

end

figure(8)
hold on
```

```
plot(t,area_CO2./10)
xlabel('time(min)')
ylabel('CO area (A.U.*cm^-1)')

%% ramping periods

% check here if the ramping starting min (spectra) are right

t_ramping1=t(t>23 & t<222)-23;
area_CO_R1=area_CO(t>23 & t<222,:);

t_ramping2=t(t>346 & t<545)-346;
area_CO_R2=area_CO(t>346 & t<545,:);

start_temp=23;
end_temp=300;
steps=size(area_CO_R1,1);
temperature = linspace(start_temp,end_temp,steps);  % interpolation for temperture -> insert real numbers

figure('Name','CO concentration during ramping');
plot(temperature,area_CO_R1)
hold on
plot(temperature,area_CO_R2)
xlabel('Temperature (°C)')
ylabel('CO area (A.U.*cm^-1)')

%% gas line substraction
upper=2250;
lower=2000;%2354;%2200;
absoshort2=absocorr(wn2>lower & wn2<upper,:);
wnshort=wn2(wn2>lower & wn2<upper);
%
figure(78)
clf
plot(wnshort,absoshort2)
%%

%% CO gas phase substraction
addpath('C:\...\ ');

upper=2250;
lower=2000;%2145;%2354;%2200;


% load CO reference spectrum

waterraw=load('C:\...\ '); % reference CO spectrum

water2=waterraw(waterraw>lower & waterraw<upper,:);
water=water2(1:end,:);
waterwn=water2(:,1);
waterabs=water(:,2);

figure(66)
plot(waterwn,waterabs)
%%
% Fit CO2
clearvars absoCO2corr absoCO2corr2
%absoCO2short=abso2(wn>lower & wn<upper,:);
```

```
absocorr_CO=absocorr;
for kk=1:size(absocorr,2)

    upper=2250;

    absoshort1=absocorr(wn2>lower & wn2<upper,kk);
    fitfun=@(x,xdata) scaledwater(waterwn,waterabs,x(1),x(2),x(3));
    x0=[0.5 10 0];
    ub=[100 10 3]; %upper boundery
    lb=[-100 -10 -3];
    xfitted=lsqcurvefit(fitfun,x0,waterwn,absoshort1,lb,ub);

%     figure(66)
%     clf
%     plot(waterwn,absoshort1)
%     hold on
%     plot(waterwn,waterabs*xfitted(1))

    upper2=upper;
    lower2=2000;
    absoshort2=absocorr(wn2>lower2 & wn2<upper2,kk);
    wnshort2=wn2(wn2>lower2 & wn2<upper2);

    water22=waterraw(waterraw>lower2 & waterraw<upper2,:);
    waterwn2=water22(:,1);
    waterabs2=water22(:,2);


    waterscaled=waterabs2*xfitted(1)*1.25; % random fixing factor
    absofit2=absoshort2-waterscaled;
    upper3=2250;
    lower3=2000;
    absofit3=absofit2(waterwn2>lower3 & waterwn2<upper3);
    absocorr_CO(wn2>lower3 & wn2<upper3,kk)=absofit3;
end
%%
figure(568)
clf
c=summer(size(absocorr_CO,2));
hold on
for oo=2:size(absocorr_CO,2)
    plot(wn2,absocorr_CO(:,oo),'color',c(oo,:),'LineWidth',1)
end
 set(gca, 'XDir','reverse')
xlim([2000 2450])


%% plot selected spectra

from=345;
to=555;
abso_COcorr_selected=absocorr_CO(:,from:to);
c=turbo(size(abso_COcorr_selected,2));
figure(56)
clf
hold on
for oo=2:size(abso_COcorr_selected,2)
    plot(wn2,abso_COcorr_selected(:,oo),'color',c(oo,:),'LineWidth',1)
end
 set(gca, 'XDir','reverse')
```

```
xlim([2000 2150])
xlabel('Wavenumber (cm-1)')
ylabel('Absorbance (A.U.)')

%% save random spectrum

saverandom=[wn2 absocorr(:,716)];
save('test_CO_spectrum.txt','saverandom','-ascii')

%%
function [specout] = scaledwater(xaxis,refspec,scale,k,d)
    specout=refspec*scale+k*(xaxis-mean(xaxis))+d;
end
```

Appendix E: Pt/SiO_2 TEM images before/after DRIFTS measurements

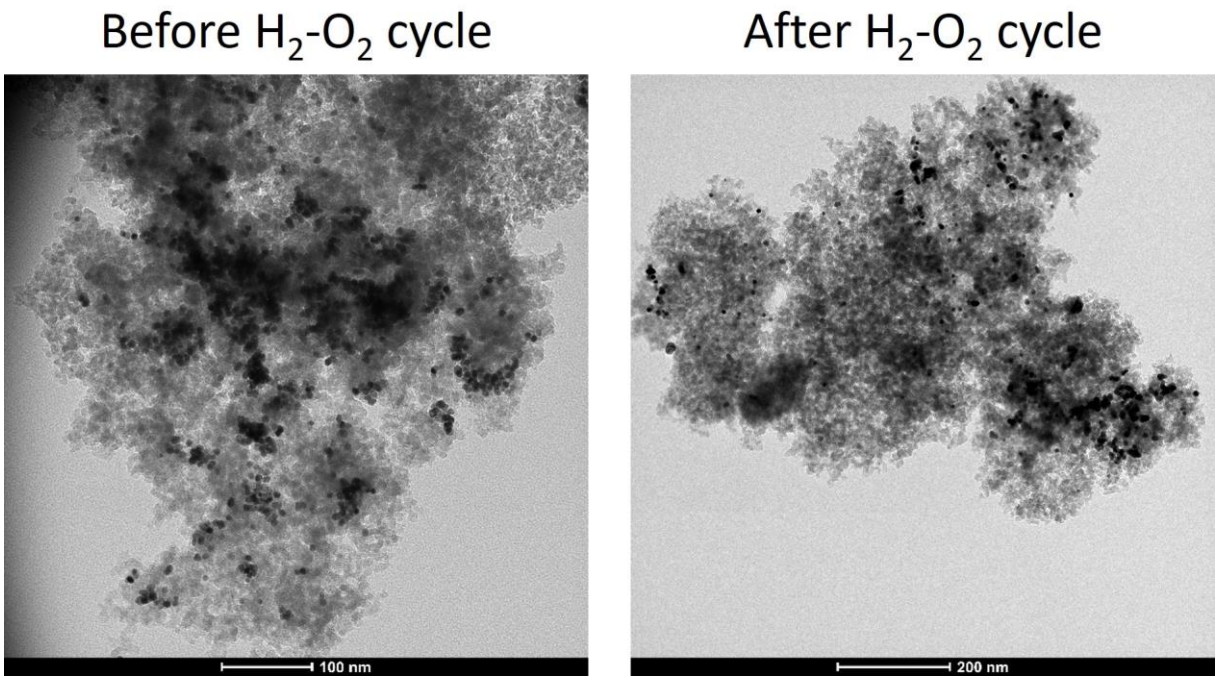

Figure 42 TEM images of Pt nanoparticles on SiO_2 (S18) before and after a DRIFTS measurement. During the DRIFTS measurement H_2, O_2, and CO gasses were flown over the sample and the sample was heated to 300 °C. 'S' refers to synthesis, each synthesis' conditions can be found in Table 2.